University of Tennessee, Knoxville
TRACE: Tennessee Research and Creative Exchange

Doctoral Dissertations

Graduate School

12-2011

Design of Wireless Power Transfer and Data Telemetry System for Biomedical Applications

Ashraf Bin Islam
University of Tennessee - Knoxville, aislam@utk.edu

Follow this and additional works at: https://trace.tennessee.edu/utk_graddiss

Part of the Electrical and Electronics Commons, Electromagnetics and Photonics Commons, Electronic Devices and Semiconductor Manufacturing Commons, and the VLSI and Circuits, Embedded and Hardware Systems Commons

Recommended Citation

Islam, Ashraf Bin, "Design of Wireless Power Transfer and Data Telemetry System for Biomedical Applications. " PhD diss., University of Tennessee, 2011.
https://trace.tennessee.edu/utk_graddiss/1195

This Dissertation is brought to you for free and open access by the Graduate School at TRACE: Tennessee Research and Creative Exchange. It has been accepted for inclusion in Doctoral Dissertations by an authorized administrator of TRACE: Tennessee Research and Creative Exchange. For more information, please contact trace@utk.edu.

To the Graduate Council:

I am submitting herewith a dissertation written by Ashraf Bin Islam entitled "Design of Wireless Power Transfer and Data Telemetry System for Biomedical Applications." I have examined the final electronic copy of this dissertation for form and content and recommend that it be accepted in partial fulfillment of the requirements for the degree of Doctor of Philosophy, with a major in Electrical Engineering.

Syed K. Islam, Major Professor

We have read this dissertation and recommend its acceptance:

Benjamin J. Blalock, Leon M. Tolbert, Thomas T. Meek

Accepted for the Council:

Carolyn R. Hodges

Vice Provost and Dean of the Graduate School

(Original signatures are on file with official student records.)

To the Graduate Council:

I am submitting herewith a dissertation written by Ashraf Bin Islam entitled, "Design of Wireless Power Transfer and Data Telemetry System for Biomedical Applications." I have examined the final electronic copy of this dissertation for form and content and recommend that it be accepted in partial fulfillment of the requirements for the degree of Doctor of Philosophy, with a major in Electrical Engineering.

____
Syed Kamrul Islam, Major Professor

We have read this dissertation
and recommend its acceptance:

____
Benjamin J. Blalock

____
Leon M. Tolbert

____
Thomas T. Meek

Accepted for the Council

____
Carolyn R. Hodges
Vice Provost and Dean of the Graduate School

DESIGN OF WIRELESS POWER TRANSFER AND DATA TELEMETRY SYSTEM FOR BIOMEDICAL APPLICATIONS

A THESIS PRESENTED FOR THE

DOCTOR OF PHILOSOPHY

DEGREE

THE UNIVERSITY OF TENNESSEE, KNOXVILLE

Ashraf Bin Islam

December 2011

Copyright © 2011 by Ashraf Bin Islam

All rights reserved.

DEDICATION

This dissertation is dedicated to my wife, my parents and my siblings.

ACKNOWLEDGEMENTS

I would like to thank my advisor Dr. Syed K. Islam for all his support and guidance throughout my time at graduate school. I am grateful to Dr. Islam for taking me as his student, believing in my abilities, and teaching me research and other works in my graduate school. Special thanks to Dr. Leon M. Tolbert, Dr. Benjamin J. Blalock, and Dr. Thomas T. Meek for serving in my committee and critically reviewing my work.

I am thankful to Dr. Faquir C. Jain of University of Connecticut for giving me the opportunity to work in a joint research project. It was a good learning experience. I am grateful to Dr. Mohammad R. Haider of University of Alabama, Birmingham for nice and long discussion regarding circuit design. I would like to thank Dr. Aly Fathy for introducing me to Sonnet software and giving me the opportunity to use his lab equipments. I am thankful to Mr. Yun Seo Koo, Ms. Dianne Bull, Mr. Gary To for helping me in the measurement works. I would like to thank MOSIS MEP program for giving us the opportunity to fabricate integrated circuits.

I thank and congratulate my wife, Salwa Mostafa, for sharing this journey with me and for always being there. I would not have dared to walk this path had she not taken every step with me. Thanks to my mother for constant support. Also thanks to father, sister, brother, my in-laws, the rest of my family and friends for their constant prayers and the confidence they instilled in me.

I would also like to thank all the past and present members of Analog VLSI and Devices Laboratory for their help and support in various aspects. I have the warmest gratitude for Ms. Dana Bryson, Mr. William Rhodes and all staff members of EECS department for their loving support with any issues that may have arisen.

Lastly I thank the almighty for giving me this great opportunity and for providing a chance to interact with such wonderful people.

ABSTRACT

With the advancement of biomedical instrumentation technologies, sensor based remote healthcare monitoring system is gaining more attention day by day. These sensors can be classified as wearable and implantable. While the wearable sensors are placed outside the body, the implantable types are placed underneath the skin or inside the body cavity typically via surgical means. Implantable sensors are placed inside the human body to acquire the information on the vital physiological phenomena such as glucose, lactate, pH, oxygen, etc. These sensors have associated circuits for sensor signal processing and data transmission. Powering the circuit is always a crucial design issue. Batteries cannot be used in implantable sensors which can come in contact with the blood resulting in serious health risks. An alternate approach is to supply power wirelessly for tether-less and battery- less operation of the circuits.

Inductive power transfer is the most common method of wireless power transfer to the implantable sensors. For good inductive coupling, the inductors should have high inductance and high quality factor. But the physical dimensions of the implanted inductors cannot be large due to a number of biomedical constraints. Therefore, there is a need for small sized and high inductance, high quality factor inductors for implantable sensor applications. In this work, design of a multi-spiral solenoidal printed circuit board (PCB) inductor for biomedical application is presented. The targeted frequency for power transfer is 13.56 MHz which is within the license-free industrial, scientific and medical

(ISM) band. A figure of merit based optimization technique has been utilized to optimize the PCB inductors. Similar principal is applied to design on-chip inductor which could be a potential solution for further miniaturization of the implantable system. Typically on-chip inductors require very small footprint around few mm^2 and accordingly have very small values around tens of nH. To accommodate the small values of inductance the operating frequency needs to be increased to GHz range. For layered human tissue, the optimum frequency of power transfer is 1 GHz for smaller coil size. For this reason, design and optimization of multi-spiral solenoidal integrated inductors for 1 GHz frequency is proposed. Finally, it is demonstrated that the proposed inductors exhibit a better overall performance in comparison with the conventional inductors for biomedical applications.

TABLE OF CONTENTS

LIST OF TABLES

LIST OF FIGURES

Chapter 1

INTRODUCTION AND GENERAL INFORMATION

1.1 Targeted Biomedical Applications

1.1.1 Categories of Biomedical Applications

Recent growth of biomedical applications has paved a new way for research and development (R&D). Key factors driving R&D works for biomedical applications are aging populations, rising healthcare costs, remote patient monitoring, and the rapid development of biotechnologies. It is a cross functional research area that bridges electrical engineering with biology and medicine. Biomedical applications can be primarily categorized into three major divisions – biotechnology, clinical engineering and medical devices (see Figure 1-1). The focus of this research work is on the design of wireless power transfer and data telemetry system for the medical devices, particularly the biomedical sensors.

Biomedical devices are used for diagnosis, mitigation, treatment, or prevention of disease. These devices can be divided into two major groups – imaging and sensors. The focus of this work is on biomedical sensors which are used for detection of various analytes in human body. Biomedical sensors can have the following three major components (see Figure 1-2):

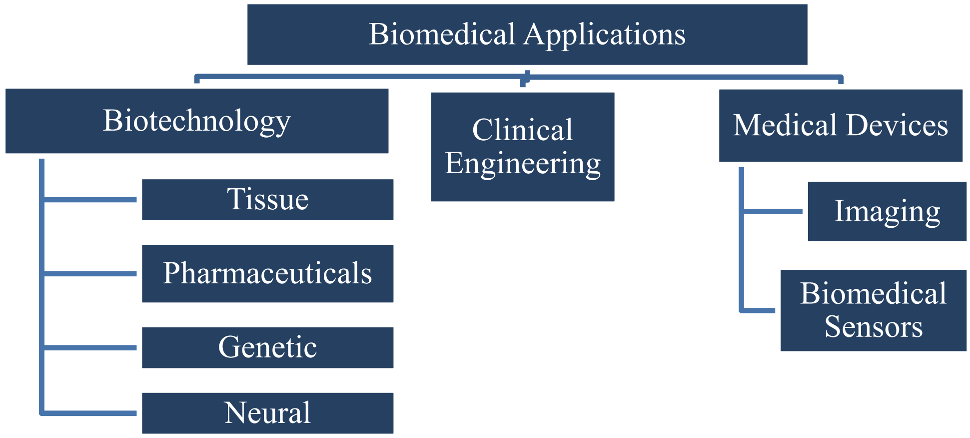

Figure 1-1: Major components of an implantable biomedical sensor.

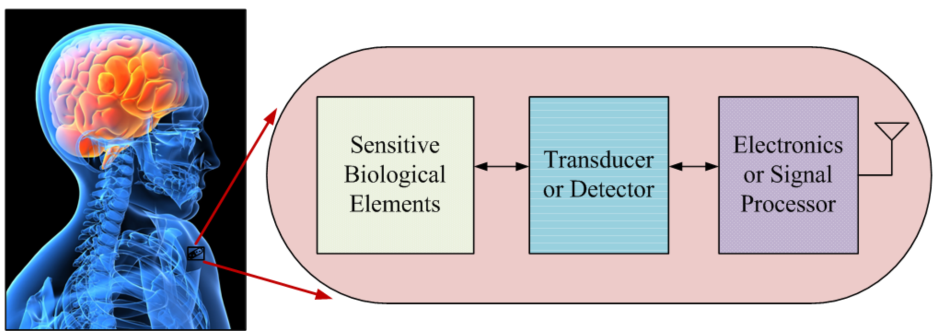

Figure 1-2: Key components of an implantable biomedical sensor.

1. Sensitive biological element: tissue, microorganisms, organelles, cell receptors, enzymes, antibodies.
2. Transducer or detector element
3. Electronics or signal processors

Based on the placement location, biomedical sensors can be of two types:

1. External sensor: External sensors are placed outside the human body to measure physiological activities such as blood pressure, pulse, body temperature, etc.
2. Implantable sensor: Implantable sensors are placed inside the human body to detect and measure various biologically relevant metabolites of interest such as glucose, pH, lactate, CO_2, O_2, lipoprotein, etc.

   Implantable sensors can be implemented in two ways:

1. Subcutaneous / transdermal sensor: this sensor is placed underneath the skin
2. Fully implanted inside the human body

1.1.2 Need for Implantable Biosensors

Implantable biosensors are very important for continuous monitoring of various physiological phenomena of a patient. These sensors are designed to provide metabolite level without the need for patient intervention regardless of the patient's physiological state (exercise, rest, sleep, etc.). For example, diabetic patients need to monitor the blood glucose level on a regular basis depending on the state of the disease. Generally it is done by collecting data from test strips using blood drawn from finger pricking. This procedure is not only painful but also incapable of reflecting the overall direction, trends, and patterns associated with daily habits [1]. This predicament initiated an extensive range of research efforts focused on developing implantable biosensors for continuous monitoring of various biologically relevant metabolites [2]. As glucose biosensor accounts for 85% of the biosensor market, it is the dominant sector of the biosensor research [3]. Intensive research is going on in other applications such as sensors for detecting electric signals in the brain [4], sensors for nerve stimulation capable of alleviating acute pain [5], and sensors for monitoring bio-analytes in the brain [6] together with implantable drug delivery systems for controlled delivery at the site of pain and stress [7, 8].

1.2 Powering Biomedical Sensors

The electronics inside the biosensor are used for signal processing and telemetry. These electronics blocks need power to function properly. The focus of the work is to develop external powering schemes for these types of sensor systems which are fully implanted inside the human body. Powering of implantable biomedical sensors is a major concern due to various constraints. Typically the leading source of powering involves batteries which can be used inside the human body if placed into a body cavity and are hermetically sealed. For example, pacemakers use batteries which have a typical lifetime of 5 to 7 years. These types of batteries are hermetically sealed and are placed inside human cavity via surgical means. Replacing these batteries is also cumbersome requiring surgical procedures. However, a battery is not recommended to be placed inside the human body when it may come in contact with blood. For example, the following sensors cannot use batteries as they directly come in contact with blood – glucose, pH, lactate, lipoprotein, CO_2, and O_2. The main risk of putting batteries in contact with blood is leakage which may lead to chemical burns, poisoning, and even death. There are alternative methods to power up the implantable sensors which are discussed below.

1.2.1 Alternate Sources of Energy

Alternate sources of energy as listed in Table 1-1 show promising prospect for powering sensors. Some of the alternate sources of energy, corresponding energy density, pros and cons are summarized in Table 1-1.

Table 1-1: Comparison of Some Alternate Sources of Energy

Method	*Energy Density [9]*	*Pros*	*Cons*
Piezoelectric	200 $\mu W/cm^3$	No need to supply energy from outside	Depends on the movement of subject
Thermoelectric	60 $\mu W/cm^3$	Contains no materials that must be replenished	Low efficiency < 5% Energy Storage is required
Kinetic (wrist watch)	4 $\mu W/cm^3$	Contains no materials that must be replenished	Depends on the movement of subject
Ambient RF Energy Harvesting	1 $\mu W/cm^2$	Harvest energy from ambient EM wave	Output depends on the availability of the EM wave
Visible Light	100 mW/cm^2	Sunlight is free	Light is not present at night and cloudy days
Temperature Variation	10 $\mu W/cm^3$	Contains no materials that must be replenished	Low efficiency Energy Storage is required
Airflow	1 $\mu W/cm^2$	Contains no materials that must be replenished	Difficult to implement for implantable systems
Heel Strike	7 W/cm^2	Good source of energy	Depends on the movement of subject

1.2.2 Need for Wireless Power Transfer

All the methods discussed in Table 1-1 have some positive as well as some negative attributes. The method which does not have these problems is wireless power transfer (WPT). WPT is clean, controllable, does not depend on the movement of patient and can be available 24/7. Although WPT is less efficient than battery, it is more efficient than the other energy sources described in Table 1-1. Moreover, if designed properly, WPT is harmless compared to a battery which makes it suitable for biomedical applications. Another advantage of WPT is the lifetime. A battery can last 5~7 years and needs surgical procedures to remove and replace it. But WPT has the same working lifetime of the electronics (15~20 years) which makes it much cheaper than battery. WPT is discussed briefly in the following section.

1.3 Wireless Power Transfer (WPT)

Wireless power transfer (WPT) is the propagation of electrical energy from a power source to an electrical load without the use of interconnecting wires. Wireless transmission is useful in cases where interconnecting wires are difficult, hazardous, or non-existent. Wireless power transfer is becoming popular for induction heating, charging of consumer electronics (electric toothbrush, Wii charger), biomedical implants, radio frequency identification (RFID), contact-less smart cards, and even for transmission of electrical energy from space to earth.

Famous scientist Nicola Tesla first demonstrated the potential of WPT using the 'Tesla coil' which was a resonant transformer for which he filed a patent in 1902 [10]. In his design, the secondary side of the transformer was excited by resonant inductive coupling. After the invention many researchers demonstrated the use of WPT for various applications.

1.3.1 Types of Wireless Power Transfer

Wireless power transfer can be divided into two major types – electromagnetic induction and electromagnetic radiation. Electromagnetic induction can be of three types – electrodynamic, electrostatic and evanescent wave coupling. Electromagnetic radiation can be divided into two categories – microwave power transfer (MPT) and laser. The types of wireless power transfer are shown in following Figure 1-3.

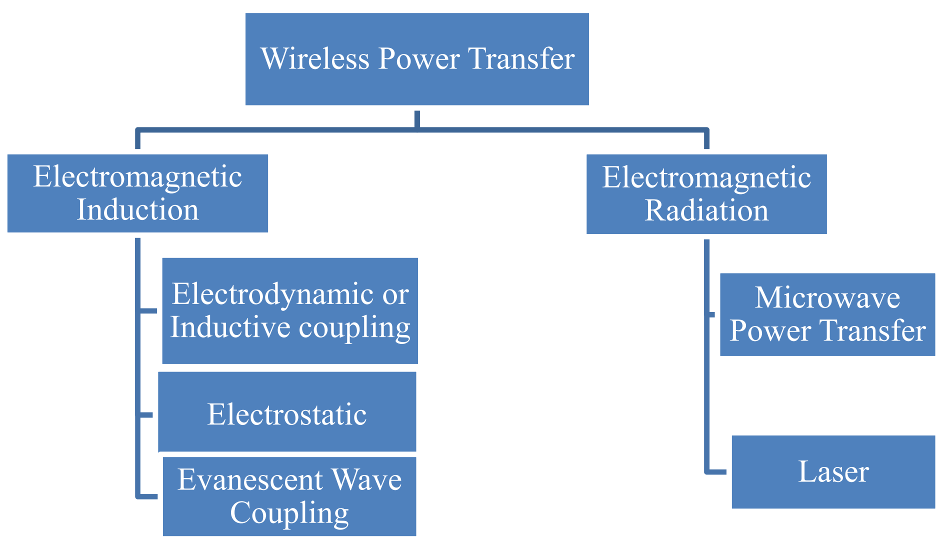

Figure 1-3: Types of wireless power transfer.

1.3.2 Electromagnetic Induction

It is the production of an induced voltage in a circuit which is excited by means of the magnetic flux. The condition for an induced current to flow in a closed circuit is that the conductors and the magnetic field must rotate relative to each other. It can be of three different types.

a) Electrodynamic or inductive coupling: Inductive coupling is the coupling of energy between two inductors or coils using near field radiation. It is also known as inductive or magnetic coupling. Inductive coupling is discussed in detail later.

b) Electrostatic: Electrostatic or capacitive coupling is the feeding of electrical energy through a dielectric medium. The electric field is generated by an alternating current of high voltage and high frequency.

c) Evanescent wave coupling: Evanescent wave coupling is a process by which electromagnetic waves are transmitted from one medium to another by means of evanescent, exponentially decaying electromagnetic field.

1.3.3 Electromagnetic Radiation

Electromagnetic radiation travels through vacuum at the speed of light and propagates by the interaction of time varying electric and magnetic fields. It has a wavelength and a frequency and can have two different forms:

a) Microwave power transmission: Microwave signal is used to transmit directional power to a large distance (usually in kilometers). Rectennas (rectifying antennas) are used to convert the energy back to electricity.

b) Laser: Power can be transmitted by converting electricity into a laser beam which is then pointed at a solar cell receiver. That receiver can convert light to usable electrical energy.

1.3.4 Limitations of Wireless Energy Transfer

There are a number of limitations to the full implementation of wireless energy transfer:

a) Size: The size of the transmitter or the receiver sometimes becomes too large to implement in a smaller systems.

b) Range: The range of wireless energy transfer is just a few meters, which represents a major hurdle towards its practical implementation.

c) Efficiency: Typical efficiency of wireless energy transfer ranges between 45% and 80% and is less efficient than conventional wire based energy transfer methods.

The prominent method of transferring wireless power is electrodynamic or inductive coupling. Inductive coupling is discussed in the following section.

1.4 **Inductive Link**

1.4.1 Inductive Link or Inductive Coupling

An inductive link is formed by a loosely coupled transformer consisting of a pair of coils that are usually placed in a coaxial arrangement as shown in Figure 1-4. The external or the primary coil is excited by an alternating current, and thus an electromagnetic field is produced with its magnitude dependent on the dimensions of the coil, the drive current and the frequency of operation. A portion of the alternating flux lines generated this way link to the internal or the secondary coil, and the change in flux linkage produces a voltage in the secondary coil, which is proportional to the rate of change of the flux and the number of turns in the secondary coil (Faraday's law of electromagnetic induction). If the number of turns is n and the magnetic flux linking each turn is ψ_m, then the induced voltage for the circuit can be written as,

$$V = n\frac{d\psi_m}{dt} \tag{1-01}$$

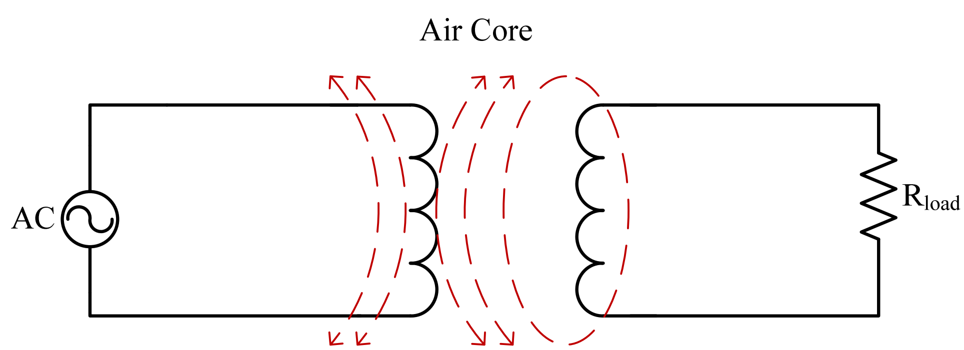

Figure 1-4: An inductive link produced by alternating electromagnetic field.

1.4.2 Use of Inductive Link

Inductive link has a wide range of applications.

a. A transformer is basically an inductive link which transfers electrical energy from one circuit to another through inductively coupled conductors. The windings are wound around a ferromagnetic core for good power transfer efficiency.

b. In induction motors current in the primary side creates an electromagnetic field which interacts with the electromagnetic field of the secondary side to produce a resultant torque, thereby transforming the electrical energy into mechanical energy.

c. Batteries of electric vehicles also can be charged via inductive link. In some factories inductive link is also deployed underneath the floor to power up the tools.

d. Radio frequency identification (RFID) readers power up the passive RFID tags located in remote location via inductive link.

e. Electronic article surveillance (EAS) system powers remote RFID tags to detect product theft. Inductive chargers charge batteries using inductive coupling, such as electric toothbrushes, Wii remotes, cell phones, etc.

f. Induction cookers transfer power from the cooker to the cooking pan using inductive link. Thus flame can be avoided in the kitchen.

g. Inductive powering is used in various biomedical applications, such as cochlear implant, retinal prosthesis, brain-machine interface, etc.

1.5 Health Related Issues

It is essential to consider the associated health risks in designing wireless power transmission system for biomedical applications. Heating of the tissue occurs due to the exposure of the human body to RF energy. This is referred as "thermal" effect. Lazzi summarizes the thermal effect of biomedical implants on the human body [11]. It has been known for many years that the exposure to very high levels of RF radiation can be harmful due to the ability of RF energy to rapidly heat the biological tissues. Tissue damage in humans could occur during exposure to high RF levels because of the inability of the body to cope with or dissipate the excessive heat that could be generated. Federal Communications Commission (FCC) regulates the time and the amount of exposure of the electromagnetic waves to human tissues at various frequencies [12]. American National Standards Institute (ANSI) standard C95.1-1982 sets the electromagnetic field strength limits for the general public for frequencies between 300 kHz and 100 GHz [13, 14]. Below 300 MHz the electric and the magnetic fields must be accounted for separately. The ANSI standard C95.1-1982 is superseded by The Institute of Electrical and Electronics Engineers (IEEE) standard C95.1-1991, which sets the electric and the magnetic field strength limits for the general public for frequencies between 3 kHz and

300 GHz [15]. Below 100 MHz the electric and the magnetic fields must be accounted for separately. Table 1-2 illustrates the IEEE standard C95.1-1991.

Table 1-2: IEEE Standard C95.1-1991:Limit of Maximum Permisible Exposure at Controlled Environment on Human Body [15]

Frequency Range (MHz)	*Electric Field Strength, E (V/m)*	*Magnetic Field Strength, H (A/m)*	*Power Density, S (mW/cm^2)*		*Averaging Time*
			E-field	H-field	$\|E\|^2, \|H\|^2$ *(minutes)*
0.003-0.1	614	163	100	1E6	6
0.1-3.0	614	16.3/f	100	$10000/f^2$	6
3-30	1842/f	16.3/f	$900/f^2$	$10000/f^2$	6
30-100	61.4	16.3/f	1	$10000/f^2$	6
100-300	61.4	0.163	1		6
300-3K	--	--	f/300		6
3K-15K	--	--	10		6
15K-300K	--	--	10		$616000/f^{1.2}$

f = Frequency in MHz

The quantity used to measure how much energy is actually absorbed in a body when exposed to radio frequency (RF) electromagnetic field is called the specific absorption rate (SAR). It is defined as the power absorbed per mass of the tissue and has units of watts per kilogram (W/kg) or milliwatts per gram (mW/g). SAR can be calculated as,

$$SAR = \int \frac{\sigma(r)|E(r)|^2}{\rho(r)} dr \tag{1-2}$$

here, σ is the electrical conductivity of the sample, E is the RMS electric field and ρ is the sample density. In the case of whole-body exposure, a standing human adult can absorb RF energy at a maximum rate when the frequency of the RF radiation is in the range of about 80 MHz and 100 MHz, meaning that the whole-body SAR is at a maximum under these conditions (resonance). Because of this resonance phenomenon, RF safety standards are generally most restrictive for these frequencies. SAR should be within the tolerable acceptable range for biological tissue [16, 17]. A whole-body average SAR of 0.4 W/kg has been set as the restriction that provides adequate protection for occupational exposure [18]. The FCC limit for public exposure from cellular telephones is an SAR level of 1.6 W/kg [19]. Two areas of the body, the eyes and the testes, are particularly vulnerable to RF heating because of the relative lack of available blood flow to dissipate the excessive heat load. At relatively low levels of exposure to RF radiation, that is, levels lower than those that would produce significant heating; the evidence for harmful biological effects is ambiguous and unproven. Such effects have sometimes been referred to as "non-thermal" effects. It is generally agreed that further research is needed to determine the effects and their possible relevance, if any, to human health.

1.6 Dissertation Outlines

The outline of this dissertation is as follows.

A brief introduction of biomedical applications, sources of energy and wireless power transfer for biomedical applications have been presented in chapter 1. The motivations behind this research work, research objectives and health related issues of wireless power transfer have also been discussed in this chapter.

An example of implantable sensor based patient monitoring system is discussed on chapter 2. Prior works on wireless power transfer for implantable biomedical system are discussed in this chapter. Several features of data telemetry system have also been discussed and a review of previous works has been summarized.

Inductive link based power transfer system has been employed in this work. Underlying theory of the inductively powered coils, the factors which affect performance of the inductive link and a board level design of inductive power transfer system are discussed in chapter 3.

Printed circuit board (PCB) inductors are used for wireless power transfer system. Chapter 4 discusses design of multi-stack solenoidal PCB inductor, mathematical modeling of the PCB inductor for single-layer and multi-layer spiral inductors, and the effect of variation of design parameter on PCB inductor such as number of metal layers, metal spacing, and metal width. An optimization technique for PCB inductors is also discussed in this chapter. The designed inductor is compared with state of the art work.

The PCB inductors need to be replaced by on-chip inductor for the realization of the miniaturized implantable wireless power transfer system in future. Chapter 5 discusses the challenges associated with the design of the on-chip inductors, mathematical model of the inductors, methods of improvement, design of solenoidal multi-layer stacked on-chip inductors and an optimization method based on figure of merit. The layout of on-chip inductor, on-wafer calibration technique and measurement results are also discussed in this chapter.

Chapter 6 discusses design of power oscillator based wireless telemetry system and its components such as differential power oscillator, rectifiers, sensor read-out circuit, backward data telemetry unit and data recovery unit.

Finally a conclusion of this research work is drawn and some of the future works in the related field are mentioned in chapter 7.

Chapter 2

REVIEW OF PRIOR WORKS

2.1 Implantable Sensor Based Patient Monitoring System

Recently a wireless body area network (WBAN) based patient monitoring system for a comprehensive healthcare alternative has been proposed [20]. This system provides early detection of abnormal conditions and prevention of serious consequences. This system incorporates a number of different sensors to monitor various physiological phenomena (electrocardiography, oxygen, temperature, motion, glucose, etc.) and the data is transmitted to a server computer which communicates with the central database through the internet. The data is monitored and stored in the central database and based on the sensor data proactive measures could be initiated by healthcare providers. Some of the physical phenomena can only be monitored by placing implantable sensors inside the human body. An overview of this system is shown in Figure 2-1.

As the data is stored in a medical server, long-term and short-term patient treatment can be optimized based on the medical history. Example of this work is glucose monitoring of diabetes patients. Personal glucose monitoring can be integrated with the WBAN based health monitoring system. Closed loop insulin delivery is a good choice for the system level integration. This system monitors glucose in real-time and activates/deactivates an insulin pump depending on the blood glucose level of the body.

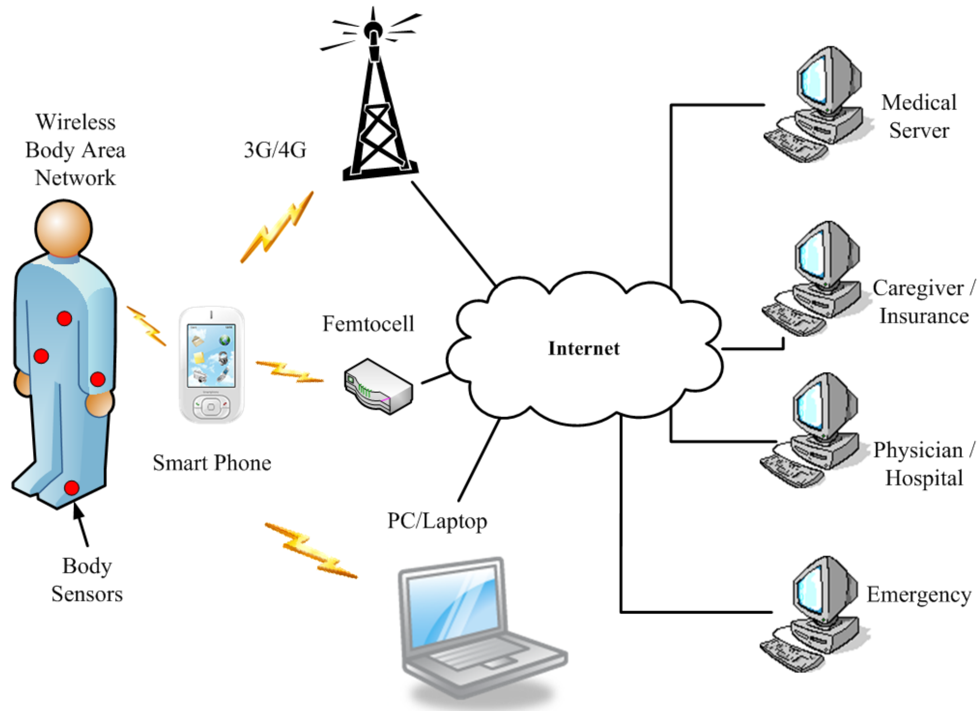

Figure 2-1: Overview of wireless body area network (WBAN) based patient monitoring system.

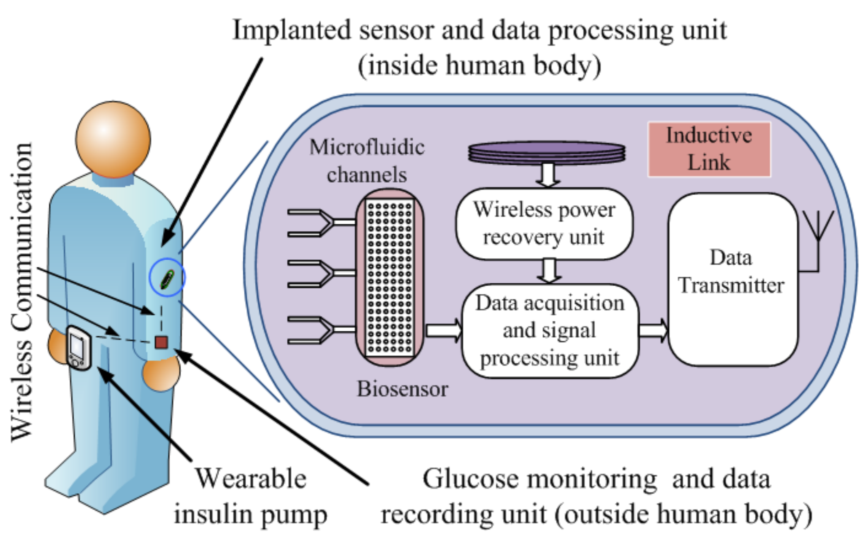

Figure 2-2: A conceptual overview of closed-loop based glucose monitoring and insulin pump system based on the implantable glucose capsule.

A conceptual overview of closed-loop based glucose monitoring and insulin pump system based on the implantable glucose capsule is shown Figure 2-2. This system is described in the following section.

An '*implanted sensor and data processing unit*' is placed inside the human or patient's body where it measures the glucose level, processes the data and sends the data signal back to the remote station for monitoring and further processing. A '*glucose monitoring and data recording unit*' (which could be worn like a wrist watch) is placed outside the human body which wirelessly powers up the implantable unit, monitors the blood glucose, and depending on the glucose level sends the signal wirelessly to an '*insulin pump*' to inject the required dose of insulin into the human body to control the blood glucose level. This ensures real-time patient monitoring and health care around the clock. In the encapsulated system 'microfluidic channels' draws the sample (blood) and brings the sample in close proximity of the sensor. The '*Biosenso*r' block detects and measures the glucose level. '*Data acquisition and signal processing unit*' stimulates the biosensor as well as collects and processes the data. The '*data transmitter*' unit wirelessly transmits the data outside of the human body using biomedical frequency band. The '*wireless power recovery unit*' harvests the power supplied wirelessly from outside of the human body via inductive link and delivers the power required to operate the electronic components of the system. The entire sensor system is encapsulated in biocompatible materials to prevent contamination of the body fluid.

2.2 Inductive Link for Biomedical Implantable Systems

Biomedical sensing technology is going through a rapid development in recent years. Rise of micro- and nano-fabrication facilities with inexpensive signal processing systems has led to the development of various biomedical sensors. Silicon-based microfabrication and microelectromechanical (MEMS) techniques have been successfully applied for the fabrication of a number of different types of miniature electrochemical biomedical sensors. These advances in the fabrication processes have enabled significant recent research focused on the investigation of continuous *in vivo* measurement and monitoring of various physiological variables by means of implantable sensors. Examples include monitoring of the blood glucose level [21-23], continuous *in vitro* monitoring of lactate in the bloodstream or tissues [24], and minimally invasive monitoring of pressure in blood vessels and intracranial compartments [25]. Primary emerging and commercialized sensing technologies of the past few years are summarized by G. L. Cote [26].

For biomedical applications, implanted electronics are being increasingly used for real-time patient monitoring, diagnosis, and in some cases for treatment. Inductive link is a common method for wireless powering of implantable biomedical electronics and data communication with the external world. Previously, transcutaneous power cables were used in some clinical implantable applications [27], but they introduce a significant path for infection. One alternative to the transcutaneous power cables is the use of implanted batteries, which provide a limited supply of power and may exceed size and mass requirements for the implant. In addition, replacement can only be performed by surgical procedure, and long-term implantation introduces a potential risk of leakage. Alternatively, inductive links do not suffer from these limitations, and consequently produce increased implant robustness and if implemented properly provide sufficient miniaturization. Wireless power transmission and data telemetry using an inductive link has been demonstrated for various biomedical applications including visual prosthesis, cochlear implants, neuromuscular and nerve stimulators, cardiac pacemakers/defibrillators, deep-brain stimulators, spinal-cord stimulators, brain-machine interfaces, gastrointestinal microsystems, and capsule endoscopy [28-38]. Emerging implantable and ingestible wireless biomedical devices are summarized by Bashirullah [39]. A summary of the prior works is given in Table 2-1.

2.3 Data Telemetry

Another important feature of implantable micro-systems is the wireless transmission of the sensor data for real-time monitoring and diagnosis. Data telemetry can be done in two ways: data transmission from power transmitter to power receiver is known as forward telemetry and data transmission from power receiver to power transmitter is known as backward telemetry.

Several modulation schemes such as amplitude-shift keying (ASK), frequency-shift keying (FSK), etc. have been reported in the literature. These schemes provide high energy efficiency by taking the benefits of low data rate and short distance communication associated with biomedical telemetry [37, 40]. For an inductively powered system the transmitting antenna of the data signal could be either the power link coils or a separate unit. Load-shift keying (LSK) modulation scheme utilizing the changing of the load value of an inductively coupled system has been reported in literature for biomedical implant applications [41, 42].

Table 2-1: Prior Arts on Wireless Power Transfer for Biomedical Implants

Reference	**Applications**	**Frequency**	**Inductor type**
[29]	Neural prosthetic implant	2 – 20 MHz	Ferrite core
[30]	Cochlear implant	--	--
[38]	Retinal prosthesis	1 MHz	Litz wire
[37]	Biomedical implant	5/10 MHz	--
[36]	Neural implant	4 MHz	Copper magnet wire
[33]	Endoscope	1.055 MHz	Litz wire
[34]	Gastrointestinal Microsystems	58.418 KHz	Copper wire
[43]	Neural recording	4 MHz	Litz wire
[44]	Implantable system	13.56 MHz	On-chip
[45]	Neural prosthesis	25 MHz	wire
[46]	Implantable prosthesis	1 GHz	Bond wire
[47]	Neuroprosthetic implantable device	13.56 MHz	PCB
[48]	Neural recording	2.64 MHz	Off-chip power, on-chip data
[49]	Neural recording	<10 MHz	Wire

Table 2-2: Summary of Prior Work on Data Telemetry for Biomedical Applications with Wireless Power Transfer

Refere-nce	*Forward Telemetry*		*Backward Telemetry*		*Application*
	Modulation Type	Data Rate, Carrier	Modulation Type	Data Rate, Carrier	
[50]	FM	1 Mbps, 20 MHz	N/A	N/A	Neural stimulators
[51]	FSK	100 kbps, 1 MHz	DBPSK	15.625 kbps, 500 kHz	Visual neuro-prosthesis
[52]	ASK-BPSK	1.507 Mbps, 13.56 MHz	LSK	1.13 Mbps, 13.56 MHz	cortical stimulator
[53]	Packet detect	-, 2.5 MHz	Burst of RF energy	-, 2.5 MHz	Neuro-stimulation
[54]	ASK	-, 4 MHz	PWM-ASK	125 kbps, 4MHz	Peripheral neural recording
[55]	OOK	100 kbps, 5 MHz	N/A	N/A	Neural stimulator
[56]	OOK	-, 6.78 MHz	LSK-CCM	200 kbps, 6.78 MHz	neuromuscular stimulation
[37]	FSK	2.5 Mbps, 5/10 MHz	N/A	N/A	Neural stimulation
[32]	PWM-ASK	25~250 kbps, 1~10 MHz	N/A	N/A	retinal prosthesis
[57]	N/A	N/A	LSK-pseudo PWM	3.3 kbps, 1MHz	retinal prosthesis
[36]	N/A	N/A	LSK	10 kbps, 4 MHz	neurological monitoring

Wireless-based systems should not interfere with existing communication systems. Due to these stringent requirements, medical radios tend to use industrial, scientific and medical (ISM) frequency bands with low data rate operation. Depending on the application, medical radios use various data rates and frequencies. For example, data bandwidths for pacemakers, cardiac defibrillators and analog cochlear processors are typically around 8 kbps [58, 59], neural recording uses 800 kbps [60] and retinal stimulators use 40 kbps data rate [61]. A summary of prior works on data telemetry for biomedical applications with wireless power transfer is given in Table 2-2.

2.4 **Conclusion**

An example of wireless power and data transfer system for biomedical application has been discussed in this chapter. Previously reported works on wireless power transfer system for biomedical applications have been summarized in Table 2-1 based on application, frequency and types of inductor. Various aspects of data telemetry such as modulation scheme, bit rate have also been discussed. Prior works on data telemetry are summarized in Table 2-2.

Chapter 3

DESIGN OF WIRELESS POWER TRANSFER (WPT) SYSTEM

3.1 Introduction

Generally the inductive link for biomedical applications involving implantable devices consists of two coaxially aligned circular coils, of which one coil is meant to reside inside the human body, while the other one to be placed in an external unit located just outside of the body. The link provides a means for transferring electrical power from the external to the internal unit that can be used by the implantable sensor interface electronics and communication module via transformer action. The same link or a different one can be used for transmission of digital data from the implant to the external unit, which is known as backward or reverse telemetry. A system level overview of the inductive link system is shown in Figure 3-1.

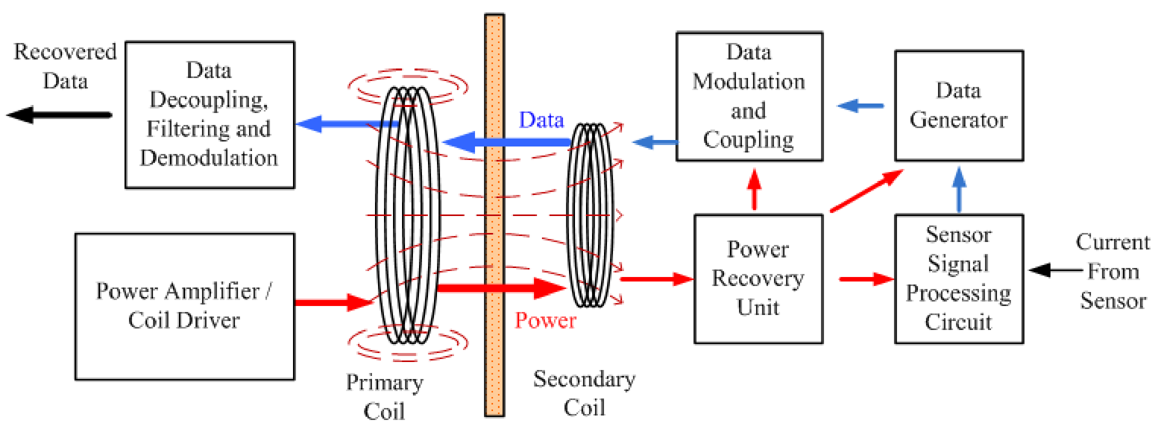

Figure 3-1: Block diagram of an inductive power transfer and backward data telemetry system.

In this system a '*power amplifier/coil driver'* with AC energy drives the primary coil. Power is transferred from the primary coil to the secondary coil via the inductive link through the skin. 'Power recovery unit' rectifies the received energy from AC to DC and then regulates the output voltage and supplies it to the *'sensor signal processing circuit'*, *'data generator'* and *'modulation and coupling'* blocks. The *'sensor signal processing circuit'* block takes current from sensor as input, processes the current and sends signal to the *'data generator'*. The '*data generator'* converts the signal to digitally encoded data signal and sends it to the *'data modulation and coupling'* block. The *'data modulation and coupling'* unit takes the data as input, modulates it and couples it to the secondary coil. The data is transmitted through the inductive link back to the primary side. The *'data decoupling, filtering and demodulation'* unit decouples the data and filters it out from the power signal and demodulates the data signal to get the information back. This is how a simple wireless power transfer and data transmission unit works. In some systems separate pairs of coils are used for transferring power and data. This method reduces the interference between the data and the power signal.

3.2 Theory of the Inductively Powered Coils

The fundamental concepts of designing an inductive link are described in this section following the work reported by W. H. Ko *et al.* [28]. The theory and accompanying practical design equations were developed using the basic inductively

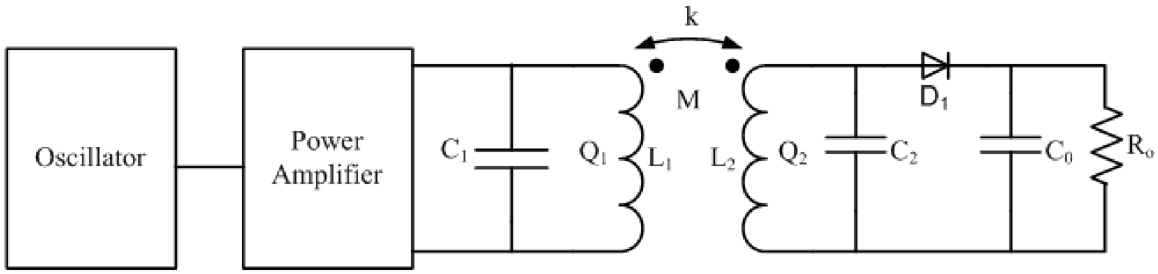

Figure 3-2: Basic inductively coupled circuit.

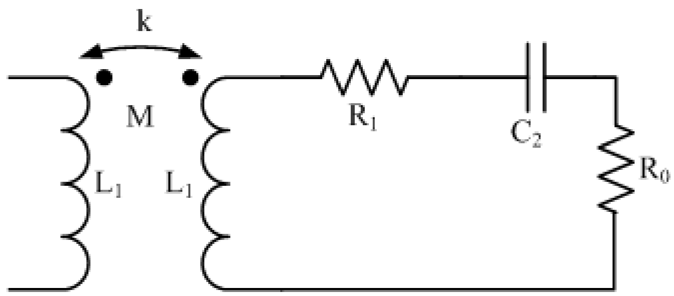

Figure 3-3: DC equivalent secondary circuit for basic inductively coupled circuit.

coupled circuit and its equivalent secondary circuit as shown in Figure 3-2 and Figure 3-3, respectively. In Figure 3-2, L_1 and L_2 are the inductances of the primary and secondary coils, respectively. In this figure, $M=k(L_1L_2)^{1/2}$ = mutual inductance of the coils, and $Q_1 = \omega L_1/R_1$, $Q_2=\omega L_2/R_2$ are the unloaded quality factors of the primary and secondary coils, respectively and '*k*' is the mutual coupling which has value ranging from 0 to 1. The equivalent AC load resistance *R* which will dissipate an amount of AC power equivalent to the DC power in load resistance R_0 is, $R= R_0/2$. The equivalent AC series resistance R_L due to the load R_0 is,

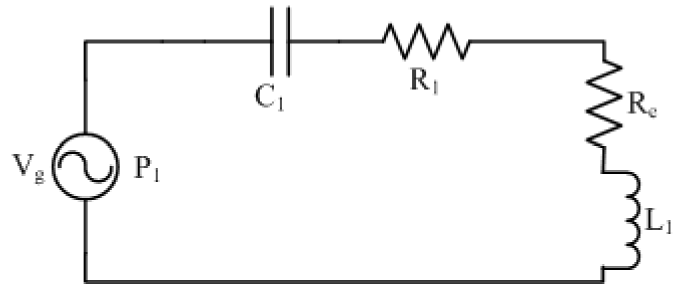

Figure 3-4: Primary referred equivalent circuit of basic inductively coupled circuit.

$$R_L = \frac{(\omega L_2)^2}{R} = \frac{2(\omega L_2)^2}{R_0} \tag{3-01}$$

The total equivalent series resistance in the secondary tank circuit is, $R_2 + R_L$, where R_2 is the series resistance of the unloaded secondary tank circuit and R_L is the load resistance. The equivalent resistance R_e, reflected back into the primary coil is,

$$R_e = \frac{(\omega M)^2}{R_2 + R_L} = \frac{Rk^2 Q_1 Q_2}{R + Q_2{}^2 R_2} R_1 \tag{3-02}$$

Therefore, the equivalent circuit referred to the primary side can be shown in Figure 3-4.

3.2.1 *Overall Circuit Efficiency at Resonance*

From the primary equivalent circuit shown in Figure 3-4, the efficiency of the circuit at resonance can be derived as,

$$P_i = \frac{1}{2}\left(\frac{|V_g|^2}{R_e + R_1}\right) \tag{3-03}$$

$$P_i = P_o = \frac{R_L}{R_L + R_2} \frac{R_e}{R_1 + R_e} P_i \frac{1}{2}\left(\frac{|V_g|^2}{R_e + R_1}\right) \tag{3-04}$$

$$\eta = \frac{P_0}{P_i} = \frac{k^2 Q_1 Q_2^3 R_2 R}{(R + Q_2^2 R_2)\{(1 + k^2 Q_1 Q_2)R + Q_2^2 R_2\}} \tag{3-05}$$

As can be seen from the above equation, the overall efficiency depends on coupling factor, k. However, value of k is dependent on size of the coil, coil spacing, and lateral and angular misalignment.

3.2.2 Optimum Efficiency

If the derivative of the efficiency expressed in equation (3-05) is taken with respect to R_2 (for a given set of k, Qs and R) and set to zero, then the optimum value of R_2 required for maximum efficiency is found to be,

$$R_{2opt} = \frac{R(1 + k^2 Q_1 Q_2)^{1/2}}{Q_2^2} \tag{3-06}$$

Substituting this result into equations (3-02) and (3-05) and yields the optimum efficiency of the circuit,

$$\eta_{opt} = \frac{k^2 Q_1 Q_2}{[1 + (1 + k^2 Q_1 Q_2)^{1/2}]^2} \tag{3-07}$$

This equation once again confirms that the optimum efficiency increases as $k^2 Q_1 Q_2$ increases, and therefore the first and the foremost design consideration in an inductive link design is the attainment of the highest possible unloaded Q and k. These two vital parameters are functions of the shape, size and relative position of the coils.

Putting $Q_1 = \omega L_1/R_1$, $Q_2 = \omega L_2/R_2$ in the equation (3-07) results in:

$$\eta_{opt} = \frac{k^2\omega^2\left(\frac{L_1L_2}{R_1R_2}\right)}{\left[1+\left(1+k^2\omega^2\left(\frac{L_1L_2}{R_1R_2}\right)\right)^{1/2}\right]^2} \tag{3-08}$$

3.2.3 Energy in the LC Circuit

The energy stored in magnetic field is $U_B = \frac{1}{2}LI^2$ while the energy stored in electric field can be expressed as, $U_E = \frac{1}{2}CV^2$. Thus the total energy in a LC circuit can be expressed as,

$$U = U_B + U_E = \frac{1}{2}LI^2 + \frac{1}{2}CV^2 \tag{3-09}$$

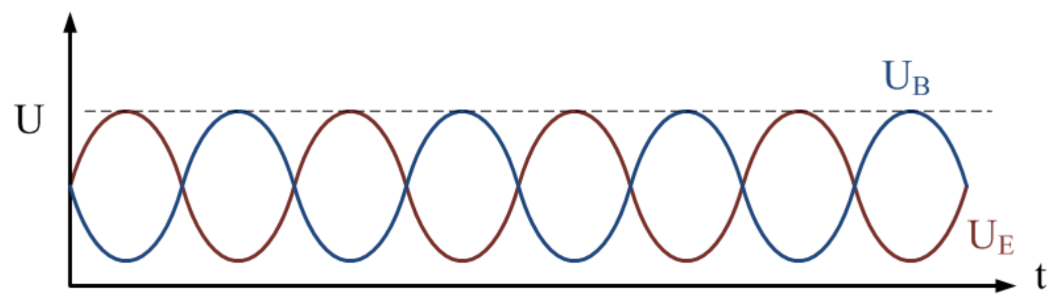

Figure 3-5: Electric and magnetic energy in the LC circuit.

At resonance condition, collapsing magnetic field of the inductor generates an electric current in its windings that charges the capacitor, and then the discharging capacitor provides an electric current that builds the magnetic field in the inductor. In resonance mode energy is transferred between inductor and capacitor and they are equal:

$$U_B = U_E$$

$$Energy = \frac{1}{2}LI^2 = \frac{1}{2}CV^2 \tag{3-10}$$

From equations (3-08) and (3-10) it can be concluded that the inductance is a very important design parameter of the inductive link. Higher value of inductance is required for higher energy and better efficiency.

3.3 Factors Affecting Inductive Link Performance

Some of the factors that vastly influence the performance of an inductive link are qualitatively discussed here. Most of these elements are greatly interdependent, and consequently, extensive trade-offs are associated with the design choices.

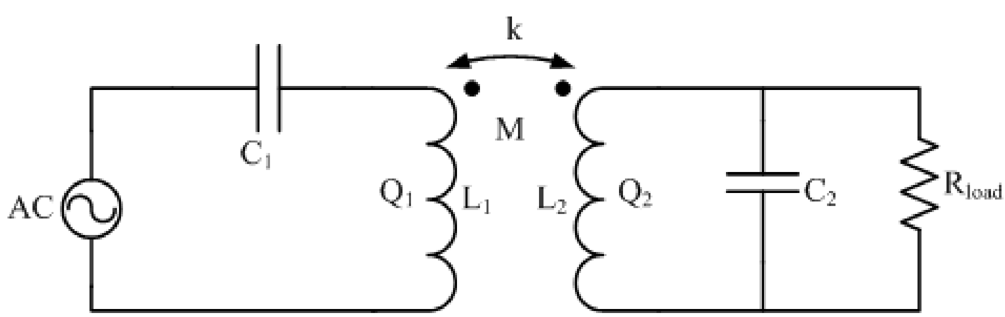

Figure 3-6: Schematic of a basic inductive link based on series-parallel resonance.

The maximum value of the mutual inductance that can exist between two coils of inductance L_1 and L_2 is $\sqrt{L_1 L_2}$, and this occurs when all the flux of one coil links with all the turns of the other. The ratio of the mutual inductance present between two inductances to the maximum possible value is called the coupling coefficient and is written as,

$$k = \frac{M}{\sqrt{L_1 L_2}} \tag{3-11}$$

The coupling coefficient is a dimensionless quantity which ranges from 0 to 1.

The link efficiency is defined as the ratio of the power delivered to the load to the power supplied to the primary coil. The total link efficiency for a parallel resonant secondary can be written as [62],

$$\eta = \frac{k^2 Q_1 Q_2}{\left(1 + \frac{Q_2}{\alpha} + k^2 Q_1 Q_2\right)\left(\alpha + \frac{1}{Q_2}\right)} \tag{3-12}$$

For a series resonant secondary the expression becomes,

$$\eta = \frac{k^2 Q_1 \alpha}{\left(1 + k^2 Q_1 + \frac{1}{Q_2}\right)\left(\alpha + \frac{1}{Q_2}\right)} \tag{3-13}$$

In both equations, Q_1 = quality factor of the primary coil, Q_2 = quality factor of the secondary coil, k = coupling factor between the coils, α = unit less constant = $\omega C_2 R_L$, ω = angular operating frequency, C_2 = capacitance of the secondary resonant capacitor, and R_L = load resistance.

The voltage gain of an inductive link depends on the diameters of the receiver and transmitter coils [29]. Since the self- and the mutual inductances of the coils also vary proportionally with their diameters, the link efficiency, also increase with increasing diameters. For implantable systems the limits on the receiver coil size are usually more stringent than those of the transmitter coil. The mutual inductance is proportional to the product of the number of turns in the transmitter and the receiver coils.

Spacing between coils can significantly affect the coupling. When the receiver coil is present within the circumference of the transmitter coil the performance is comparable or better than that with an exact coaxial alignment [29]. Variation in coil alignment also changes the mutual inductance and the link gain. Two types of misalignment can be present in the system - lateral misalignment and angular misalignment which can affect the link efficiency [27].

Quality factors (Q) of the primary and the secondary coils can change the link efficiency of a typical inductive link. [28, 63]. Therefore, reasonably high Q values are desired at the frequency of operation in order to achieve satisfactory power transfer. In addition the output voltage becomes sensitive to load changes when Q is low [50].

The frequency of operation is also an important design parameter. The maximum power through human tissue is determined by the frequency. The size of the coil, the mutual impedance, and the voltage transfer ratio are determined by frequency. Since the quality factor is a function of frequency, the efficiency and the bandwidth of the link are also impacted by the choice of frequency.

Generally low loss switching amplifiers are used to drive the external or the primary coil. The driver efficiency of the primary coil defines the overall power transfer efficiency of an inductive link. In an efficient system the drive transistor should only draw current when there is no voltage across it, which is achieved with a tuned amplifier load [64]. Most commonly used topologies reported in the literature are class-C [28, 64] or class-E [36, 38, 51, 57, 65, 66], class-D [50, 67] and class-C-E [63]. Sokal *et al.* reported the class-E amplifier which gives the highest efficiency by shaping the drain voltage and the current waveforms for the active device [68]. This amplifier exhibits an inherent insensitivity to small timing errors, as the transistor voltage and its derivative are ideally zero when the switch is turned on. The class-E amplifiers are superior to most of the switching amplifiers in terms of efficiency. Class-E amplifiers are quite sensitive to variations in the impedance of the output network. A variation in the internal load, either by a change in power demand or a change in coupling factor of the coils (k), will therefore result in a change in the equivalent series resistance of the primary circuit as seen by the driver. For implantable biomedical applications, changes in the physical configuration of the two coils and the surrounding materials will affect the overall link gain and efficiency.

3.4 Board Level Design of Inductive Power Transfer System

A board level design of a wireless power transfer system is shown in Figure 3-7. The system includes a sensor signal conditioning circuit, an inductive power transfer unit and a backward data communication unit. The signal conditioning circuit processes the sensor analog current and produces frequency modulated digital pulses. The modulator block employs frequency-shift keying (FSK) scheme to modulate the digital pulses and to transmit the data packets to the outside environment. This signal can be easily received and demodulated by a receiver outside of the sensor environment. The frequency of the recovered digital pulses represents the sensor current for a certain time frame and demodulated by a receiver outside of the sensor environment.

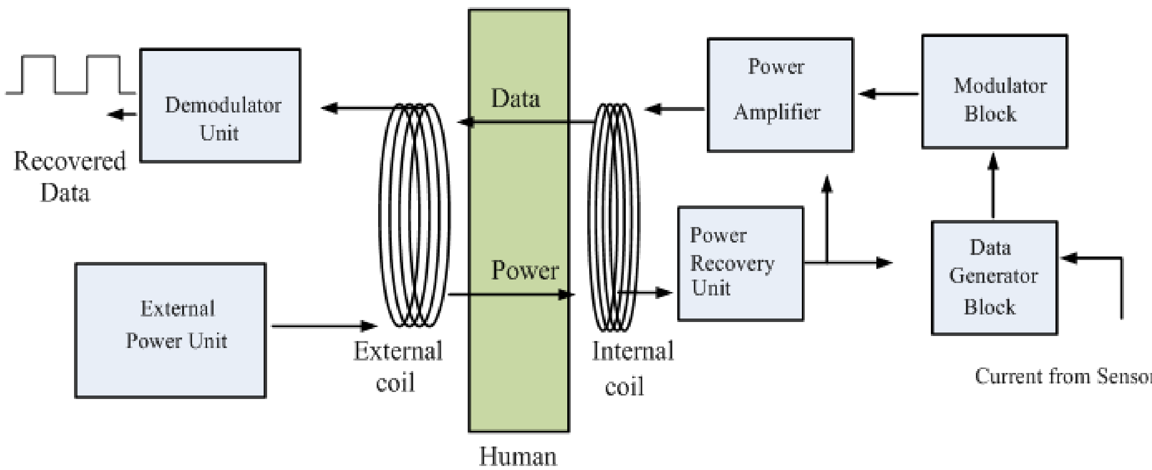

Figure 3-7: Block diagram of the designed system with inductive link.

The inductive power link provides the necessary power to the implanted unit for long-term monitoring and transmission of the sensor signals. Here the power is inductively coupled between the two coils separated by a few centimeters of distance. An efficient class-E power amplifier drives the primary coil (external coil) inducing a voltage on the secondary coil (internal coil) operated in resonance resonant condition and finally, the power recovery unit regulates this power to make it a useful power supply. Specification of the designed inductive link is summarized in Table 3-1.

Table 3-1: Specifications of the Designed Inductive Link

Parameters	**Value**
Frequency	200 KHz
Primary Coil (L_1)	7.4 μH
Secondary Coil (L_2)	267 μH
Coupling Factor (k)	0.453
Load Quality factor (Q_L)	4.58
Capacitor (Cs)	83.5 nF
Primary Capacitor (C_1)	119.3 nF
Rated output (V)	5
Rated distance	1 cm

3.4.1 Measurement Results of the Board Level Design

If the inductive link based system is used in an implantable biomedical application, misalignments of the coil could occur any time resulting in the reduction in the coupling efficiency of the system. Their misalignments typically can be due to change in coil spacing, lateral misalignment, or angular misalignment. In an implantable system, either a single misalignment or multiple misalignments can be present. The following section describes the effect of these misalignments on the proposed inductive link. While carrying out the experiments, only one misalignment parameter is varied while other two parameters are kept constant to isolate the effect of each misalignment. The effect of the change of these parameters has been discussed by Soma *et al.* [27].

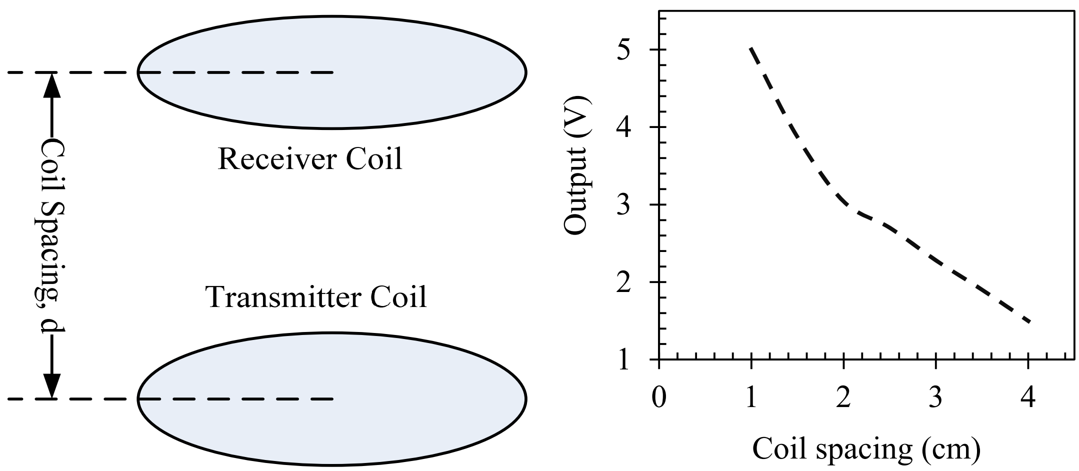

(a) (b)

Figure 3-8: Effect of variation of coil spacing between transmitter and receiver coils. (a) Orientation of the coils in this setup. (b) Output voltage decreases when coil spacing is increased beyond the rated distance of 1 cm.

Coil Spacing (d): The transmitter and the receiver coil are attached to separate Plexiglas boards in such a way that their planes are in parallel to each other. The centers of both the coils are located along the same axis as shown in **Error! Reference source not found.** (a). The coil spacing *d* can be varied by keeping the transmitter coil fixed while moving the receiver coil along the axis. The mutual inductance varies inversely proportional to *d* [27]. Measurements have been carried out by varying the coil spacing from 1 cm to 4 cm and it is found that output voltage decreases when coil spacing increases beyond rated distance of 1 cm as shown in **Error! Reference source not found.** (b).

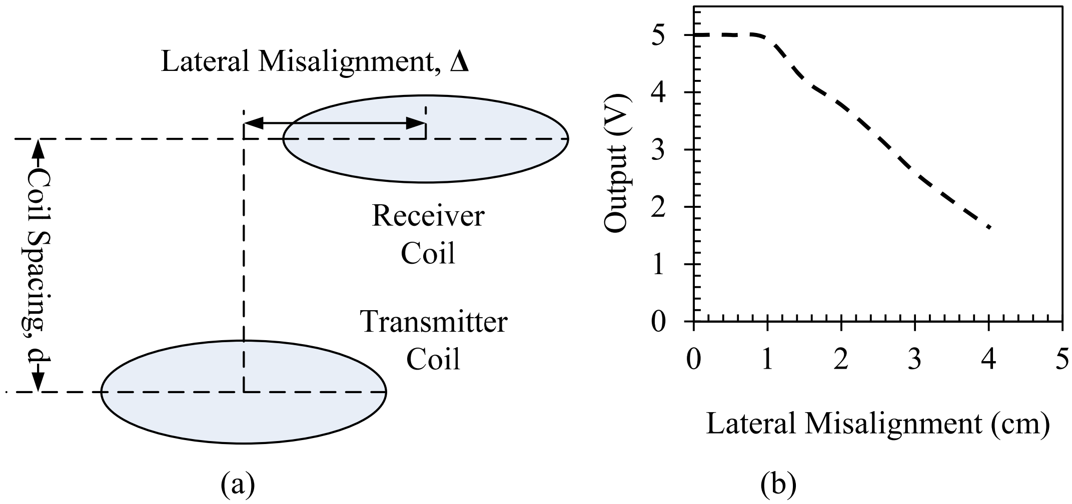

Figure 3-9: Effect of variation of lateral misalignment (Δ) between the transmitter and the receiver coils. (a) Orientation of the coils. (b) Decrease in output voltage for increase in lateral misalignment.

<u>*Effect of lateral misalignment (Δ):*</u> In this scenario, the centers of the coils are displaced in the horizontal direction **Error! Reference source not found.** (a), which is termed as lateral misalignment (Δ). The planes of the coils are still parallel to each other. The coil spacing *d* is kept fixed at 1 cm, while Δ is varied from 0 to 4 cm. Measurement results in **Error! Reference source not found.** (b) show that increment in Δ results in decrement in output voltage. This decrement in output voltage is due to the reduction in mutual inductance which is inversely proportional to Δ [27].

<u>*Effect of angular misalignment (φ):*</u> In this case, the centers of the two coils are kept along the same axis (Δ = 0), but their planes are tilted to form an angle φ Figure 3-10 (a) which is termed as angular displacement. The coil spacing *d* is kept fixed at 1 cm, while

φ is varied from 0^0 to 90^0. It is observed as φ is increased, output voltage drops due to the reduction in mutual inductance, which is inversely proportional to φ [27] When the planes of the coils become orthogonal to each other ($\varphi = 90^0$), there is no mutual inductance at all between the coils and output voltage drops to zero. The test results are shown in Figure 3-10 (b).

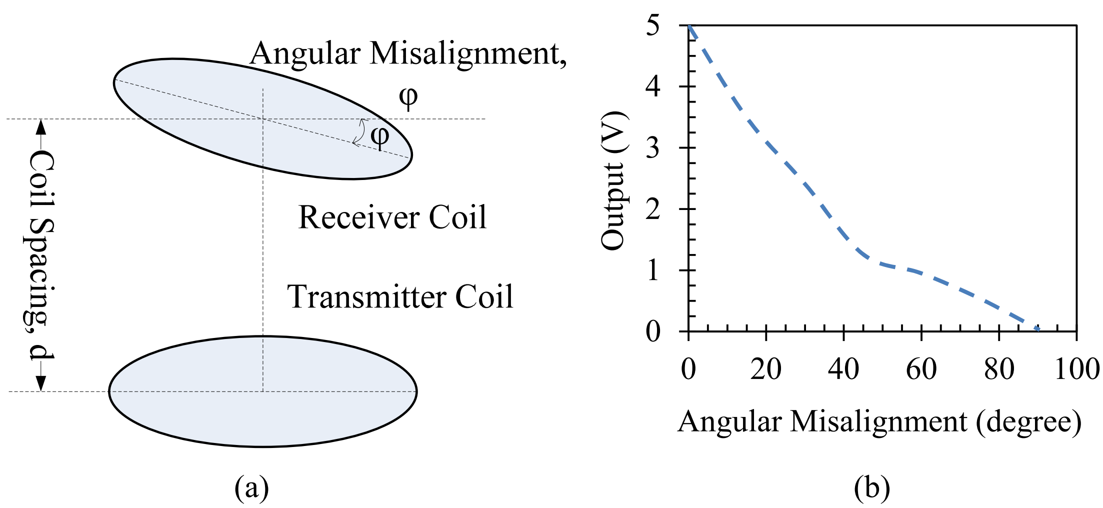

Figure 3-10: Illustration of angular misalignment (φ) between the transmitter and the receiver coils. (a) Orientation of the coils. (b) Change of output for increase in angular misalignment.

3.5 Conclusion

In this chapter, a brief overview of the fundamental theories of inductive link, associated features and factors affecting inductive links and their correlations have been presented. A board level design of inductive link has been performed. The designed link has been measured to observe the effect of the change of coil spacing, lateral misalignment and angular misalignment between transmitter and receiver coils on output voltage. Measurement results show that increase in coil spacing, lateral misalignment and angular misalignment can drastically reduce the coupling hence the output voltage of the receiver. The minimum peak to peak voltage that can be regulated by the voltage regulator would define how much of these misalignments a system could tolerate. While designing inductive links for biomedical applications these factors needs to be considered very carefully.

Chapter 4

DESIGN OF PRINTED CIRCUIT BOARD (PCB) INDUCTORS FOR WPT SYSTEM

4.1 Design of PCB Inductor

4.1.1 Introduction

Spiral printed circuit board (PCB) planar inductors are widely used in radio frequency applications. PCBs are inexpensive, low-cost and can be fabricated in large amounts in batches. Their geometries and aspect ratios can be optimized, which make them suitable for implantable systems placed underneath the skin or within the epidural space [69]. If fabricated on thin flexible substrates such as polyimide, they can also conform to the outer body or brain surface curvature. Shah *et al.* proposed PCBs for neuroprosthetic transcranial telemetry applications [70]. Micromachining techniques can be used to fabricate rigid hermetically sealed PCBs on silicon chips or low temperature co-fired ceramics (LTCC) [71, 72]. In this work, design of PCBs for WPT in biomedical applications is presented.

In this work, PCB inductors have been designed for targeted biomedical applications Frequency of operation is planned at 13.56 MHz license free industrial, scientific, and medical (ISM) band. In this frequency band, amount of allowable maximum electric field through human tissue is higher than high frequency bands which is strictly controlled by FCC [12]. The distance between the transmitter and the receiver coil is assumed to be 10 mm, which is a reasonable distance for most biomedical applications. The size of the PCB inductor is chosen to be 10 mm x 10 mm to comply with the size constraints of an implantable system. Inductors are designed using a commercial PCB manufacturing process where FR-4 is used as a substrate material.

The self-inductance of a conductor is derived by Grover [73, 74] as,

$$L_{self} = 2l\left\{ln\left(\frac{2l}{w+t}\right) + 0.5 + \left(\frac{w+t}{3l}\right)\right\} \tag{4-01}$$

where, L_{self} is the self-inductance, l is the length, w is the width, and t is the thickness of the conductor. Self-inductance of a straight conductor is given as [75],

$$L = 0.002l\left[ln\left(\frac{2l}{GMD}\right) - 1.25 + \frac{AMD}{l} + \left(\frac{\mu}{4}\right)T\right] \tag{4-02}$$

where, L is the inductance in, l is the conductor length, GMD and AMD represent the geometric and arithmetic mean distances, respectively, of the conductor cross section, μ is the conductor permeability, and T is a frequency-correction parameter. It is clear from the above equation that the self-inductance is proportional of the length of the conductor.

In presence of mutual inductance (M), the total inductance calculation is changed. Greenhouse first took into account the negative as well as the positive mutual inductances [75]. Negative mutual inductance results from the coupling between the two conductors having current vectors in opposite directions and the positive inductance results from the coupling between the two conductors having current vectors in the same direction. Total inductance can be calculated as [75],

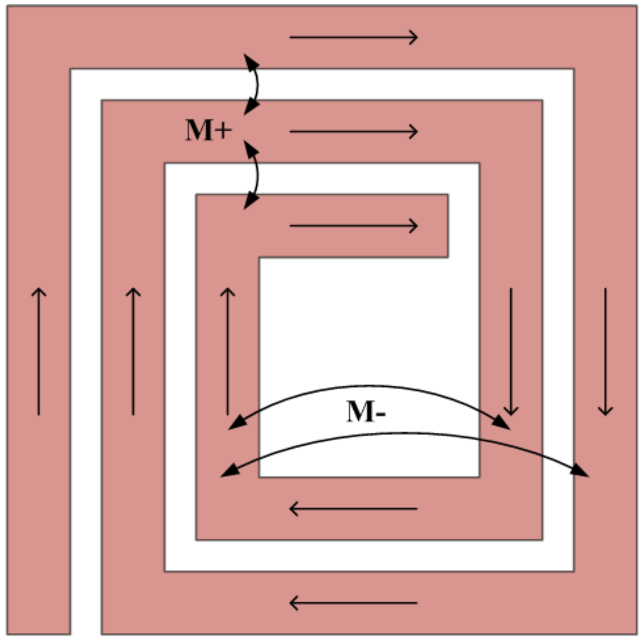

Figure 4-1: Positive and negative mutual inductance in a planar spiral inductor.

$$L_{Total} = \sum L_{self} + \sum M_{+} - \sum M_{-} \tag{4-03}$$

where, M_+ is positive mutual inductance and M_- is the negative mutual inductance as illustrated in Figure 4-1.

It is clear that the positive mutual coupling is additive towards the total inductance and the negative mutual coupling decreases the value of the total inductance. From equations (4-02) and (4-03), it is evident that inductance can be increased if the length of the metal trace is increased and if the effective mutual coupling between the metal lines functions as positive coupling. This concept is utilized and expanded to design the multi-stacked spiral solenoidal inductors. Flow of current in the designed

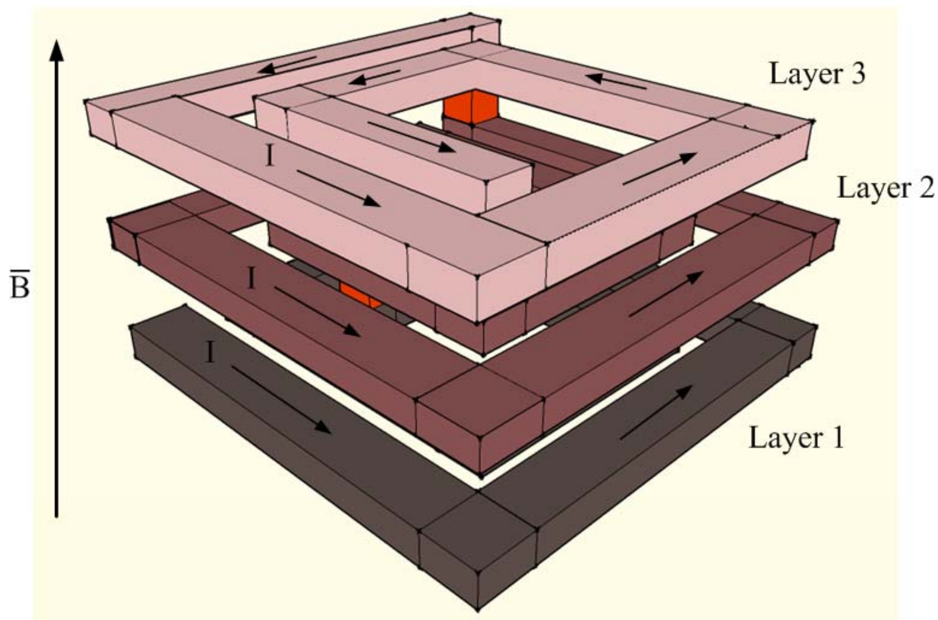

Figure 4-2: Concentric flow of current in a 3-layer PCB inductor and direction of the associated magnetic field.

inductor is shown in Figure 4-2. An inductor constructed using three level metal layer is shown here. Multi-level conductors are stacked and designed to form a solenoidal structure. The inductance of a solenoid is given by,

$$L = \frac{NA}{i} B \tag{4-04}$$

where, N is the number of turns, A is the area of the solenoid, i is the current flowing through the solenoid and B is magnetic flux density. It is clear from equation (4-04) that if the magnetic flux density of a solenoid is increased it will increase the overall inductance. By having a solenoidal structure the magnetic flux inside the loop increases, thereby increasing the overall inductance of the structure.

The inductors are designed and simulated using Sonnet Software [76]. The Sonnet Suites develop precise RF models (S-, Y-, Z-parameters or extracted SPICE model) for planar circuits and antennas. The software employs a rigorous method-of-moments (MoM) electromagnetic (EM) analysis based on Maxwell's equations that include all parasitic, cross-coupling, enclosure and package resonance effects. It divides the structure into subsections. It evaluates the electric field everywhere due to the current in a single subsection. It then repeats the calculation for every subsection in the circuit, one at a time. It effectively calculates the "coupling" between each possible pair of subsections in the circuit. An overview of Sonnet Software is given in the appendix section.

For simulation, the structure of a commercial 4-layer PCB is assumed with FR-4 as the substrate material and copper as the metal layer. For physical constraints, the size of the inductor is fixed to 10 mm x 10 mm. The inductors are simulated up to 100 MHz, considering the application for biomedical systems. L and Q can be calculated from the admittance parameter as follows,

$$L = \frac{Imag\left(\frac{1}{Y_{11}}\right)}{2\pi f} \tag{4-05}$$

$$Q = \frac{|Imag\ [1/(Y_{11})]|}{Re\ [1/(Y_{11})]} \tag{4-06}$$

Figure 4-3 (a) and Figure 4-3 (b) depict the top layer of the 4-layer inductor and the 3D view of the inductor in Sonnet, respectively.

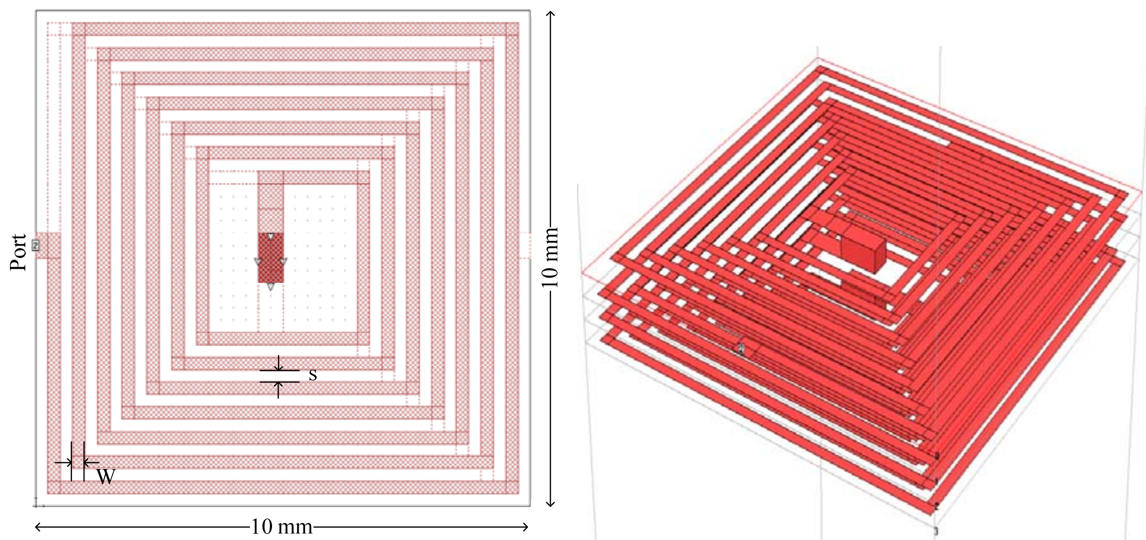

(a) (b)

Figure 4-3: (a) Top view of the designed 4-layer inductor (b) 3-D view of the designed inductor in Sonnet Software.

4.1.2 Mathematical Modeling of the PCB Inductor

a) Single Layer Spiral

For a single layer spiral inductor Mohan *et al.* [77] deemed following equation after Greenhouse [75], which is known as the 'Greenhouse formula'.

$$L = \frac{1.27\ \mu_0 n^2\ d_{avg}}{2}\left[ln\left(\frac{2.07}{\varphi}\right) + 0.18\varphi + 0.13\varphi^2\right] \tag{4-07}$$

$$\varphi = \frac{d_0 - d_i}{d_0 + d_i} \tag{4-08}$$

Where, n = number of turns, d_0 = outer diameter, d_i = inner diameters of the coil, φ = parameter known as fill factor, which changes from 0, when all the turns are concentrated

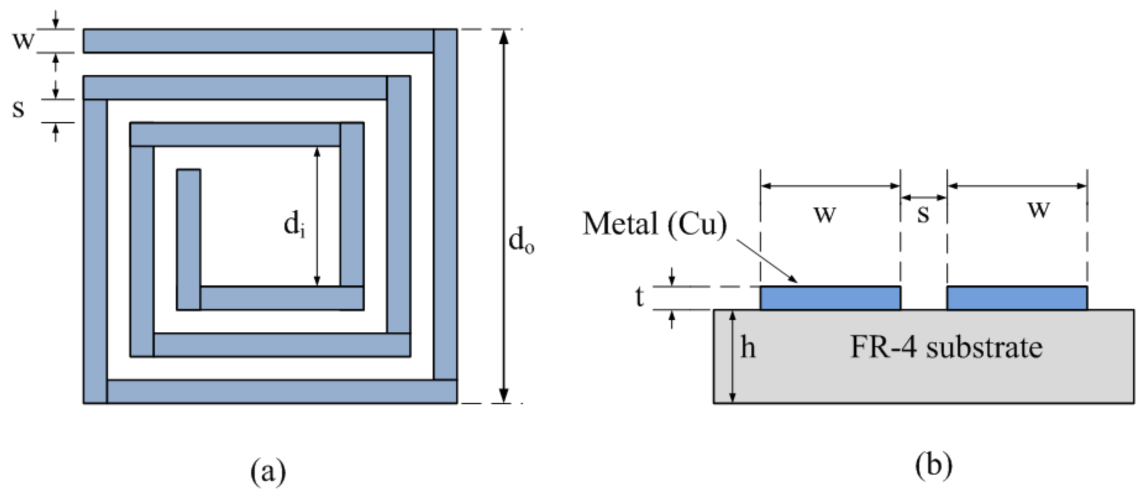

Figure 4-4: Geometrical parameters of a square-shaped PCB inductor. (a) Top view of the PCB inductor. (b) Side view of the PCB inductor.

on the perimeter like filament coils, to 1, when the turns spiral all the way to the center of the coil. All these geometric parameters are shown in Figure 4-4. To find the total parasitic DC resistance of the PCB inductor, the following parameters need to be calculated: the length of the conductive trace l_c, resistivity of the conductive material ρ_c, and its thickness t_c. The length of the conductive trace, l_c and the DC resistance, R_{dc} can be expressed as,

$$l_c = 4nd_0 - 4nw - (2n + 1)^2(s + w) \qquad (4\text{-}09)$$

$$R_{dc} = \rho_c \frac{l_c}{w\, t_c} \qquad (4\text{-}10)$$

where, w and s are the line width and the spacing, respectively.

The skin effect will increase the coil AC resistance at higher frequencies and should be taken into account. Considering the skin effect the equivalent series resistance, R_s is given by,

$$R_s = R_{dc}\left[\frac{t_c}{\delta\left(1 - e^{-t_c/\delta}\right)}\right] \tag{4-11}$$

$$\delta = \sqrt{\frac{\rho_c}{\pi\mu f}} \tag{4-12}$$

$$\mu = \mu_r\mu_0 \tag{4-13}$$

where δ is the skin depth, μ_0 is the permeability of space, and μ_r is the relative permeability of the conductor. Skin depth has some impact on the equivalent series resistance in the operating frequency range. Skin depth of copper at various frequencies is given in Table 4-1.

Table 4-1: Skin Depth of Copper in Various Frequencies

Frequency	***Skin Depth***
1 MHz	66 µm
10 MHz	20.89 µm
100 MHz	6.6 µm
1 GHz	2.09 µm

Considering standard 1 oz. copper method (weight of copper in a 1 square foot board), the thickness of copper in a single layer PCB is 35.56 μm. From Table 4-1, at 10 MHz the skin depth is 20.89 μm. Due to the skin effect most of the current will flow through this skin depth and there will be eventual rise in the resistance. The equivalent series resistance can therefore be written as,

$$R_s = \rho_c \frac{l_c}{w}\left[\frac{1}{\delta\left(1 - e^{-t_c/\delta}\right)}\right] \tag{4-14}$$

Thus, the quality factor of the PCB without its parasitic capacitance can be found by,

$$Q = \frac{\omega\, L}{R_s} \tag{4-15}$$

The length of the gap, l_g is slightly shorter than the length of the conductor and can be found from,

$$l_g = 4(d_0 - nw)(n-1) - 4sn(n+1) \tag{4-16}$$

There are two types of insulating materials affecting this capacitance. One is air or the coating insulator that fills the gap between adjacent traces. The other is the PCB substrate, which could be ceramic, polyimide, or FR-4. Therefore, C_p can be divided into C_{pc} and C_{ps} components as.

$$C_p = C_{pc} + C_{ps} = (\alpha\varepsilon_{rc} + \beta\varepsilon_{rs})\varepsilon_0 \frac{t_c}{s} l_g \tag{4-17}$$

Using Maxwell equations, M_{ij} between a pair of parallel circular single-turn coils at radii r_i and r_j can be found from,

$$M_{ij} = \mu\pi\sqrt{r_i r_j}\int_0^{\infty} J_1\left(x\sqrt{\frac{r_i}{r_j}}\right)J_2\left(x\sqrt{\frac{r_j}{r_i}}\right)J_0\left(x\frac{\gamma}{\sqrt{r_i r_j}}\right)exp\left(-x\frac{D}{\sqrt{r_i r_j}}\right)dx \tag{4-18}$$

where D is the relative distance between the two coils, μ is the permeability of the medium, and γ is the lateral misalignment, J_0 and J_1 are the Bessel functions of the zeroth and the first order, respectively. For perfectly aligned coaxial coils, $\gamma=0$, the equation can be written as,

$$M_{ij} = \frac{2\mu}{\alpha}\sqrt{r_i r_j}\left[\left(1-\frac{\alpha^2}{2}\right)K(\alpha) - E(\alpha)\right] \tag{4-19}$$

$$\alpha = 2\sqrt{\frac{r_i r_j}{\left(r_{i+}r_j\right)^2 + D^2}} \tag{4-20}$$

where, $K(\alpha)$ and $E(\alpha)$ are the complete elliptic integrals of the first and the second kind, respectively. By adding the partial mutual inductances between every two turns on a PCB inductor pair, the mutual inductance, M can be given as,

$$M = g\sum_{i=1}^{n1}\sum_{j=1}^{n2} M_{ij}\left(r_i, r_j, D\right) \tag{4-21}$$

where, g is a factor dependent on the shape of the PCB inductor. Even though the area of a square-shaped coil with a side length of $2r$ is 27% larger than a circular coil with equal diameter, it is empirically found that M between a pair of square-shaped PCB inductors is

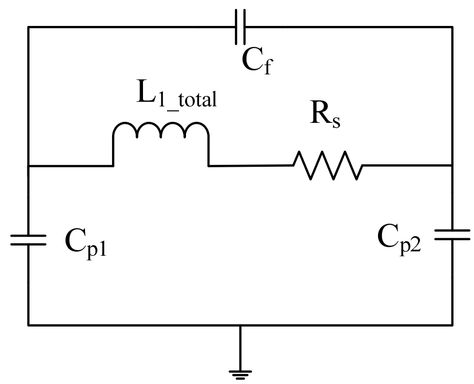

Figure 4-5: π-model of a single layer inductor.

only 10% higher than a pair of similar circular PCB inductors. Thus, g = 0.95, 1.0, and 1.1 for a pair of hexagonal, circular, and square-shaped PCBs with equal diameters, respectively [69]. For a single layer inductor the π-model can be shown in Figure 4-5.

b) <u>Stacked Inductor:</u>

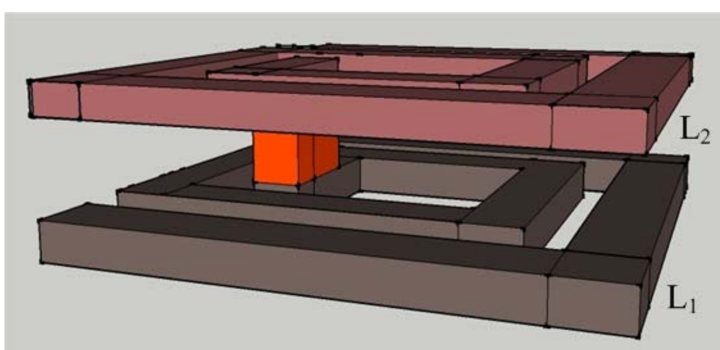

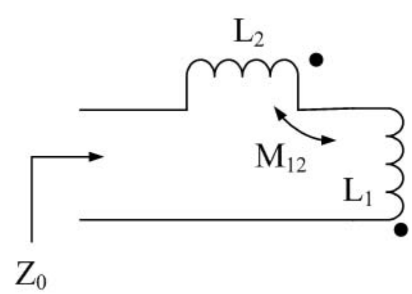

(a) (b)

Figure 4-6: a) Double layer stacked inductor and b) circuit showing mutual coupling between inductance of two metal layers.

For a two-layer stacked inductor (shown in Figure 4-6) the total inductance can be written as,

$$L_{2\_total} = L_1 + L_2 \pm 2M_{12} \tag{4-22}$$

Where, L_1 and L_2 are the inductance of layer 1 and layer 2, respectively and M_{12} is the mutual inductance between layer 1 and layer 2. In a stacked inductor if the spirals are identical then $L_1 = L_2 = L_1$ and the mutual coupling between two layers can be given as,

$$M_{12} = k_1\sqrt{L_1 L_2} = k_1 L_1 \tag{4-23}$$

k_1 = mutual coupling between metal layer 1 and metal layer 2. Total inductance of two layer inductor then becomes,

$$L_{2\_total} = 2L_1 \pm 2k_1 L_1 \tag{4-24}$$

For additive mutual coupling action of the structure the net inductance becomes,

$$L_{2\_total} = 2L_1 + 2k_1 L_1 \tag{4-25}$$

Similarly for a three-layer stacked inductor (shown in Figure 4-7) total inductance can be calculated as,

$$L_{3\_total} = L_1 + L_2 + L_3 \pm 2M_{12} \pm 2M_{23} \pm 2M_{13} \tag{4-26}$$

$$L_{3\_total} = 3L_1 \pm 4M_{12} \pm 2M_{13} \tag{4-27}$$

where, $L_1 = L_2 = L_3$ and $M_{12} = M_{23}$

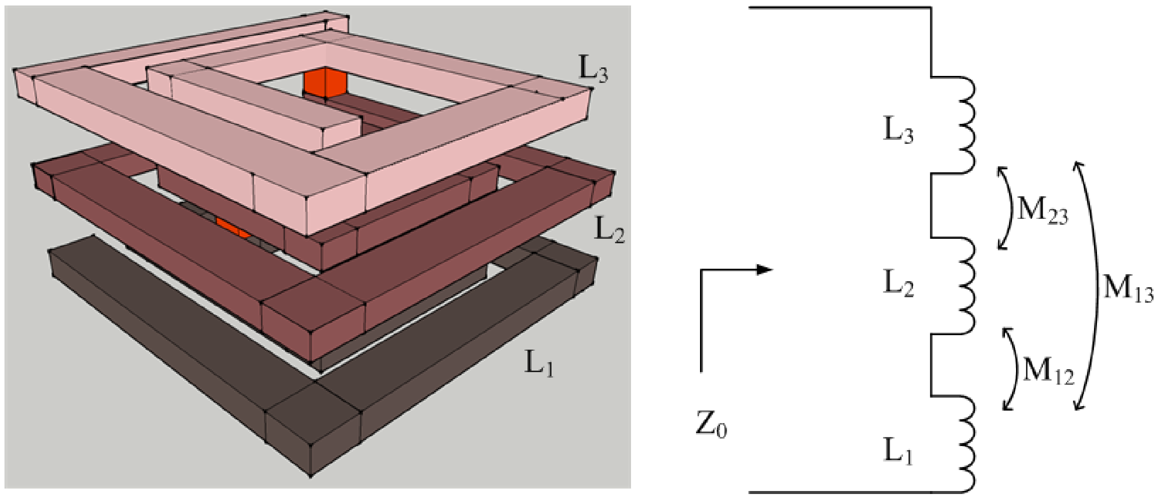

(a) (b)

Figure 4-7: a) Three layer stacked inductor. b) Circuit showing mutual coupling between metal layers.

Now,

$$M_{13} = k_2\sqrt{L_1 L_3} = k_2 L_1$$

Thus the equation (4-27) can be rewritten as,

$$L_{3\_total} = 3L_1 \pm 4k_1L_1 \pm 2k_2L_1$$

For additive mutual coupling action of the structure the net inductance becomes,

$$L_{3\_total} = 3L_1 + 4k_1L_1 + 2k_2L_1$$

$$L_{3\_total} = L_1(3 + 4k_1 + 2k_2) \tag{4-28}$$

Similarly for four-layer stacked inductor total inductance can be calculated as,

$$L_{4\_total} = L_1 + L_2 + L_3 + L_3 + L_4 \pm 2M_{12} \pm 2M_{23} \pm 2M_{34} \pm 2M_{13} \pm 2M_{24} \pm 2M_{14}$$

$$L_{4\_total} = 4L_1 \pm 6M_{12} \pm 4M_{13} \pm 2M_{14}$$

Where, $L_1 = L_2 = L_3 = L_4$ and $M_{12} = M_{23} = M_{34}$ and $M_{13} = M_{24}$

Now,

$$M_{14} = k_3\sqrt{L_1 L_4} = k_3 L_1$$

Thus the equation becomes,

$$L_{4\_total} = 4L_1 \pm 6k_1L_1 \pm 4k_2L_1 \pm 2k_3L_1$$

For additive mutual coupling action of the structure the net inductance becomes,

$$L_{4\_total} = 4L_1 + 6k_1L_1 + 4k_2L_1 + 2k_3L_1$$

$$L_{4\_total} = L_1(4 + 6k_1 + 4k_2 + 2k_3) \quad (4\text{-}29)$$

For i-layer stacked inductors,

$$L_{i\_total} = iL_1 + (i-1)2k_1L_1 + (i-2)2k_2L_1 + (i-3)2k_3L_1 + \cdots + \big((i-1)\big)2k_{i-1}L_1 \quad (4\text{-}30)$$

$$L_{i\_total} = L_1[i + (i-1)2k_1 + (i-2)2k_2 + \cdots + 2k_{i-1}] \quad (4\text{-}31)$$

Equivalent series resistance of the i-layer inductor can be expressed as,

$$R_i = iR_s = i\rho_c \frac{l_c}{w}\left[\frac{1}{\delta\left(1 - e^{-t_c/\delta}\right)}\right] \quad (4\text{-}32)$$

Equivalent capacitance of the i-layer inductor can be written as,

$$C_{p-i} = i(C_{pc} + C_{ps}) = i(\alpha\varepsilon_{rc} + \beta\varepsilon_{rs})\varepsilon_0 \frac{t_c}{s} l_g \tag{4-33}$$

The self-resonance frequency (SRF) of the inductor is given by,

$$f_{SRF} = \frac{1}{2\pi\sqrt{L_{eq}C_{eq}}} \tag{4-34}$$

The final set of equations for the equivalent π-model of the i-layer stacked PCB inductor is summarized in Table 4-2.

Table 4-2: Final Set of Equations for the Equivalent Pi-Model of the i-Layer Solenoid Stacked PCB Inductor

Parameter	Equation
Inductance	$L_{i\_total} = L_1[i + (i-1)2k_1 + (i-2)2k_2 + \cdots + 2k_{i-1}]$
Series Resistance	$R_i = iR_s = i\rho_c \frac{l_c}{w}\left[\frac{1}{\delta\left(1 - e^{-t_c/\delta}\right)}\right]$
Capacitance	$C_{p-i} = i(C_{pc} + C_{ps}) = i(\alpha\varepsilon_{rc} + \beta\varepsilon_{rs})\varepsilon_0 \frac{t_c}{s} l_g$
Self-Resonance Frequency	$f_{SRF} = \frac{1}{2\pi\sqrt{L_{eq}C_{eq}}}$

4.2 Effect of Variation of Design Parameter on PCB Inductor

There are four design parameters in the board level inductor design:

a. Number of the metal layers

b. Spacing between the metal traces

c. Width of the metal trace

d. Number of Turns

The effects of variation of design parameters are presented in the following sections.

4.2.1 Variation of Number of Metal Layers (l)

Inductors have been designed for the number of metal layers varying from 1 to 4 and the results are shown in Figure 4-8, and Figure 4-9. Inductors in multiple PCB layers are oriented in such a way that they keep a solenoidal structure and the mutual coupling between metal lines is constructively added to the overall inductance value. When the number of metal layer is increased it increases the length of the inductor which in turn increases the value of inductance. This characteristic follows the trend in equation (4-31). From Figure 4-8, it is evident that as the number of metal layers is increased the inductance value (L) is increased. This proves that proper stacking is an effective way to increase the inductance of a structure. Variation of the quality factor with increasing number of metal layers is shown in Figure 4-9 (a). For the operating frequency range Q remains almost similar for changes in the number of stacks. With the increase in number

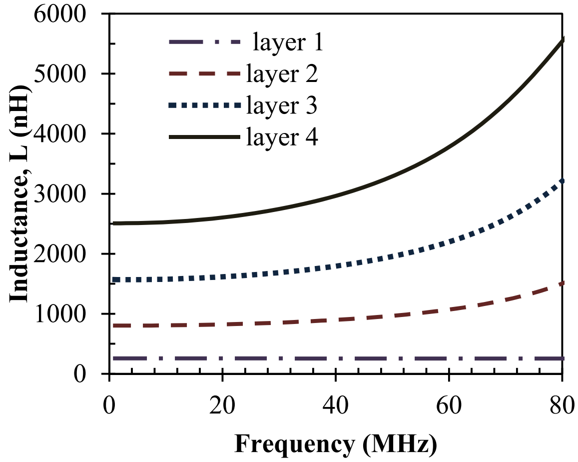

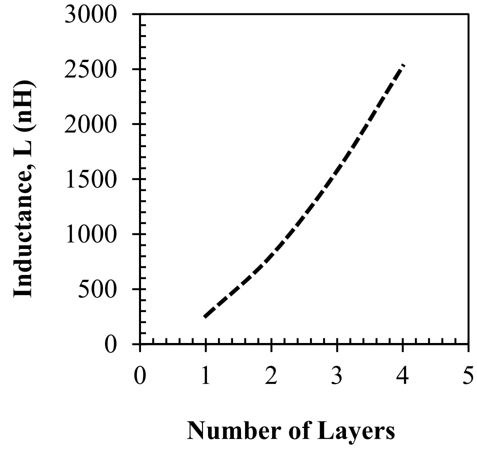

(a) (b)

Figure 4-8: (a) Effect of variation of number of metal layers on inductance with change in frequency. (b) Change of inductance at 13.56 MHz for changing metal layers. Both metal spacing (s) and width (w) are kept at 0.25 mm and number of turn is 6.

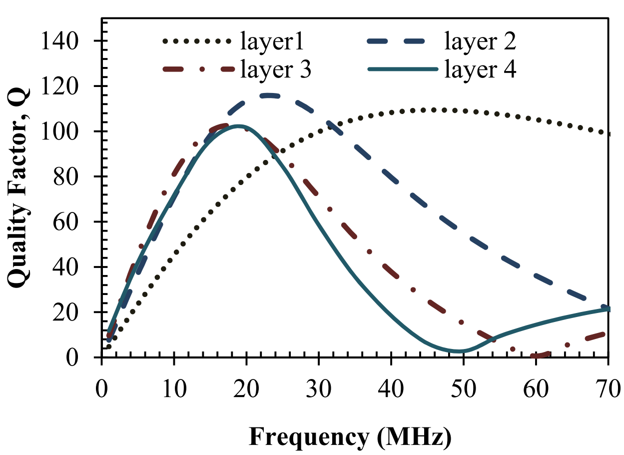

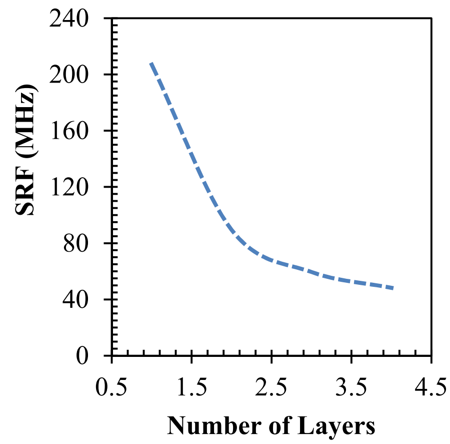

(a) (b)

Figure 4-9: (a) Effect of variation of number of metal layers on quality factor (Q). (b) Effect of variation of number of metal layers on self-resonance frequency (SRF). SRF values are obtained from (a). Both metal spacing (s) and width (w) are kept at 0.25 mm.

of metal stacks the value of inductance (L) and the series resistance (R_s) increases in same proportion. From the definition of Q in equation (4-15), it can be said that Q would remain same for a fixed frequency if L/R_s remains same. Stacking of metal layers also affect the self-resonance frequency (SRF) of the inductor. SRF is defined by equation (4-34) and it can also be defined by the frequency where $Q \simeq 0$. From Figure 4-9 (a), SRF for various numbers of metal layers can be determined and are plotted in Figure 4-9 (b). It can be seen from the figure that the increment of the number of layers reduces the SRF. Increasing the number of metal layer increases the inductance (L) and parasitic capacitances, thereby reducing the SRF.

4.2.2 Variation of Metal Spacing (s)

The spacing (s) between metal traces also changes the effective inductance value. The effect of the change in metal spacing from 0.25 mm to 0.75 mm is illustrated in Figure 4-10 (a) and (b). As the metal spacing is increased, the inductance is decreased. When the metal spacing is increased, the mutual coupling between the coils is decreased (see equation (4-19)) and as a result the overall inductance is decreased. Q remains almost same at the operating frequency (see Figure 4-11 (a)). Similarly, increase in the metal spacing reduces the inductance and the parasitic capacitance and consequently increases the SRF (see Figure 4-11 (b)).

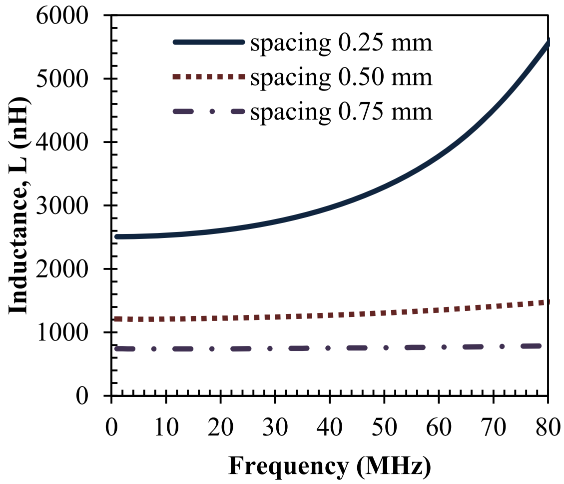

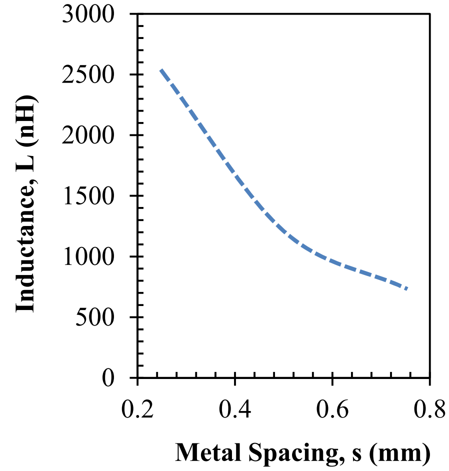

(a) (b)

Figure 4-10: (a) Effect of variation of spacing (s) between metal traces on inductance with change in frequency. (b) Change of inductance at 13.56 MHz for changing spacing (s). Metal width (w) is kept at 0.25 mm in a 4-layer design and number of turn is 6.

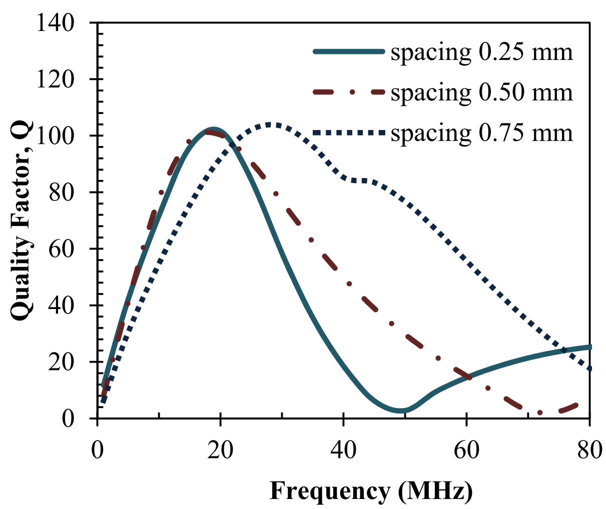

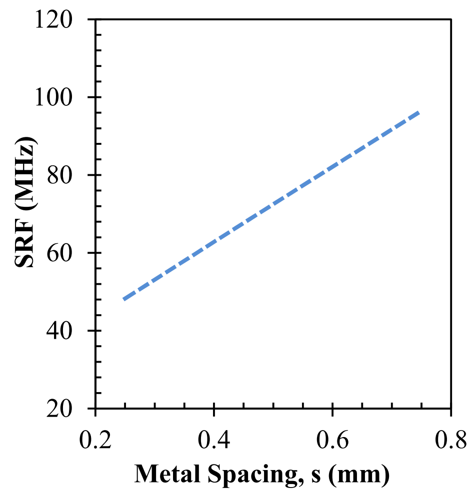

(a) (b)

Figure 4-11: (a) Effect of variation spacing between metal traces on quality factor (Q). (b) Effect of variation of spacing between metal traces on self-resonance frequency (SRF). SRF values are obtained from (a). Metal width (w) is kept at 0.25 mm in a 4-layer design.

4.2.3 *Variation of Metal Width (w)*

Inductance and SRF of the designed inductor are also affected by the variation of metal width (*w*). Metal width is varied from 0.25 mm to 0.75 mm and results are depicted in Figure 4-12 (a) and (b). Figure 4-12 (a) depicts the change of inductance with respect to frequency for various metal widths. From this figure, inductance of different metal widths at 13.56 MHz frequency is presented in Figure 4-12 (b). We can see that as the width of the metal is increased inductance is decreased. The effective length of the total conductor is decreased as a result of the increase in metal width leading to the decrease in the inductance. Q changes with the change in metal spacing but it remains almost same in the operating frequency of 13.56 MHz (see Figure 4-13 (a)). Change of metal width also affects the self resonance frequency. Increase in metal width reduces the inductance and the parasitic capacitance and consequently increases the SRF (see Figure 4-13 (b)).

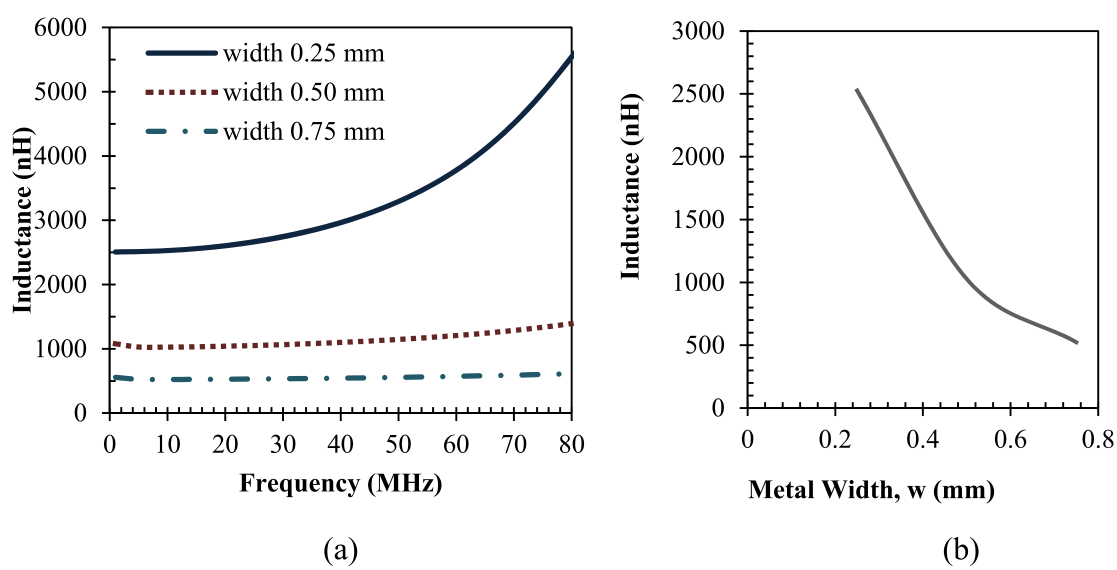

Figure 4-12: (a) Effect of variation of width (w) between metal traces on inductance with change in frequency. (b) Change of inductance at 13.56 MHz for changing width (w). Metal spacing (s) is kept at 0.25 mm in a 4-layer design and number of turn is 6.

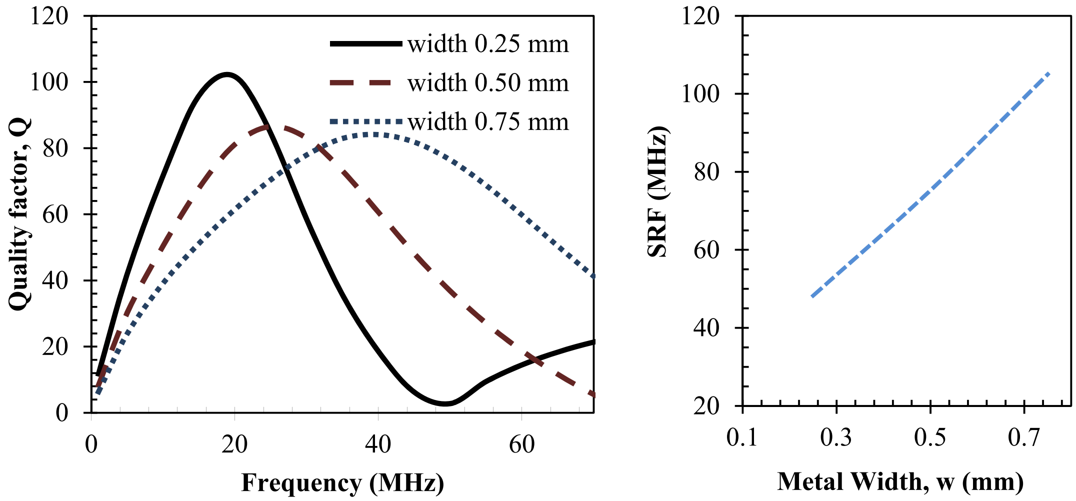

(a) (b)

Figure 4-13: (a) Effect of variation metal width (w) on quality factor (Q). (b) Effect of variation of metal width (w) on self-resonance frequency (SRF). SRF values are obtained from (a). Metal spacing (s) is kept at 0.25 mm in a 4-layer design.

4.2.4 Variation of Number of Turns (n)

The change of number of turns (n) affects the inductance and SRF of the proposed inductor. The results for the change in the number of turns from 2 to 6 are shown in Figure 4-14 (a) and (b). When the number of turns is increased, the effective length of the total conductor is increased consequently the inductance is increased. Even though Q changes with respect to frequency it remains almost same for various number of turns in the targeted operating frequency of 13.56 MHz (see Figure 4-15 (a)). Increasing the number of turns increases the inductance (L), parasitic capacitances between the metal layers and between metal tracks, thereby reduces the SRF (see Figure 4-15 (b)).

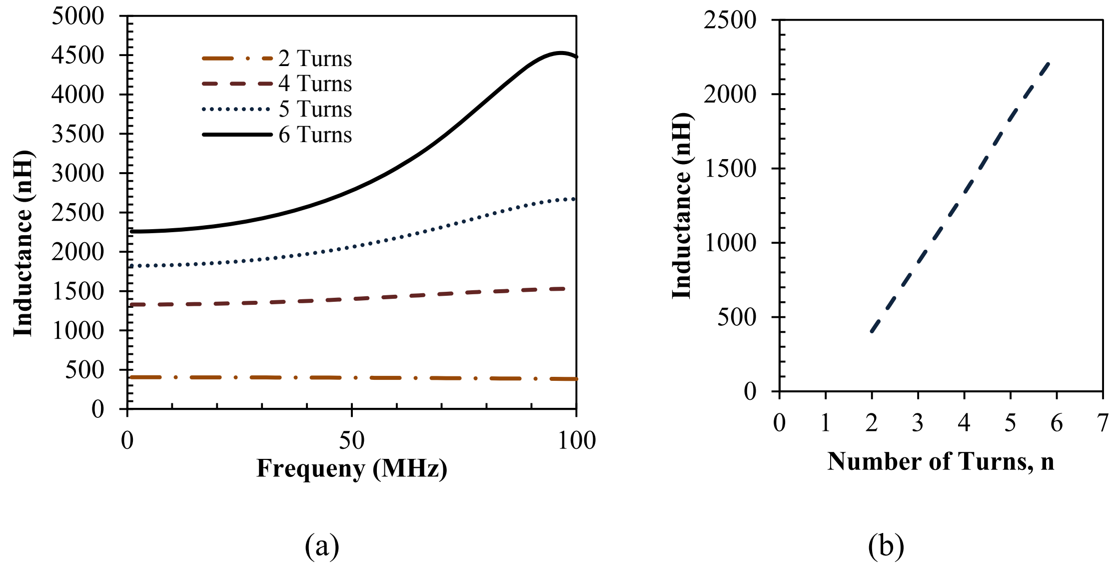

Figure 4-14: (a) Effect of variation of number of turn (n) between metal traces on inductance with change in frequency. (b) Change of inductance at 13.56 MHz for changing number of turns (n). Metal spacing (s) and metal width (w) are kept at 0.25 mm in a 4-layer design.

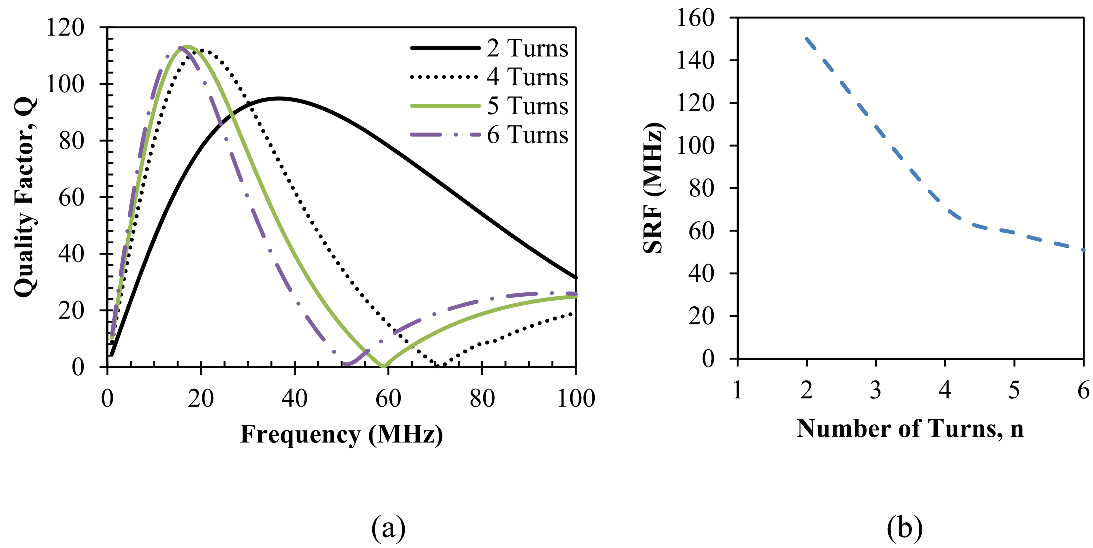

Figure 4-15: (a) Effect of variation number of turn (n) on quality factor (Q). (b) Effect of variation of number of turns (n) on self-resonance frequency (SRF). SRF values are obtained from (a). Metal spacing (s) and metal width (w) are kept at 0.25 mm in a 4-layer design.

4.3 Design Optimization of PCB Inductor

PCB inductor is optimized for biomedical applications. The target was to achieve highest possible inductance and the quality factor for the targeted 13.56 MHz band considering level of SAR in the human body. Figure of merit (FOM) of an inductor is defined by Tai *et al.* by [78]

$$FOM = \frac{L(nH)\ Q_{max}}{Area\ (mm^2)} \tag{4-35}$$

In this case, the Q at 13.56 MHz is considered instead of Q_{max} to optimize the design at the operating frequency. A new figure of merit, $FOM_{13.56MHz}$ is defined as,

$$FOM_{13.56\,MHz} = \frac{L_{13.56\,MHz}\ (nH) Q_{13.56\,MHz}}{Area\ (mm^2)} \tag{4-36}$$

The target of the optimization is to obtain the maximum possible $FOM_{13.56MHz}$ from the given design constraints. The effects of the variation of metal spacing, number of metal layers, metal width and number of turns with respect to $FOM_{13.56MHz}$ are plotted in

Figure 4-16. It is evident from the

Figure 4-16 (a), (b) and (c) that higher metal layer number, lower metal width, lower metal spacing and higher number of turns can lead to higher $FOM_{13.56MHz.}$ Effect of all four design parameters are summarized in

Figure 4-16 (d).

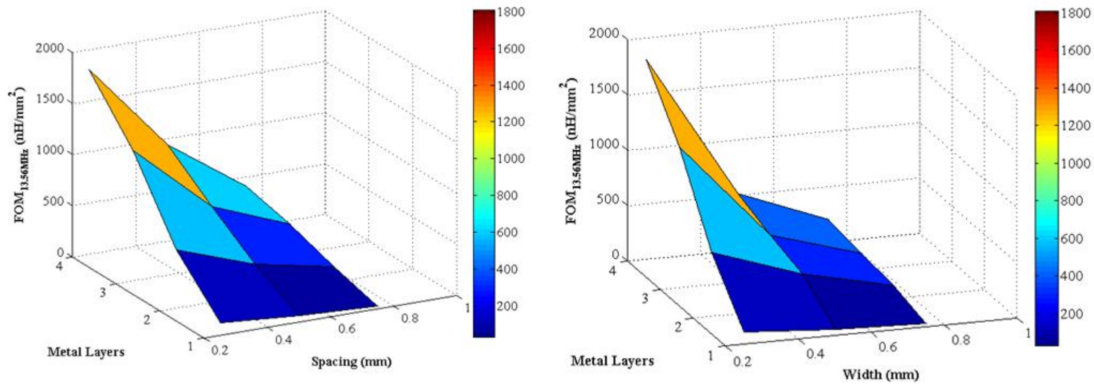

(a) (b)

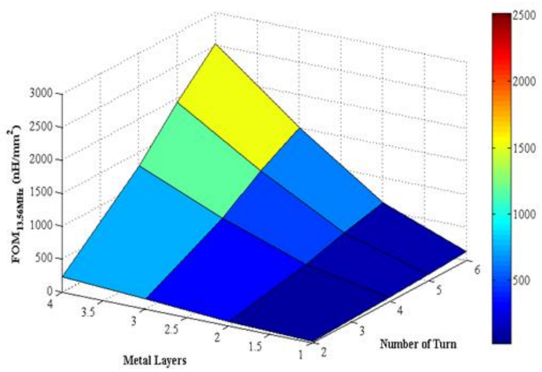

(c)

Variable	Change	FOM
Metal Layer	↑	↑
Metal Spacing	↑	↓
Metal Width	↑	↓
Number of Turn	↑	↑

(d)

Figure 4-16: Optimization of PCB inductor with respect to metal spacing, number of metal layers, width and number of turns. Higher $FOM_{13.56MHz}$ is obtained for higher metal layer (a) lower metal spacing, (b) lower metal width and (c) higher number of turns. (d) Effect of all four design parameters on $FOM_{13.56MHz}$.

The optimized design is shown in Figure 4-17. It demonstrates L and Q of inductor over a frequency range. This inductor shows promising performance in terms of L and Q particularly in the low frequency range, which is desirable for biomedical applications. The design parameters are summarized in Table 4-3. Current densities of the designed inductor are shown for 13.56 MHz and 90.25 MHz in Figure 4-18 and Figure 4-19, respectively. Current crowding effect is obvious in Figure 4-19.

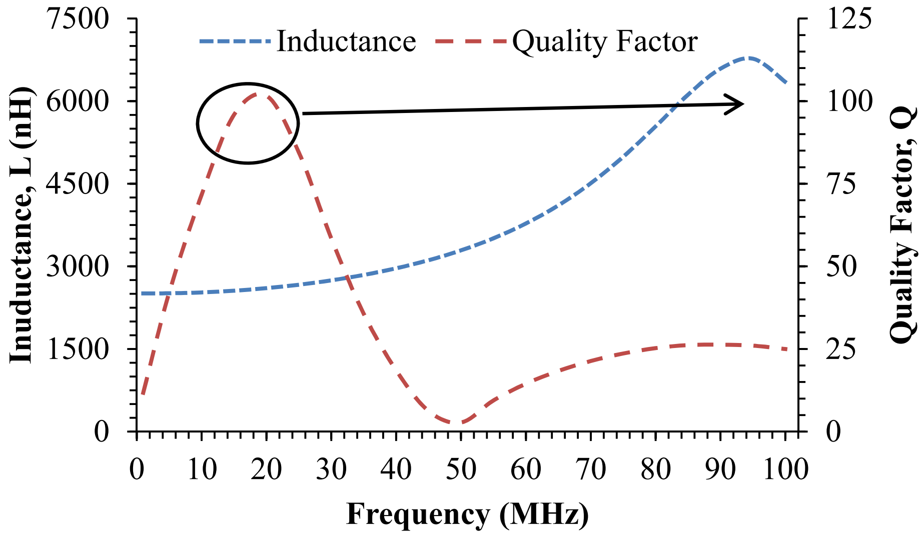

Figure 4-17: Inductance and quality factor of the optimized PCB inductor.

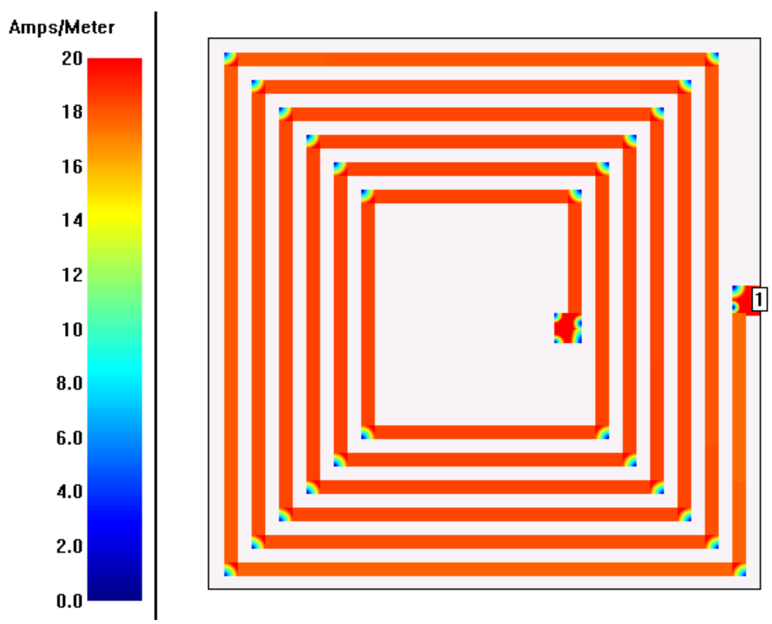

Figure 4-18: Current distribution of the top layer of the inductor at 13.56 MHz frequency.

Table 4-3: Design Summary of the Proposed PCB Inductor

Parameter	Simulated	Measured
Size	10 mm X 10 mm	10 mm X 10 mm
Number of turn	6	6
PCB material	FR-4	FR-4
Metal spacing	0.25 mm	0.25 mm
Metal width	0.25 mm	0.25 mm
Number of layer	4	4
Self-resonant frequency	48.25 MHz	37.9 MHz
Inductance, L (13.56 MHz)	2546.5 nH	3958.83 nH
Quality factor, Q (13.56 MHz)	89.8504	23.1
Peak quality factor, Q_{peak}	102.59 @ 18.75 MHz	27.17
Peak inductance, L_{peak}	6775.19 nH @ 95 MHz	7312.01 nH
FOM	2597.43	1075.61
$FOM_{13.56MHZ}$	1810.655	914.5

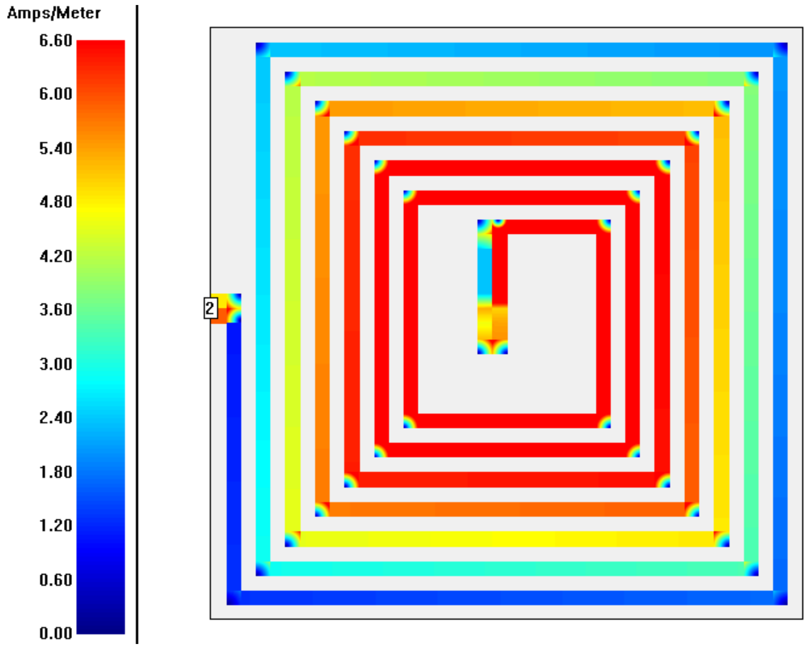

Figure 4-19: Current distribution of the top layer of the inductor at 90.25 MHz frequency.

4.4 Extraction of π-Model and Comparison with Mathematical Model

4.4.1 π-Model

Spice parameters have been extracted from sonnet simulation results. Sonnet provides a π-model of the inductor for a given frequency. Simulations have been done for various numbers of metal layers. The parameters of the PCB inductor are given in Table 4-4. For this structure parameters of the π-model is extracted as follows, (see Figure 4-20 (a)), L_1 = 149.3 nH, Rs_{-1} = 0.024Ω, Cp1 = 2.04 pF, C_{p2} = 0.85 pF.

Next, simulation is performed for a two-layer solenoidal spiral (see Figure 4-20 (b)).

Table 4-4: Parameters of PCB Inductor for π Model

Parameter	***Value***
Outer diameter	9.5 mm
Inner diameter	5.5 mm
Number of turns	4
Coil width	0.25 mm
Coil spacing	0.25 mm

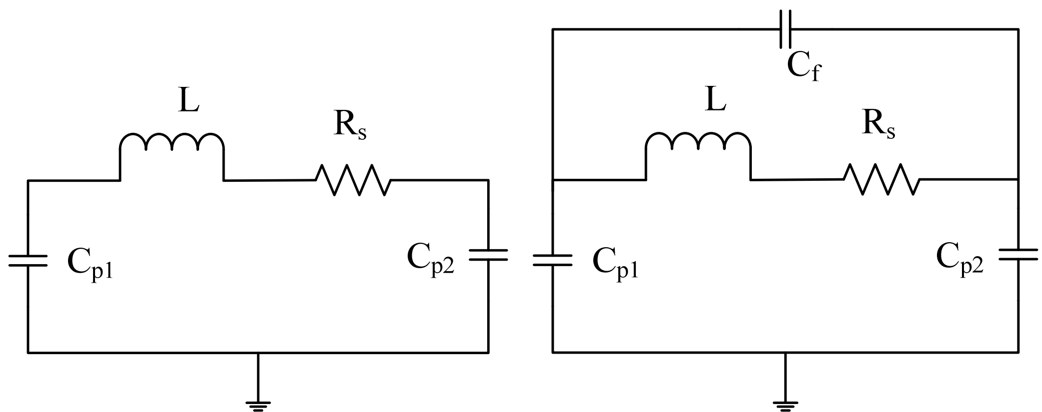

(a) (b)

Figure 4-20: π-model for a (a) single layer (b) multi-layer on-chip inductor.

where, $L_{2\text{-layer}}$ = 440.4 nH, $R_{s\text{-}2layer}$ = 0.473 Ω, C_{p1} = 1.645 pF, C_{p2} = 2.75 pF, C_f=1.1136 pF. Using equation (4-31), $L_{2-layer} = L_1[2 + 2k_1]$

Solving the equation one can get, k_1 =0.475

For a three-layer inductor the Spice parameters are found to be,

Where, $L_{3\text{-}layer}$ = 869.91 nH, $R_{s\text{-}3layer}$ =0.713 Ω, C_{p1} = 2.75 pF, C_{p2} = 3.15 pF, C_f= 0.48 pF.

Using equation (4-31),

$$L_{3-layer} = L_1[3 + 4k_1 + 2k_2]$$

Solving the equation one can get, k_2=0.463.

For a four-layer inductor the Spice parameters are found to be,

$L_{4\text{-}layer}$ = 1328.71 nH, $R_{s\text{-}4layer}$ = 0.928Ω, C_{p1} = 3.24 pF, C_{p2}=3.186 pF, C_f=0.48 pF.

Using equation (4-31),

$$L_{4-layer} = L_1[4 + 6k_1 + 4k_2 + 2k_3]$$

Solving the equation results in k_3 = 0.1.

4.4.2 Mathematical Model of Multi-Spiral PCB Inductor

Using 'Greenhouse formula', equation (4-07), the inductance and the resistance of a single-layer inductor can be calculated as, L_1= 200 nH, $R_{s\text{-}1}$=0.4339Ω. The inductance value is over-estimated compared to the simulated value. But the series resistance value is almost the same as the simulated value. It is empirically found that Greenhouse formula is approximately 26% higher than the simulated values. Greenhouse formula is modified and a good match between the simulated and the calculated values has been found,

$$L = 0.74\frac{1.27\,\mu_0 n^2\, d_{avg}}{2}\left[ln\left(\frac{2.07}{\varphi}\right) + 0.18\varphi + 0.13\varphi^2\right]$$

The modified Greenhouse formula can be written as,

$$L = 0.4699(\mu_0 n^2\, d_{avg})\left[ln\left(\frac{2.07}{\varphi}\right) + 0.18\varphi + 0.13\varphi^2\right] \tag{4-37}$$

Table 4-5: Simulated and Calculated Values of Inductance for PCB Inductor

Parameter	***Simulated***	***Calculated***
L_1	149.3 nH	149.27 nH
$L_{2\text{-layer}}$	440.4 nH	440.34 nH
$L_{3\text{-layer}}$	869.91 nH	869.64 nH
$L_{4\text{-layer}}$	1328.71 nH	1328.8 nH

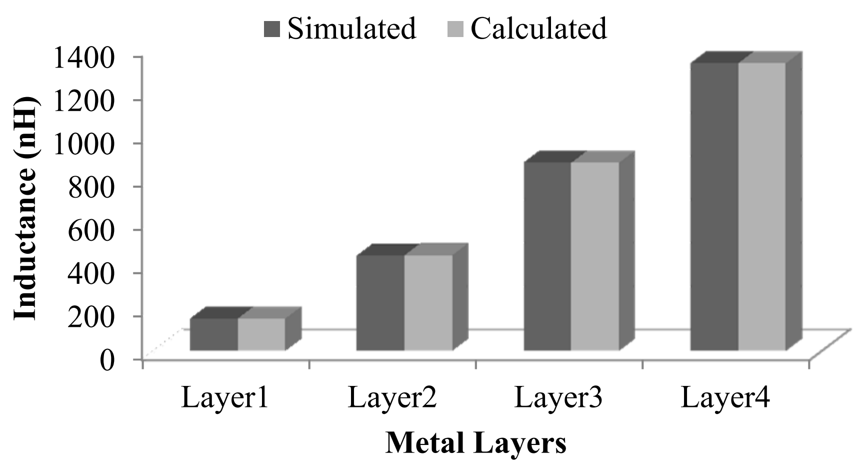

Figure 4-21: Comparison of simulated and calculated values of inductance for PCB inductors. Simulation is performed by Sonnet software and calculation is done by modified Greenhouse formula.

4.5 Measurement of the PCB Inductors

Different sets of inductors are fabricated using a commercial 4-layer PCB fabrication process. FR-4 is used as the substrate material. The fabricated inductor is shown in Figure 4-22 and the size of this inductor is compared with a penny. These inductors are measured using a 2-port Agilent E8363B PNA network analyzer. The network analyzer is calibrated by following the short-open-load-through (SOLT) calibration method using standard calibration kits. The setup of the measurement is shown in Figure 4-23. Measurements were taken from 10 MHz to 100 MHz frequency range. Using the network analyzer the *s*-parameters (s_{11}, s_{12}, s_{21}, and s_{22}) are measured for each inductor. Figure 4-24 shows the measured s_{11} parameter for an inductor from 10 MHz to 100 MHz frequency.

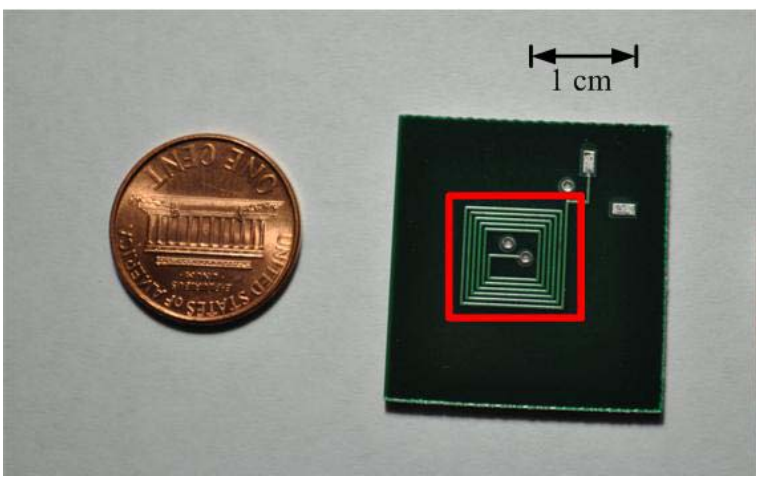

Figure 4-22: Size of the fabricated inductor (in red box) is compared with a penny.

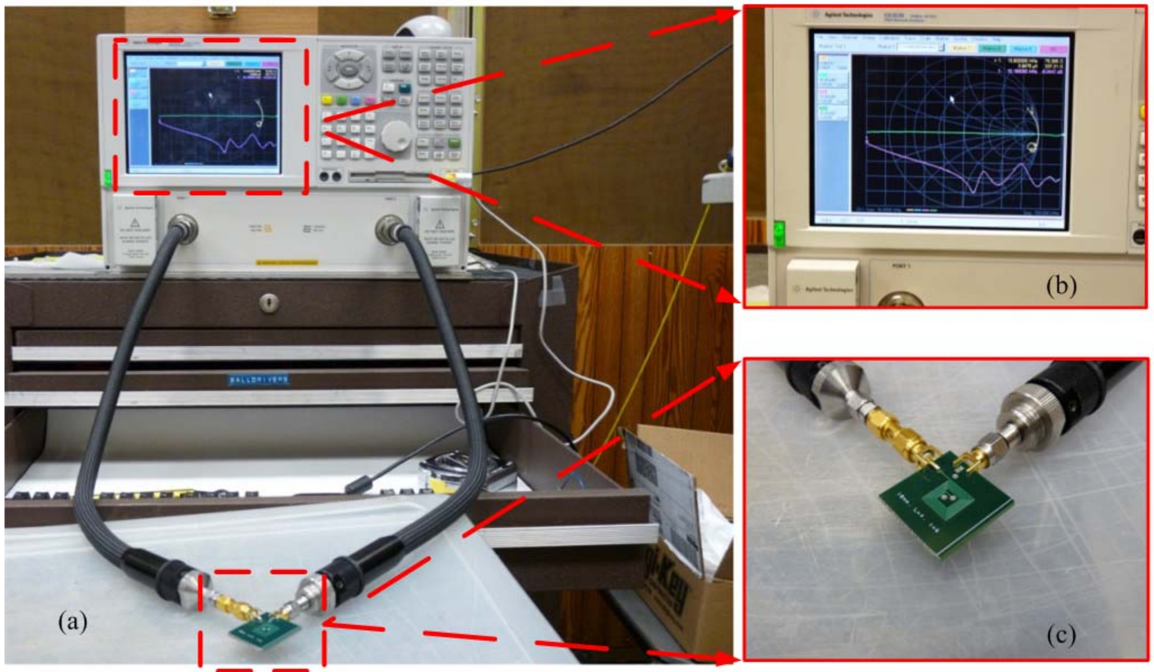

Figure 4-23: Setup for measuring PCB inductor. a) Measurement of PCB inductor with network analyzer. b) Close view of the network analyzer c) Close view of the PCB inductor.

A MATLAB® program is written to convert the *s*-parameters to *Y*-parameters and from the *Y*-parameter data the values of the inductance and the quality factor are calculated using equations (4-05) and (4-06). Inductors are fabricated using a 4-layer PCB process. Variation of inductance for changes in the number of metal layers is depicted in Figure 4-25(a). Inductance increases as the number of metal layers is increased. The measured and the simulated values of the inductance are compared in Figure 4-25(b) for 13.56 MHz frequency range. Although the value of the measured inductance is higher than the simulated data, they follow the similar trend. The variation

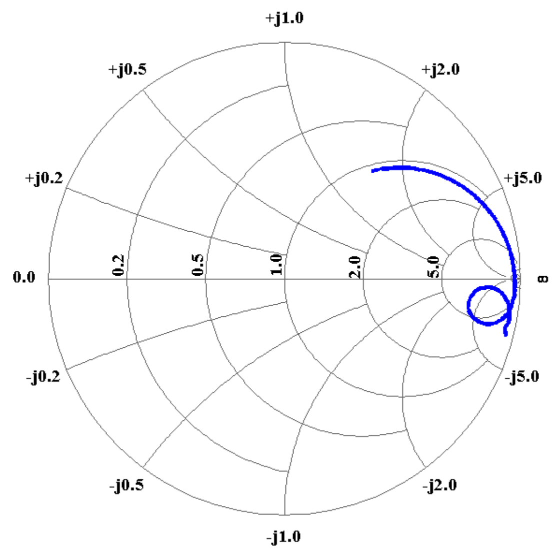

Figure 4-24: Smith chart of a PCB inductor showing measured S_{11} parameter from 10 MHz to 100 MHz frequency. Inductor parameter – the metal layer is 1, the number of turn is 6, the width is 0.25 mm, and the spacing is 0.25 mm.

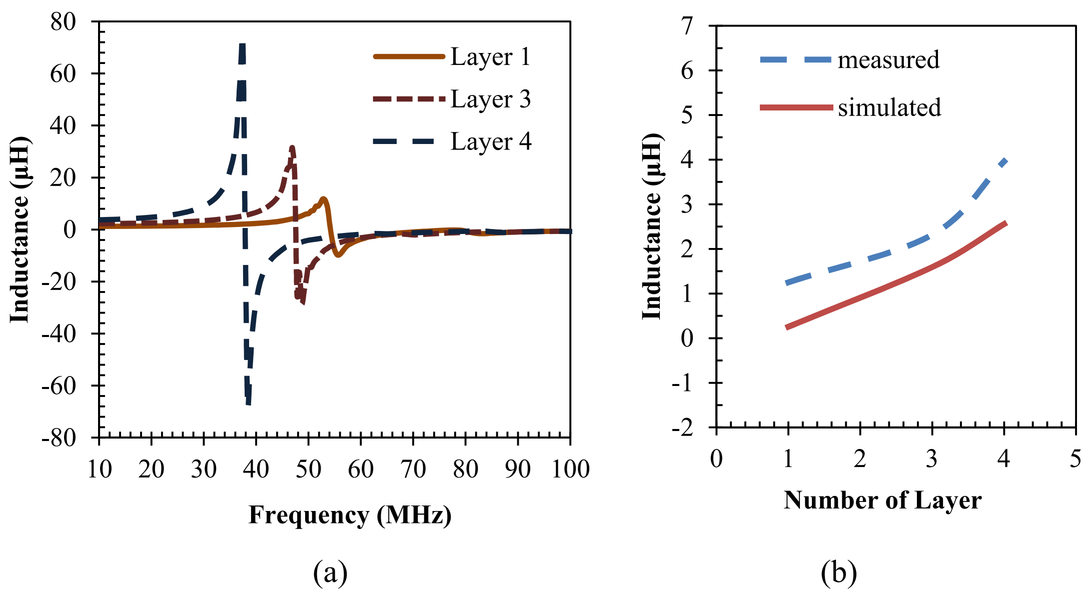

Figure 4-25: (a) Variation of inductance with number of metal layers for PCB inductor. (b) Comparison of inductance value between simulated and measured data for varying number of metal layers from 1 to 4 at 13.56 MHz frequency. In this figure, the number of turns is 6, the metal spacing is 0.25 mm, and the metal width is 0.25 mm.

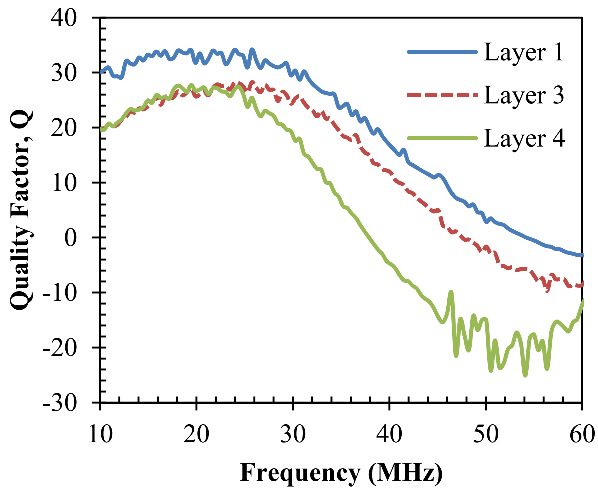

(a)

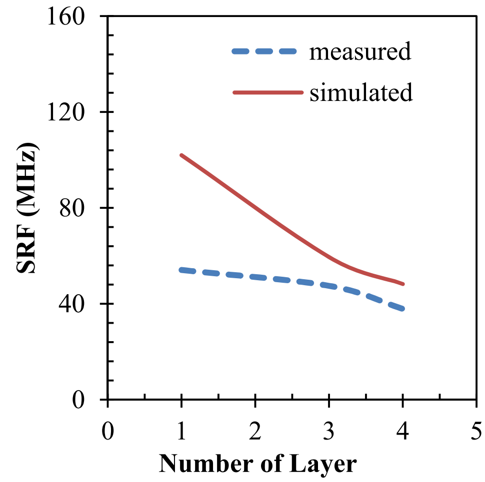

(b)

Figure 4-26: (a) Variation of quality factor with number of metal layers for PCB inductor. (b) Comparison between simulated and measured data of self-resonance frequency for various numbers of metal layers of PCB inductor. In this figure, the number of turn is 6, the metal spacing is 0.25 mm, and the metal width 0.25 mm.

is attributed to setup of the simulator as well as the condition of the measurement. While setting up the simulation it is assumed that the properties of the metal are ideal, dielectric layer is the ideal FR-4, and there is no electromagnetic interference present in the system. In the measurement, errors can come from calibration, contact resistance, connectors, electromagnetic interference, etc.

Variation of the quality factor for increase in metal layers is illustrated in Figure 4-26(a). From this data, the self-resonance frequency values for various metal layers are calculated and plotted in Figure 4-26(b). It can be seen from Figure 4-26 (a) that layer 1 shows the highest Q value at the operating frequency and other layers show similar Q values. The simulated and the measured data of SRF are also compared in Figure 4-26(b).

Although the simulated values of SRF are higher than the measured values, they follow the similar trend of decreasing with the increase in number of metal layer. Possible causes of this variation are discussed earlier.

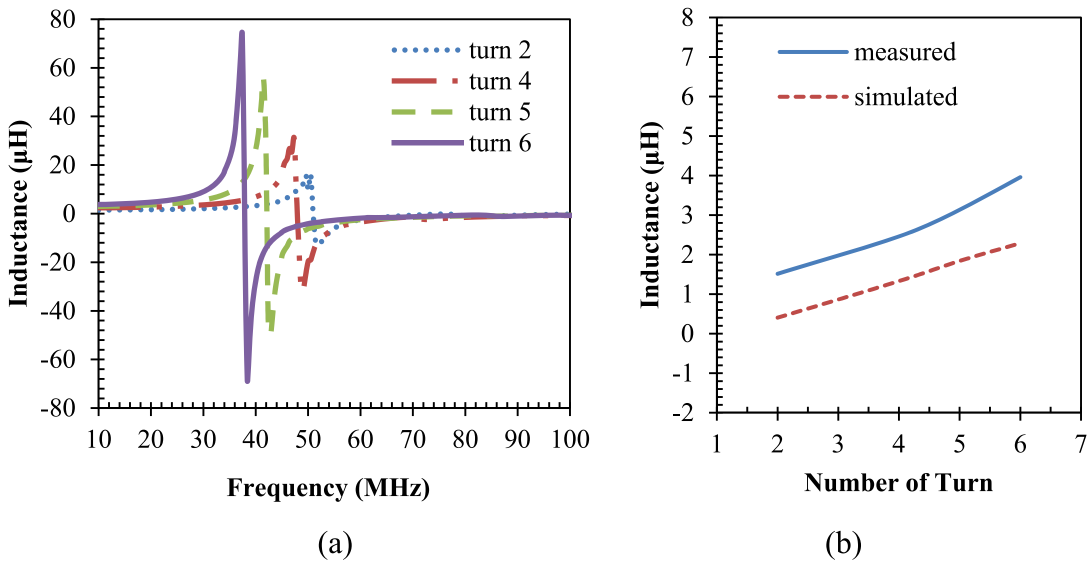

Figure 4-27: (a) Variation of inductance with number of turn for PCB inductor. (b) Comparison between simulated and measured data of inductance with the increase in number of turn for PCB inductor for 13.56 MHz frequency. In this figure, the number of layer is 4, the metal spacing is 0.25 mm, and the metal width is 0.25 mm.

The number of turn is varied from 2 to 6 for 4-layer PCB inductors. The variation of the inductance with the increase in the number of turn is illustrated in Figure 4-27(a). As the number of turn is increased the inductance is increased following the Greenhouse formula, equation (4-07) as shown in Figure 4-27(b). Simulated and measured values of inductance are also compared in Figure 4-27(b). Measured values show higher inductance than the simulated values. The quality factor and the SRF values for various number of turns are plotted in Figure 4-28(a) and (b), respectively. It can be seen from Figure

4-28(b) that measured values of SRF are lower than simulated values. The causes of this variation are discussed in the previous section.

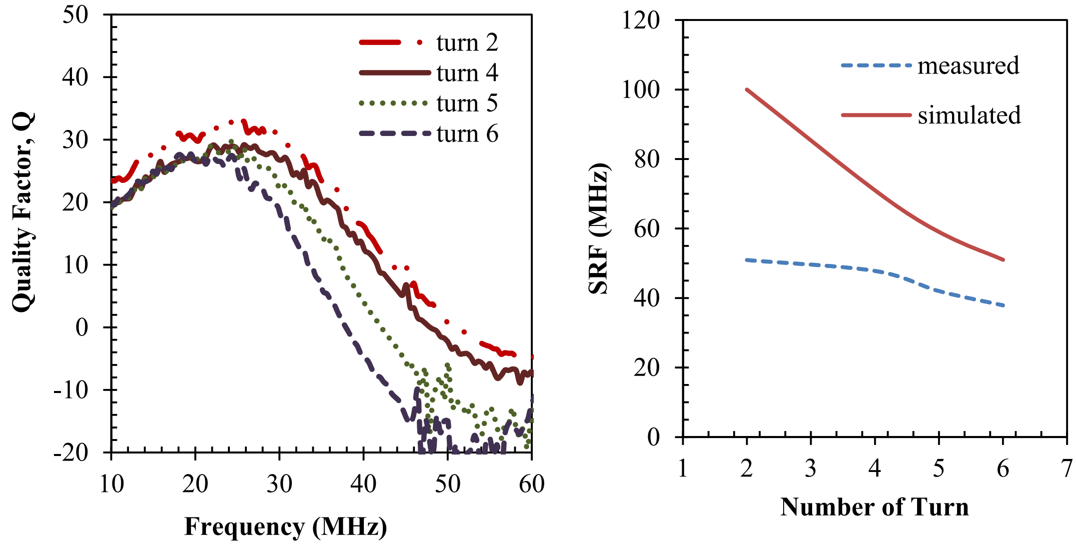

(a) (b)

Figure 4-28: (a) Variation of quality factor with number of turn for PCB inductor. (b) Comparison between simulated and measured data of self-resonance frequency with the increase in number of turn for PCB inductor. In this figure, the number of metal layer is 4, the metal spacing is 0.25 mm, and the metal width is 0.25 mm.

The metal width is varied from 0.25 mm to 1 mm for 4-layer PCB inductors. The variation of the inductance with the increase in the metal width is measured and depicted in Figure 4-29(a). The inductance is decreased with increase in metal width which is shown in Figure 4-29(b) and the measured values are compared with simulated values for 13.56 MHz frequency. Measurement results confirm the statement that increases in metal width decreases the inductance value. As discussed earlier, measured values show higher inductance than the simulated values due to various reasons.

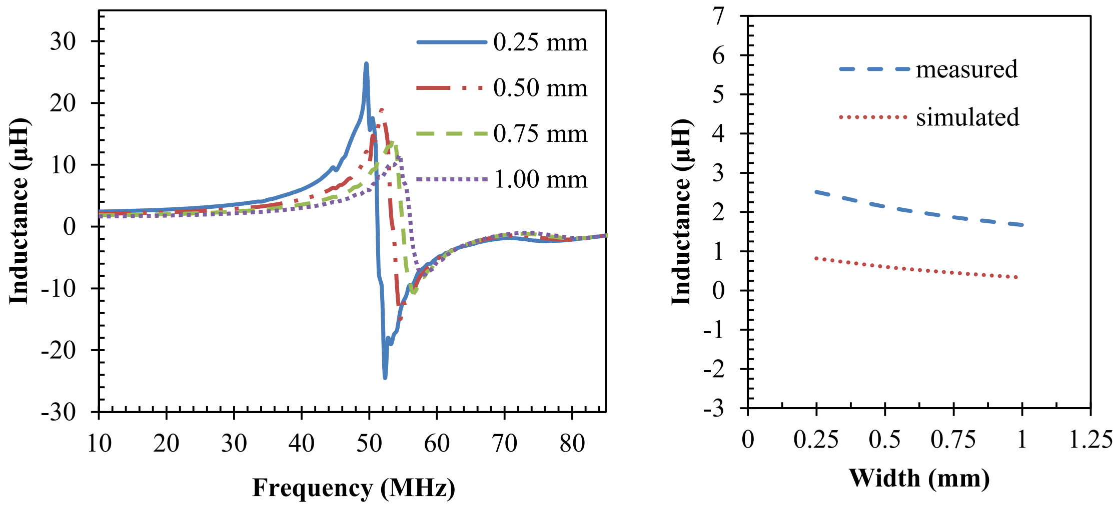

(a) (b)

Figure 4-29: (a) Variation of inductance with metal width for PCB inductor. (b) Comparison between simulated and measured data of inductance with the increase in metal width for PCB inductor for 13.56 MHz frequency. In this figure, the number of layer is 4, the metal spacing is 0.25 mm, and number of turns is 6.

Total 5 Inductors are designed with metal spacing varying from 0.25 mm to 1.25 mm and all other design parameters are kept constant (number of layer 4, metal width 0.25 mm, and number of turns 6). Measurement results are shown in Figure 4-30 (a) and (b). For 13.56 MHz frequency, measured values of inductance are compared with simulated values in Figure 4-30 (b). It is evident that increase in metal spacing decreases the inductance for a given frequency of operation. Similar to previous trends, measured values of inductance are higher than the simulated values.

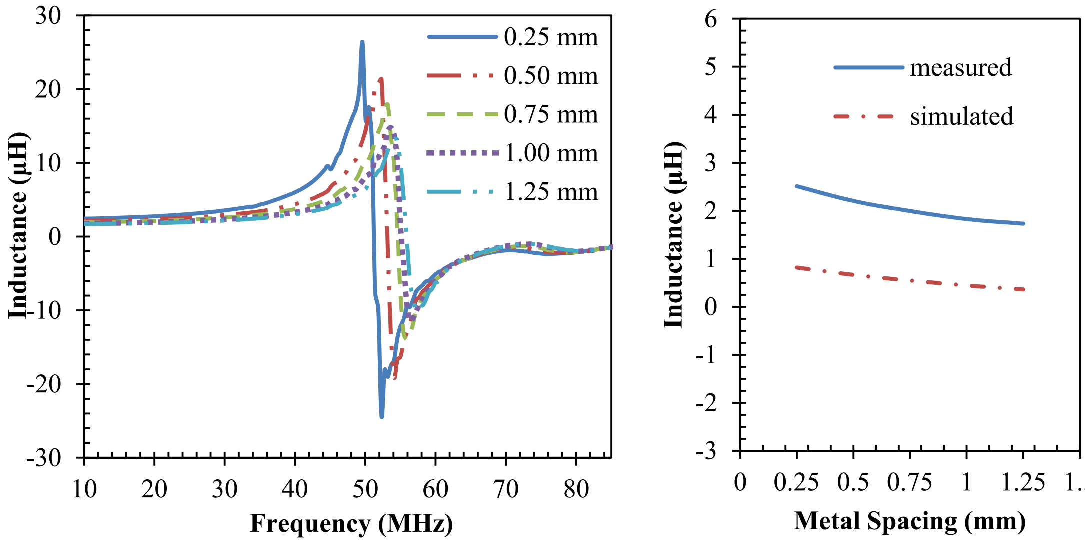

(a) (b)

Figure 4-30: (a) Variation of inductance with metal spacing for PCB inductor. (b) Comparison between simulated and measured data of inductance with the increase in metal width for PCB inductor for 13.56 MHz frequency. In this figure, the number of layer is 4, the metal width is 0.25 mm, and number of turns is 6.

4.6 Comparison with State of the Art Work

Jow *et al.* have reported works on PCB inductors for biomedical applications [47, 69, 79, 80]. The proposed work is compared with Jow's work [79] for the same frequency and the outer diameter of inductor and is shown in Table 4-6. As can be seen from the table, for the same outer diameter and the frequency the proposed design shows better result in terms of the inductance value, and $FOM_{13.56MHz}$. Although the SRF value of this work is found to be 37.9 MHz, it is still much higher than targeted operating frequency of 13.56 MHz. Therefore it will not affect the operation of the inductive link. In a nutshell, this design increases the density of inductance or reduces the size of inductor for same size which is very beneficial for implantable biomedical systems.

Table 4-6: Comparison of Proposed Work with State of the Art PCB Coil Design for Biomedical Implants

Design Parameter	***Jow* et al. *[79]***	***Proposed work***
Frequency	13.56 MHz	13.56 MHz
Outer diameter	10 mm	10 mm
Number of turn	6	6
Metal spacing	0.15 mm	0.25 mm
Metal width	0.2 mm	0.25 mm
Number of layer	1	4
Inductance, L (13.56 MHz)	510 nH	3958.83 nH
Quality factor, Q (13.56 MHz)	60	23.1
Self-resonant frequency	525 MHz	37.9 MHz
Inductance density, nH/mm^2	5.1	39.59
$FOM_{13.56MHz}$	306.00	914.5

This work is compared to PCB inductor designs reported in literature in Table 4-7. To have a fare comparison the FOM defined at Equation (4-35) has been utilized instead of $FOM_{13.56MHz}$. It is found that this work shows highest FOM with respect to other works. This proves that the multi-spiral solenoidal structure is a successful method of designing high performance inductors.

Table 4-7: Comparison of Designed PCB Inductor with Reported Works in Literature

Reference	*L (nH)*	Q_{max}	*Area (mm²)*	*FOM*
This work - PCB	3958.83	27	100	1068.88
Jow et al. [69]	510.00	60	100	306.00
Masuch et al. [81]	273.00	42.1	25	459.73
Peters et al. [82]	4013.00	44	2482	71.14

4.7 Conclusion

In this chapter, design of multi-spiral PCB inductor for biomedical applications has been discussed. Multi-spiral solenoidal stacking method has been proposed to increase the inductance density of PCB inductors. A figure of merit based optimization technique has also been introduced. Method of moment based electromagnetic simulation has been done to design and optimize the inductors. A π-model for the multi-spiral inductor is also proposed based on the empirical formulas. PCB inductors are fabricated using a commercial 4-layer fabrication process. Measurements have been carried out and the results are compared with the simulation results. The designed PCB inductor is also compared with works reported in literature. The proposed inductor exhibits highest FOM value compared to state of the art works. It manifests that the multi-spiral solenoidal scheme is a successful method of designing inductors with higher inductance density. This technique would be useful in designing smaller footprint inductors which could be implanted inside human body for wireless power transfer in biomedical instrumentations.

Chapter 5

TOWARDS THE DESIGN OF ON-CHIP INDUCTOR

5.1 Loss Mechanisms in On-Chip Inductors

Designing high quality integrated inductors remain a great challenge for designers due to various issues. The quality factor of the integrated passive inductors is determined by the characteristics of the substrate and the metallization of the process in which they are fabricated. Loss mechanisms of integrated inductors are shown in Figure 5-1 and are discussed in detail by Niknejad [83] and Aguilera [84].

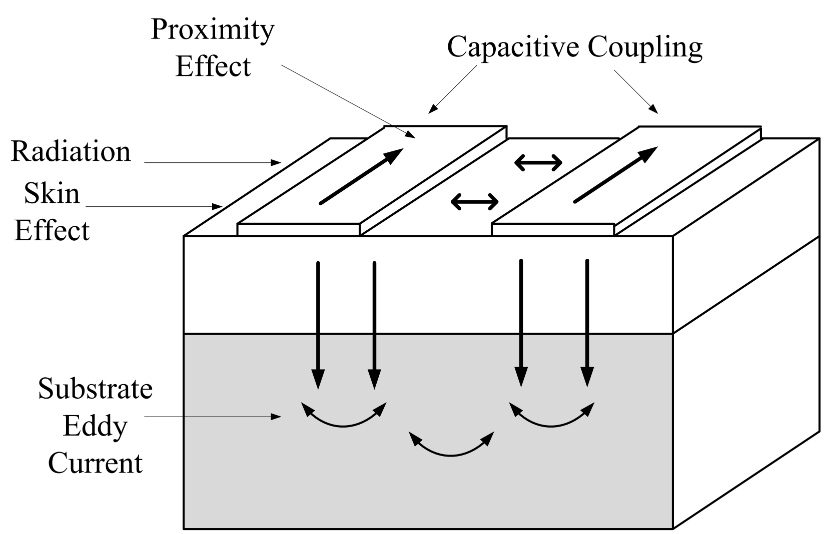

Figure 5-1: Loss mechanisms in on-chip inductors. Low inductance and low Q values of on-chip inductors are due to these loss mechanisms.

The main losses are due to, skin effect in metal traces due to high frequency of AC current, proximity effect due to near metal tracks, radiation, capacitive coupling between metal lines, and substrate eddy current loss. If a time varying voltage is applied across an integrated inductor, electric and magnetic fields are created and they interact with the structure of the on-chip inductor (see Figure 5-2). A brief description of these fields is given below.

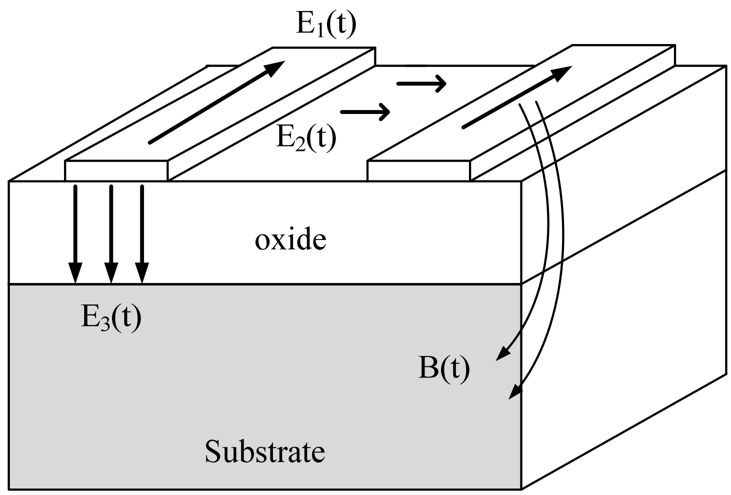

Figure 5-2: Representation of physical effect on integrated inductors when a time varying voltage is applied.

Due to presence of time varying current induced magnetic field, B(t), the self and the mutual inductance coupling among the metal layers are generated. Current is also induced in the substrate and the metal tracks. Electric field along the spiral, $E_1(t)$ generates Ohmic losses in the spiral due to the resistivity of the metal layers. Electric field passing through the oxide between strips, $E_2(t)$ builds the capacitive coupling among the coils of the inductor. Electric field passing through the oxide and the substrate, $E_3(t)$

produces capacitive coupling between the metal layer and the substrate and Ohmic losses in the substrate due to displacement currents induced through the capacitive coupling between the spiral and the substrate.

5.2 **Inductor Parameters**

5.2.1 Inductance

The inductance of a planar spiral is given by [85],

$$L = \frac{\mu_0 n^2 d_{avg} c_1}{2}[ln\left(\frac{c_2}{\rho}\right) + c_3\rho + c_4\rho^2] \tag{5-01}$$

where L is inductance, μ_0 is permeability of free space, d_{avg} is average diameter of the inductor, n is number of turns, c_n is function of geometry given in Table 5-1 and ρ is the fill factor. ρ is defined as, $\rho = (d_{out} - d_{in})/(d_{out} + d_{in})$, where, d_{out} is the outer diameter and d_{in} is the inner diameter of the inductor.

Table 5-1: Coefficients for the Inductance Formula for Equation (5-01)

Shape	c_1	c_2	c_3	c_4
Square	1.27	2.07	0.18	0.13
Hexagon	1.09	2.23	0.00	0.17
Octagon	1.07	2.29	0.00	0.19
Circle	1.00	2.46	0.00	0.20

For other type of polygons inductance can be given as,

$$L = \frac{\mu_0 n^2 d_{avg} A_{out}}{\pi d_{out}^2}\left[ln\left(\frac{2.46 - {}^{1.56}/_{N}}{\rho}\right) + \left(0.2 - \frac{1.12}{N^2}\rho^2\right)\right] \tag{5-02}$$

Where A_{out} is the area computed with the outer dimensions and N is number of sides of the polygon.

5.2.2 Resistance

Resistance of a conductor is given by,

$$R = \rho\frac{L}{A} \tag{5-03}$$

where, ρ is the resistivity, L the length and A the area of the conductor area. With the increase in frequency, the resistivity of the conductor changes due to the skin effect. Neighboring metal layers also have an effect on the resistance due to the proximity effect.

Skin Effect

The skin effect in a conductor accounts for the alteration of the current density distribution from the magnetic field generated by the current itself. The current density becomes largest near the surface of the conductor and decreases at greater depths. The electric current flows mainly at the "skin" of the conductor, at an average depth called the skin depth. Skin depth is given by,

$$\delta = \sqrt{\frac{2}{\mu.\sigma.\omega}} \tag{5-04}$$

Where μ is the magnetic permeability of the material, σ is the conductivity and ω is the angular frequency. Skin depth can be related with resistivity as,

$$\rho = \frac{1}{\sigma.\delta} = \sqrt{\frac{\pi.f.\mu}{\sigma}} \tag{5-05}$$

Generally Aluminum is used as the metal layer in semiconductor process. Skin depth of Aluminum at various frequencies is shown in Table 5-2. In some higher-end processes copper is used as the metal layer. The skin depth of Copper is listed in Table 4-1.

Table 5-2: Skin Depth of Aluminum in Various Frequencies

Frequency	***Skin Depth of Aluminum***
0.1 GHz	8.50 μm
1 GHz	2.69 μm
2 GHz	1.90 μm
5 GHz	1.20 μm

Proximity Effect

Proximity effect is the consequence of the influence of an external time-varying magnetic field over the conductor. A changing magnetic field will influence the distribution of an electric current flowing within an electrical conductor. When an alternating current (AC) flows through an isolated conductor, it generates an associated alternating magnetic field. The alternating magnetic field induces eddy currents in adjacent conductors, altering the overall distribution of the current flowing through them. The proximity effect can significantly increase the AC resistance of adjacent conductors when compared to its resistance to a DC current. The effect increases with frequency. At higher frequencies, the AC resistance of a conductor can easily exceed ten times its DC resistance. In case of an alternating current, the skin effect and the proximity effect will add together, changing the current distribution and increasing the resistance of the conductor.

5.2.2 Inductor Model

Various circuit models have been proposed for integrated inductors such as π-model [86-88], transformer model [89] and the wideband π-model [90]. Among them π-model is mostly used for simplicity. A simple two-port π-model is shown in Figure 5-3. In the figure, C_P accounts for both the capacitance among the strips and between the strips and the coil inner connection. In addition, its value is usually negligible. R_s represents the inductor resistance and accounts for the Ohmic losses due to the metal track resistance, induced effects in the metallic conductor, and the magnetic field induced currents in the substrate; L_s models the inductance of the coil; C_{OX} represents the parasitic capacitance between the metal of the spiral and the substrate. R_{si} accounts for the Ohmic losses in the substrate produced by the displacement currents induced in the substrate,

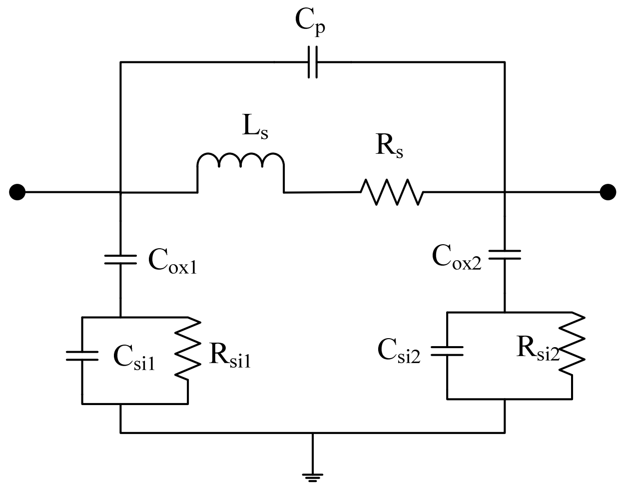

Figure 5-3: A simple two port π-model for integrated inductors.

and C_{si} models the capacitive effects of the substrate due to its semiconductor characteristics. Yue *et al.* developed expressions for the computation of each parameter in the model as a function of the geometric values of the inductor and the fabrication process parameters [91]. These expressions of various parameters of the π-model for integrated inductors as shown in Figure 5-3 are shown below:

$$R_s = \frac{\rho l}{w\delta\left(1 - e^{-t/\delta}\right)} \tag{5-06}$$

where w is the width and t the depth of the strip, 1 the length of the spiral, δ the skin depth at the considered frequency and ρ the resistivity of the metal. L_s is computed using Greenhouse formula (5-01).

$$C_p = \frac{nw^2\epsilon_{ox}}{t_{oxM1-M2}} \tag{5-07}$$

where n is the number of crossings between the coil and the central lower connection, w is the width of the strips, ε_{ox} is the oxide dielectric constant, $t_{oxM1\text{-}M2}$ is the oxide depth between the spiral tracks and its central interconnection.

$$C_{ox} = \frac{lw\epsilon_{ox}}{2t_{ox}} \tag{5-08}$$

$$C_{si} = \frac{lwC_{sub}}{2} \tag{5-09}$$

$$R_{si} = \frac{2}{lwG_{sub}} \tag{5-10}$$

where C_{sub} and G_{sub} are the substrate capacitance and conductance per unit area, respectively. These two constants are empirically computed.

5.3 Methods for Improvement of On-Chip Inductors

Various methods have been proposed in literature to improve the overall inductance and the quality factor of the integrated inductors. Some of the methods are discussed below:

1. Patterned ground shield (PGS): Yue *et al.* proposed this method in 1998 [92]. Poly silicon layer is used as the ground shield to reduce the loss due to conductive substrate. In this method the inductance remains almost same, the capacitance increases, the Q increases while the SRF decreases.

2. High resistivity silicon substrate: Ashby [93] reported high resistivity silicon substrate (150-200 Ω-cm) to lower the substrate loss.

3. Etching of silicon substrate: By selectively removing the underlying silicon substrate using a bulk micromachining technique the substrate loss can be eliminated [94-96].

4. Insertion of additional layer: By inserting additional layer between substrate and inductor (metal layers) the substrate loss can be reduced [97, 98].

5. Use of thick dielectric layer: By using thick dielectric layer between the substrate and the metal layers one can substantially reduce the substrate coupling [99].

6. Thick conductor lines: Thicker conductors have been used to reduce the resistance of the inductor and it also reduces electromigration effect [98, 100, 101].

7. Differentially excited symmetric conductor: Danesh *et al.* proposed the technique of exciting the symmetric conductor differentially and thus increasing the quality factor of the inductor [102].

8. Multilevel conductor: Multi-level conductor is also reported in literatures to effectively increase the overall inductance of the inductor [97, 103, 104].

9. Micromachining technique: A micromachined structure with reduced parasitics and fabricated on high resistivity silicon substrate is used to enhance the resonant frequency and the quality factor (Q) of a spiral inductor [105].

10. Layout optimization: Lopez-Villegas *et al.* proposed a layout optimization technique which reduced the effect of series resistance of the coil and increased the quality factor of the inductor [106].

5.4 Design of On-Chip Inductors for Biomedical Applications

Designing of integrated inductors has been a great challenge due to parasitic effects, low inductance, and low quality factor. Due to process constraints the value of inductance of integrated inductor is generally below 20 nH and the value of Q ranges in 10~15 [85]. Due to this limited performance of the on-chip inductors it is not feasible to operate in the MHz range.

There are few reported works where on-chip inductors have been used for biotelemetry applications. O'Driscoll proposed a bond wire inductor based biotelemetry system where a 4 cm^2 PCB antenna was used as a transmitter and a 4 mm^2 bond wire inductor was used as a receiver with -32.2 dB gain for 25 mm distance in 1 GHz frequency [107]. Sawan *et al.* proposed a biotelemetry system where four integrated inductors were used to increase the overall efficiency of 18% using a custom fabrication process [44]. MEMS based inductors are also proposed for power transfer applications. Post-processing inductors are also discussed in literature.

Frequency of operation is another concern for designing integrated implantable systems. Due to smaller size of inductors the frequency needs to go higher, usually in the GHz region. Although regulation is stricter in this high frequency, low power operation of integrated circuits can make the system feasible. Based on the measurement data by Gabriel et al. [108] approximate optimal frequencies of different types of biological tissues have been calculated by O'Driscoll [109] and are given in Table 5-3. From the Table 5-3 it is evident that low GHz frequency is a viable option to transfer power

Table 5-3: Approximate Optimal Frequency for Different Types of Biological Tissues. Assuming Distance, d = 1 cm [109].

Type of Tissue	*Approximate optimum frequency (GHz)*
Blood	3.54
Bone (cancellous)	3.80
Bone (cortical)	4.50
Brain (grey matter)	3.85
Brain (white matter)	4.23
Fat (infiltrated)	6.00
Fat (not infiltrated)	8.64
Heart	3.75
Kidney	3.81
Lens Cortex	3.93
Liver	3.80
Lung	4.90
Muscle	3.93
Skin (dry)	4.44
Skin (wet)	4.01
Spleen	3.79
Tendon	3.17

through tissues. It opens up possibility of using integrated inductors for power transfer applications. O'Driscoll showed that the optimal frequency for wireless power transmission is about 1 GHz for small coil size in a layered human tissue [107]. To the best of the author's knowledge there is no reported work on inductive power transfer by integrated on-chip inductors fabricated using a commercial process.

In this work, design and optimization of multi-spiral solenoidal integrated inductors for biotelemetry applications is proposed. Proposed inductors could be a path towards a complete integrated system. The inductors are simulated and optimized for targeted application using a commercial electromagnetic tool, Sonnet Software [76].

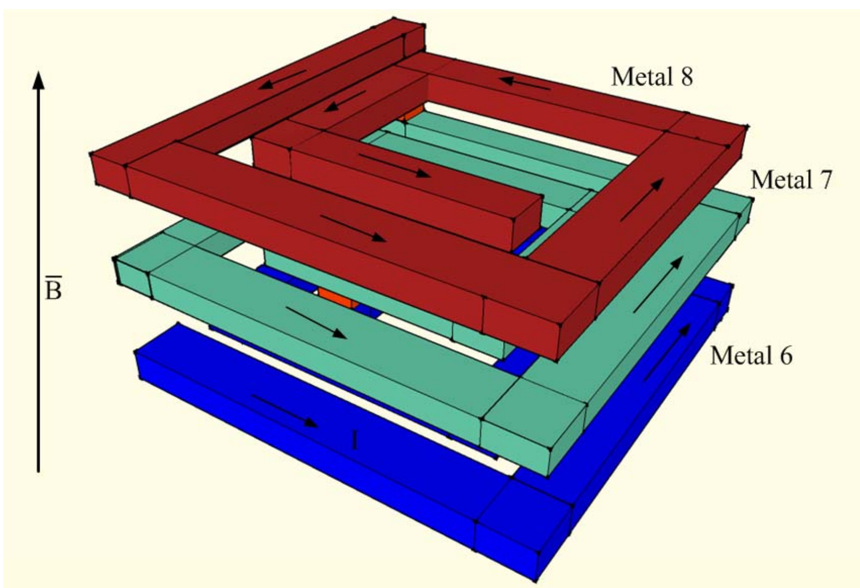

Figure 5-4: 3D view of a three-metal layer integrated inductor in a solenoidal structure. Arrows show the direction of the flow of current. (Not drawn to scale)

Inductance can be increased if the effective mutual coupling between metal lines functions as positive coupling. This concept has been applied for multi-spiral inductors. Multi-spiral inductors are designed in such a way that the net effect of mutual coupling of all the planar inductors is positive which leads to a higher value of the overall inductance. A 3D view of the designed inductor is shown in

Figure 5-4.

The inductors have been designed in a commercial 90 nm RF CMOS process technology. The cross section of the process which uses 8 metal layers is shown in Figure 5-5. The top three metal layers (Metal 6 – Metal 8) are thicker than other metal layers and can be used to realize the inductor. By following the design rules given in process design kit (PDK), the width of metal is kept at 7 μm, spacing between the metal layers is 3 μm, and the total size is 300 μm by 300 μm.

From equation (5-01) it is evident that inductance can be increased if the length of the metal trace is increased and if the effective mutual coupling between the metal lines functions as positive coupling. This concept is utilized and expanded to design the multi-spiral solenoidal inductors. Flowing of current in the designed inductor is shown in Figure 5-4. Multi-level conductors are stacked and designed to form a solenoidal structure. It is clear from equation (4-04) that if the magnetic flux density of a solenoid is increased it will increase the overall inductance. By having a solenoidal structure the magnetic flux inside the loop increases giving rise to the overall inductance of the structure. Simulated current distribution of the top layer of the inductor at 1 MHz and 990

MHz are shown in Figure 5-7 and Figure 5-6 respectively. Current crowding effect is dominant at higher frequencies and can be seen from Figure 5-6.

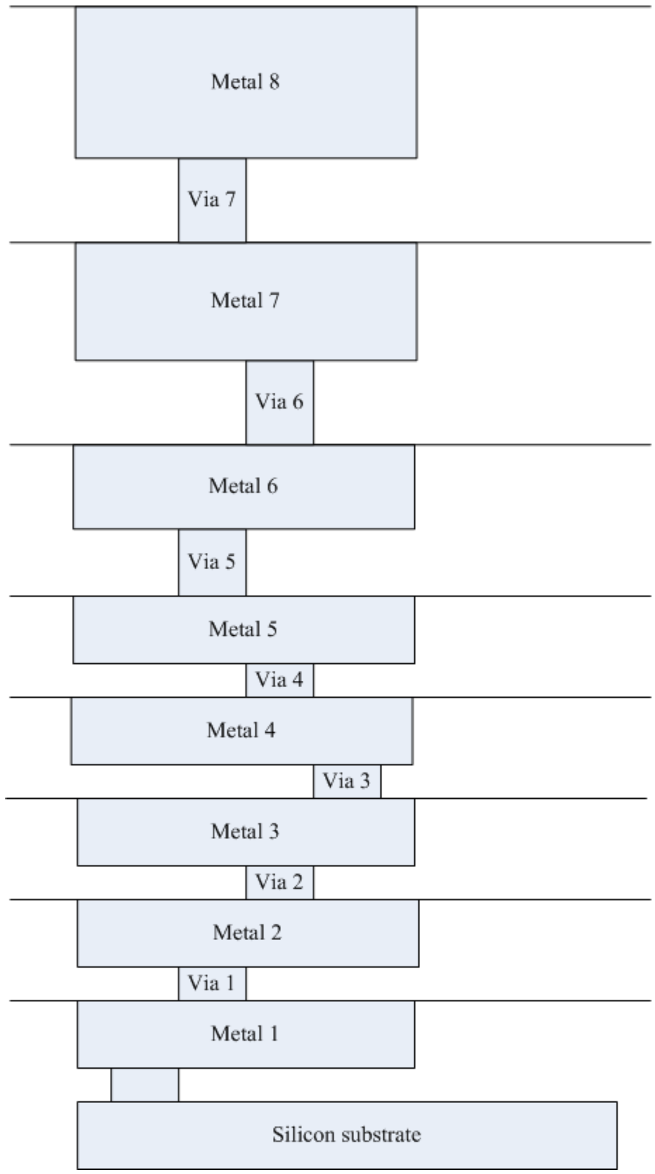

Figure 5-5: Cross section of back end of line (BEOL) metal layers of a commercial 90 nm RF CMOS process (not drawn to scale).

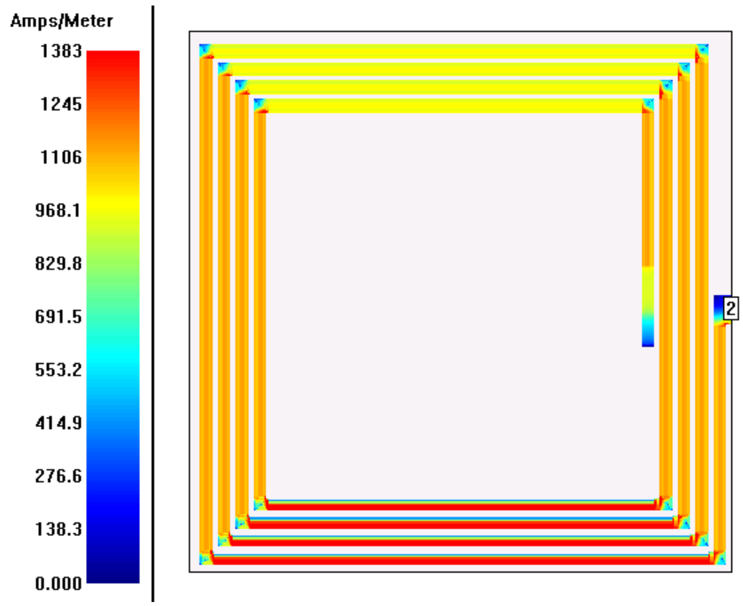

Figure 5-6: Current distribution of the top layer of the inductor at 1 MHz frequency.

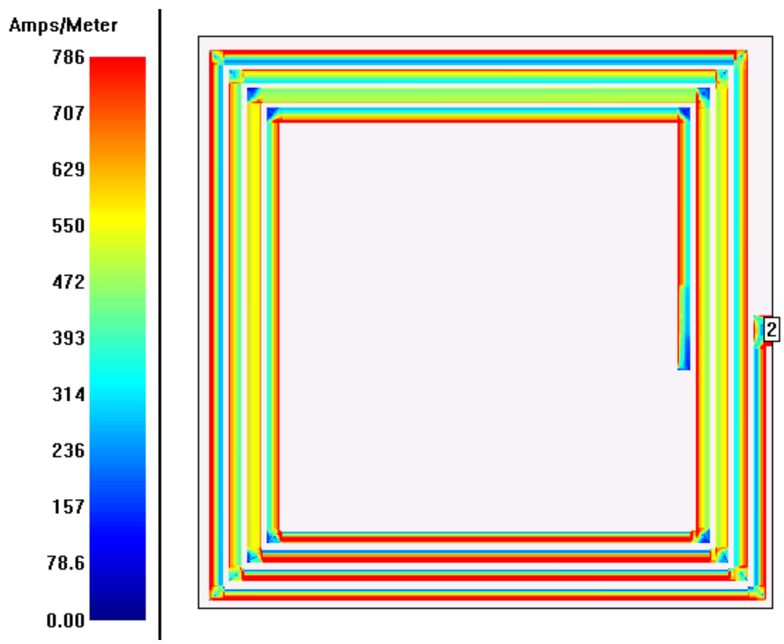

Figure 5-7: Current distribution of the top layer of the inductor at 990 MHz frequency.
Current crowding is obvious in this frequency range.

5.5 Mathematical Model of Multi-layer On-Chip Inductor

For multi-layer inductor the effective inductance will increase according to the number of turns in each layer and mutual coupling between the layers. For a two-layer stacked inductor the total inductance can be written as,

$$L = L_1 + L_2 \pm 2M_{12} \tag{5-11}$$

where, L_1 and L_2 are the inductance of layer 1 and layer 2, respectively and M_{12} is the mutual inductance between layer 1 and layer 2. Mutual inductance, M_{12} can be given as,

$$M_{12} = k_{12}\sqrt{L_1 L_2} \tag{5-12}$$

where, k_{12} is the mutual coupling between metal stacks 1 and 2.

Total inductance of two layer inductor becomes,

$$L_{2\_total} = L_1 + L_2 \pm 2k_{12}\sqrt{L_1 L_2} \tag{5-13}$$

For additive mutual coupling action of the structure the net inductance becomes,

$$L_{2\_total} = L_1 + L_2 + 2k_{12}\sqrt{L_1 L_2} \tag{5-14}$$

Similarly for three-layer stacked inductor total inductance can be calculated as,

$$L_{3\_total} = L_1 + L_2 + L_3 \pm 2M_{12} \pm 2M_{23} \pm 2M_{13} \tag{5-15}$$

Now,

$$M_{23} = k_{23}\sqrt{L_1 L_3}$$

$$M_{13} = k_{13}\sqrt{L_1 L_3}$$

Therefore equation (5-15) becomes,

$$L_{3\_total} = L_1 + L_2 + L_3 \pm 2k_{12}\sqrt{L_1 L_2} \pm 2k_{23}\sqrt{L_1 L_3} \pm 2k_{13}\sqrt{L_1 L_3} \tag{5-16}$$

For additive mutual coupling action of the structure the net inductance becomes,

$$L_{3\_total} = L_1 + L_2 + L_3 + 2k_{12}\sqrt{L_1L_2} + 2k_{23}\sqrt{L_1L_3} + 2k_{13}\sqrt{L_1L_3} \quad (5\text{-}17)$$

For i-layer stacked inductor total inductance is given by,

$$L_{i_{total}} = \sum_{j=1}^{i} L_j + \sum_{\substack{j=1 \\ k=2}}^{\substack{j=i-1 \\ k=i}} 2.\,k_{jk}\sqrt{L_jL_k}, \quad where\ j \neq k \quad (5\text{-}18)$$

Series resistance can be calculated as,

$$R_{s-ilayer} = i\frac{\rho l}{w\delta\left(1-e^{-t/\delta}\right)} \quad (5\text{-}19)$$

Final set of equations for the equivalent π-model of i-layer stacked on-chip inductor are summarized in Table 5-4.

Table 5-4: Final Set of Equations for the Equivalent Pi-Model of i-Layer Stacked On-Chip Inductor

Parameter	**Equation**
Inductance	$L_{i_{total}} = \sum_{j=1}^{i} L_j + \sum_{\substack{j=1 \\ k=2}}^{\substack{j=i-1 \\ k=i}} 2k_{jk}\sqrt{L_jL_k},$ $where\ j \neq k$
Series Resistance	$R_{s-ilayer} = i\frac{\rho l}{w\delta\left(1-e^{-t/\delta}\right)}$
Self-Resonance Frequency	$f_{SRF} = \frac{1}{2\pi\sqrt{L_{eq}C_{eq}}}$

5.6 **Variation of Design Parameters**

Two design parameters are considered in designing on-chip inductors: a) number of metal layers and b) number of turns. Other two design variables (metal width and metal spacing) considered in design of PCB inductor are kept constant due to availability of limited space in the fabrication process. Lowest possible values of these two parameters available from the design process are assumed to obtain high inductance values. Effects of variation of number of metal layers and number of turns on inductor are discussed in the following sections.

5.6.1 Number of metal layers (l)

Inductors have been designed for number of metal layers (*l*) varying from 1 to 3. Figure 5-8(a) and (b) show the effect of variation of metal layer on inductance for frequencies up to 1.2 GHz. From the figures it is evident that with the increase in metal layers, the inductance increases. The trend also satisfies equation (5-18). Figure 5-9(a) and (b) show the effect of variation metal layer on the quality factor for frequencies up to 2 GHz. From the figures it is evident that with the increase in number of layer, the self-resonant frequency (SRF) decreases. The increase in number of layers leads to increase in the equivalent inductance and the capacitance which in turn reduce the SRF. *Layer 1 (Metal 8)* and *layer 2 (Metal 7)* are wide metals. But *layer 3 (Metal 6)* consists of thinner metal layer which has higher resistance. For this reason *Q* of *layer 3* is less than that of the *layer 2*.

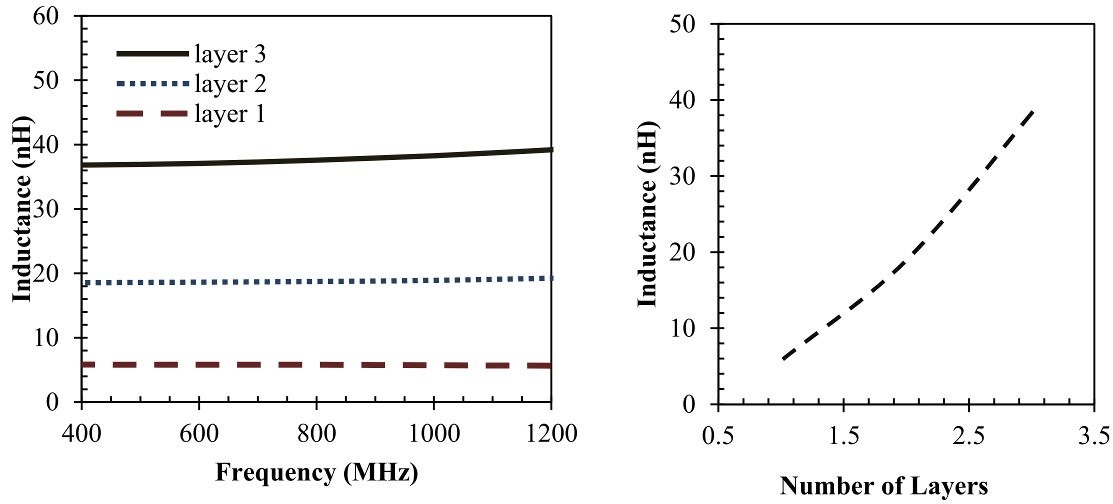

(a) (b)

Figure 5-8: (a) Effect of the variation of the number of metal layers on inductance of on-chip inductor with change in frequency. (b) Change of inductance at 1 GHz for changing metal layers. In this figure, number of turns is fixed to 4.

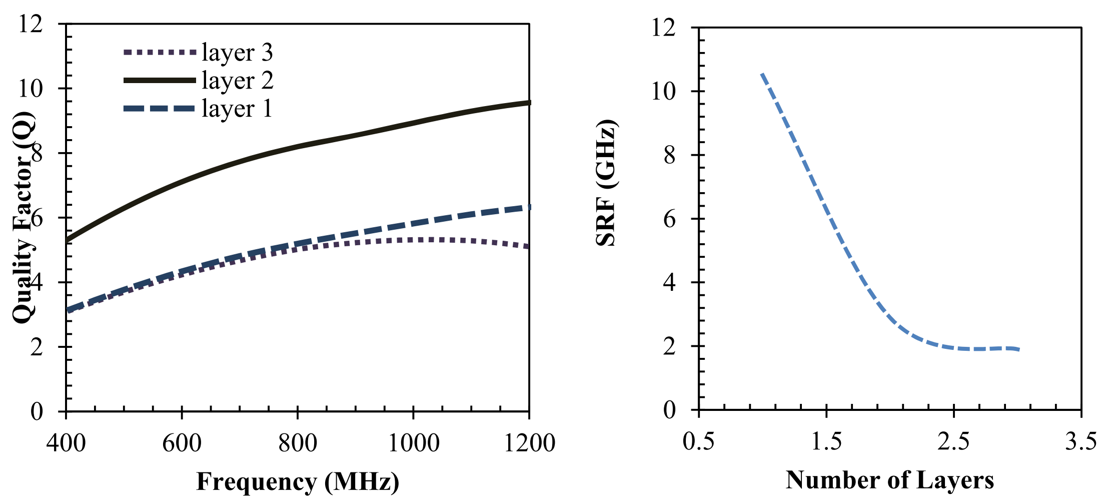

(a) (b)

Figure 5-9: (a) Effect of the variation of the metal layer on quality factor (Q). (b) Effect of the variation of the metal layer on self-resonance frequency (SRF). SRF values are obtained from (a). Here, number of turns is fixed at 4.

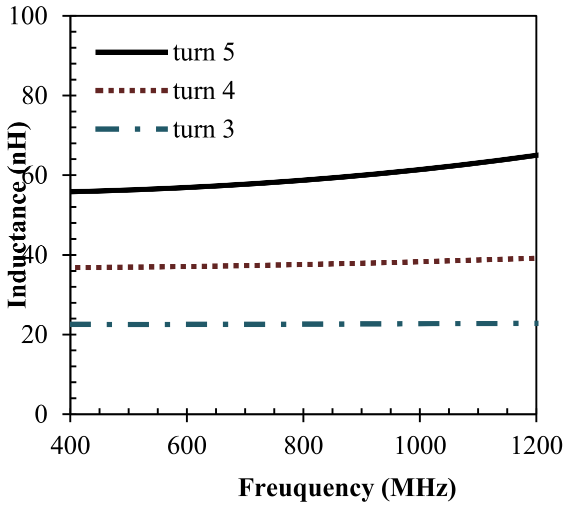

(a)

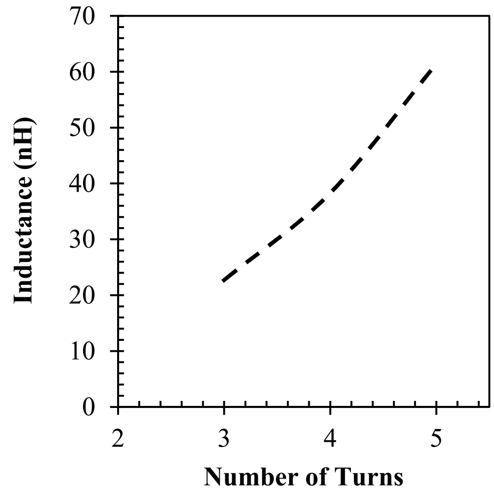

(b)

Figure 5-10: (a) Effect of the variation of number of turns on inductance of on-chip inductor with change in frequency. (b) Change of inductance at 1 GHz for changing the number of turns. In this figure, the number of metal layer is kept at 3.

5.6.2 Number of turns (n)

The number of turns (n) of the inductor is also varied for frequencies up to 1.2 GHz and the results are shown in Figure 5-10 (a) and (b). From the figures it is evident that as number of turns increases the inductance increases. The trend also satisfies equation (5-01). Figure 5-11 (a) and (b) show the variation of quality factor (Q) for varying the number of turns (n) of the inductor for frequencies up to 1.2 GHz. From the figures it is clear that as n increases the SRF decreases and the value of Q remains fairly similar for 1 GHz frequency range.

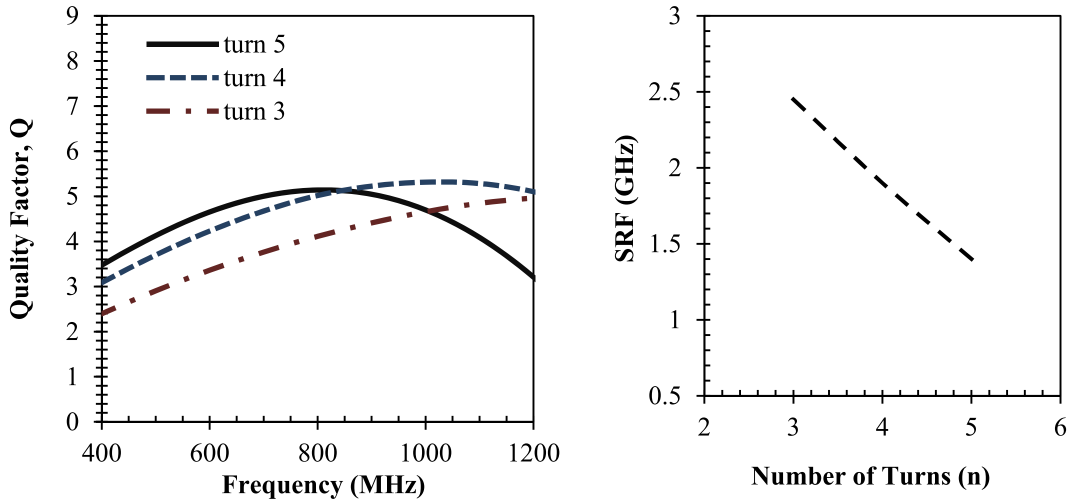

(a) (b)

Figure 5-11: (a) Effect of the variation of number of turn on quality factor (Q). (b) Effect of the variation of number of turn on self-resonance frequency (SRF). SRF values are obtained from (a). Number of metal layer is kept at 3.

5.7 Design Optimization

On-chip inductor is optimized for 1 GHz frequency. The target was to achieve the highest possible inductance and the quality factor at 1 GHz. In this case, value of L and Q in 1 GHz are optimized in the operating frequency range. The new $\mathrm{FOM}_{1\mathrm{GHz}}$ is defined as,

$$FOM_{1GHz} = \frac{L_{1\,GHz}\,(nH)Q_{1\,GHz}}{Area\,(mm^2)} \tag{5-20}$$

The target of the optimization is to get the maximum possible $\mathrm{FOM}_{1\mathrm{GHz}}$ from the given design constraints. The effect of the variation of the number of turns and the number of metal layers with respect to $\mathrm{FOM}_{1\mathrm{GHz}}$ is given in Table 5-5 and is plotted in Figure 5-12.

Table 5-5: The Effect of Variation of Number of Turns and Number of Metal Layers with Respect to FOM_{1GHz}

Inductor #	*Layer*	*Turn*	L_{1GHz} *(nH)*	Q_{1GHz}	FOM_{1GHz}
1	1 (Metal 8)	2	2.097	4.06	94.69
2	1 (Metal 8)	3	3.77	5.00	209.44
3	1 (Metal 8)	4	5.73	5.82	370.21
4	1 (Metal 8)	5	8.15	6.66	603.10
5	2(Metal 7)	2	6.04	5.67	380.86
6	2(Metal 7)	3	11.71	7.69	1000.98
7	2(Metal 7)	4	18.91	8.10	1701.37
8	2(Metal 7)	5	29.31	8.56	2787.71
9	3(Metal 6)	2	11.02	3.70	453.04
10	3(Metal 6)	3	22.71	4.66	1175.43
11	3(Metal 6)	4	38.27	5.31	2259.92
12	3(Metal 6)	5	55.41	4.70	3204.98

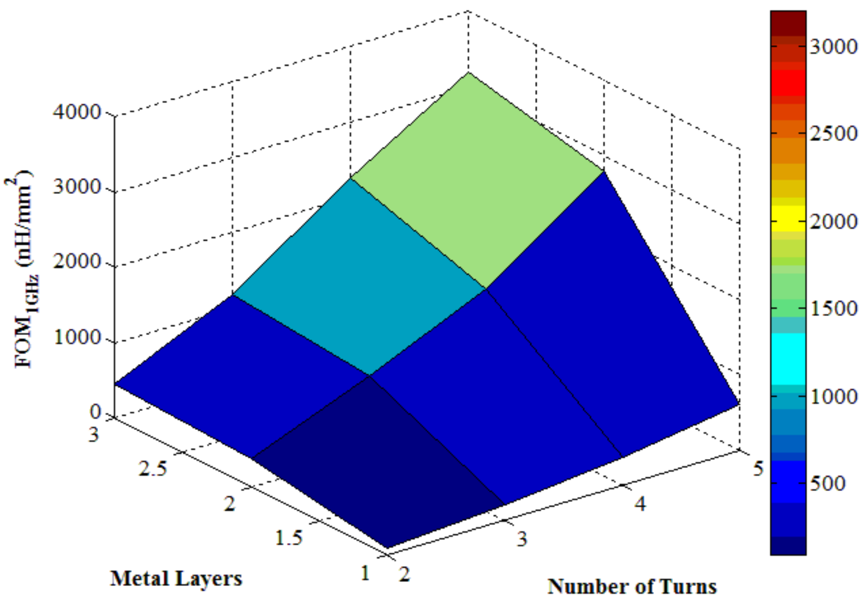

Figure 5-12: Optimization of the on-chip inductor with respect to number of turns and number of metal layers. Higher FOM is obtained for higher number of turns and higher number of metal layers.

It can be seen that higher metal spacing and higher metal layer number can lead to higher FOM_{1GHz}. From Table 5-5 it can be seen that, by combining *layer 1 (Metal 8)* and *layer 2 (Metal 7)* higher values of Q can be obtained. Inductor number 8 shows the highest value of Q. But *layer 3 (Metal 6)* is thinner than other two layers; hence it has higher resistance value. Therefore when layer 3 *(Metal 6)* is added to the structure the value of Q decreases. From Table 5-5 it can be seen that inductor number 12 shows the highest FOM_{1GHz}. But it has SRF of 1.44 GHz. As is it close to the operating frequency the next inductor (inductor # 11) is chosen as the optimized design. Specifications of the designed inductor (# 11) for 1 GHz frequency are summarized in Table 5-6.

Table 5-6: Design Summary of On-Chip Inductors at 1 GHz Frequency

Parameter	***Value***
Size	300 µm X 300 µm
Process	90 nm RF CMOS
Number of turn	4
Metal spacing	3 µm
Metal width	7 µm
Number of layer	3
Self-resonant frequency	1.9 GHz
Inductance, L (1 GHz)	38.2756 nH
Quality factor, Q (1 GHz)	5.3

5.8 Layout of the Inductor

Inductors are designed and fabricated in a commercial 90 nm RF CMOS process. Ground-signal-ground (GSG) probe pads are utilized for probing and measurement. GSG structure works as a coplanar wave guide which isolates the signal path from noise and interferences. Generally GSG pads provide good shielding, reduce the ground-lead inductance to device under test and can produce cleaner microwave signals. GSG pads are designed with a 150 µm pitch. Two sets of GSG pads are placed in opposite directions for proper probing. All the ground pads are connected together and are shorted to the substrate of the die using substrate tie down. Microphotograph of the designed inductor with GSG pads is shown in Figure 5-13. Metal fills have been used to meet the density requirement of the fabrication process.

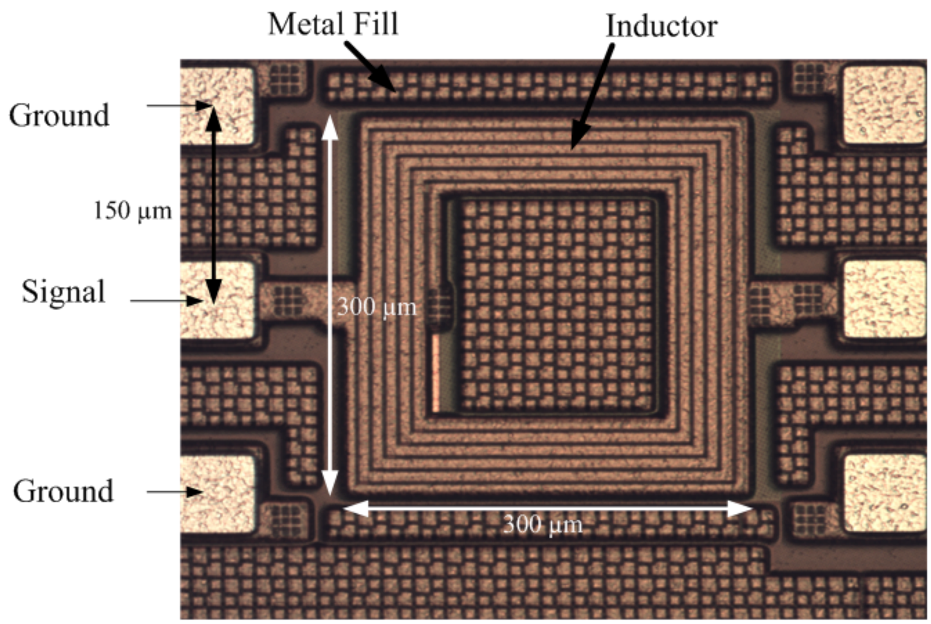

Figure 5-13: Microphotograph of the designed inductor in a 90 nm RF CMOS process. Size of inductor is 300 µm by 300 µm and pitch of the GSG pad is 150 µm.

5.8.1 On-Wafer Calibration Structures

There is a need to calibrate the on-wafer measurements for proper extraction of the parameters of device under test (DUT). Generally, on-wafer measurements are calibrated by using a ceramic 'impedance standard substrate' (ISS) with high precision calibration standards. As long as the substrate containing the DUT has similar loss and coupling characteristics as the ISS, this type of calibration offers a calibrated reference plane close to the probe tips. But a stand-alone ISS calibration cannot represent high-loss silicon CMOS substrates. Currently the most reliable approach is to use a ceramic ISS in combination with calibration devices fabricated in the CMOS technology. By this approach, measurement pads and external interconnects may be included in the calibration and thereby de-embedded. Hence, the reference plane may be established close to the intrinsic boundary of the device as desired.

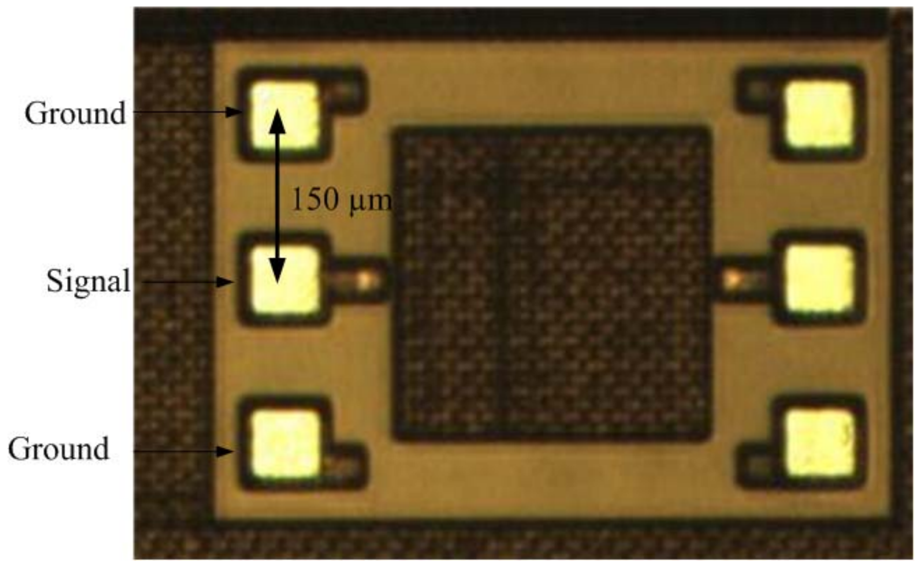

Figure 5-14: ‘Open’ test structure for on-wafer calibration. It is a complete structure without a device under test.

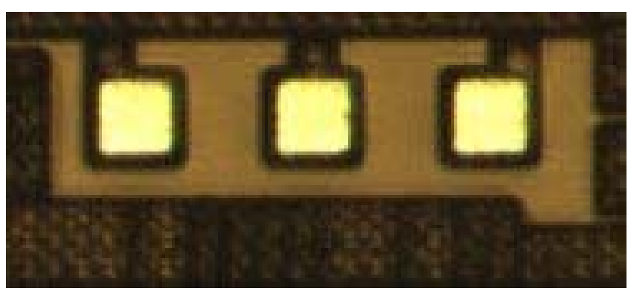

Figure 5-15: ‘Short’ test structure for on-wafer calibration. All the pads are shorted.

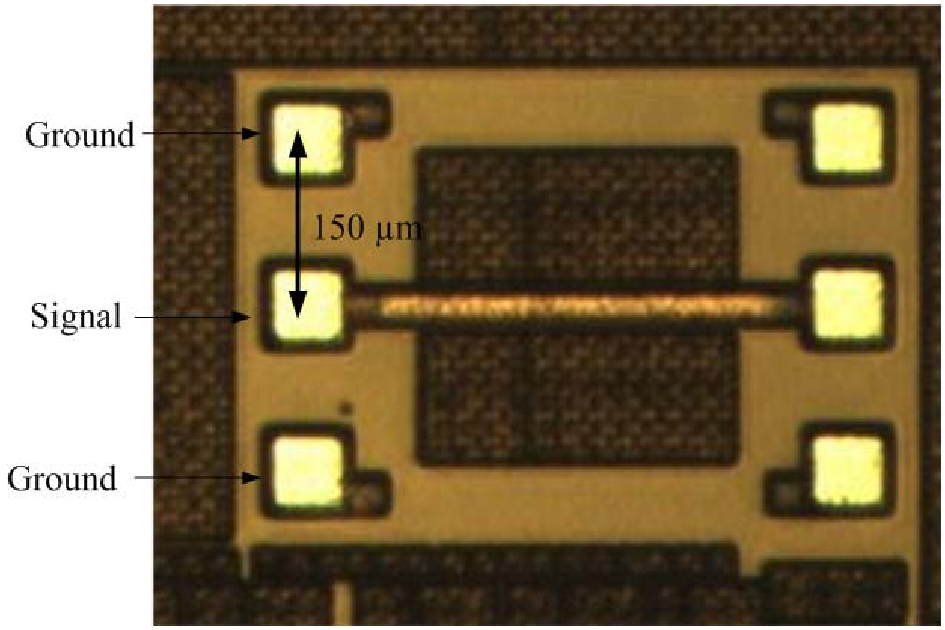

Figure 5-16: 'Through' test structure for on-wafer calibration. Signal pads of both GSG pads are shorted.

T. E. Kolding discusses in detail the test structures for proper calibration of DUT in GHz frequencies [110, 111]. By following Kolding's approach, three test structures are added to the design for open/short/through de-embedding (OSTD) method. Microphotograph of the test structures are shown in Figure 5-14, Figure 5-15, and Figure 5-16. Figure 5-14 shows the 'open' calibration structure where a complete structure without a DUT is designed. 'Short' calibration structure is shown in Figure 5-15, where all the pads (GSG) are shorted. Figure 5-16 shows the 'through' calibration structure, where the signal pads of both GSG pads are shorted through a metal layer.

5.9 Extraction of π-Model and Comparison with Mathematical Model

5.9.1 π-Model

Spice parameters have been extracted from Sonnet simulation results. Sonnet gives a π-model of inductor for a given frequency. Simulations have been done for various numbers of metal layers. The parameters of the inductor are given in Table 5-7.

Table 5-7: Parameters of On-Chip Inductor

Parameter	***Value***
Outer diameter	300 μm
Inner diameter	208 μm
Number of turns	4
Coil width	7 μm
Coil spacing	3 μm
Metal layer	3 (Metal 8, Metal 7, Metal 6)

For this structure, parameters of the spice model are extracted as (see Figure 5-17 (a)), where, L_{M8} = 5.78 nH, $R_{s\text{-}M8}$ = 4.377Ω, C_{p1} = 0.048 pF, C_{p2}=0.07 pF. Similarly simulation has been performed for layer *Metal 7*. It is found that L_{M7} = 5.8 nH, and $R_{s\text{-}M7}$ = 5.4Ω. For layer M6, L_{M6} = 6 nH, and $R_{s\text{-}M6}$ = 16.85Ω. Therefore, the inductance value remains almost the same for a single layer structure at different metal layers. But the value of the series resistance changes as the thickness of the metal changes.

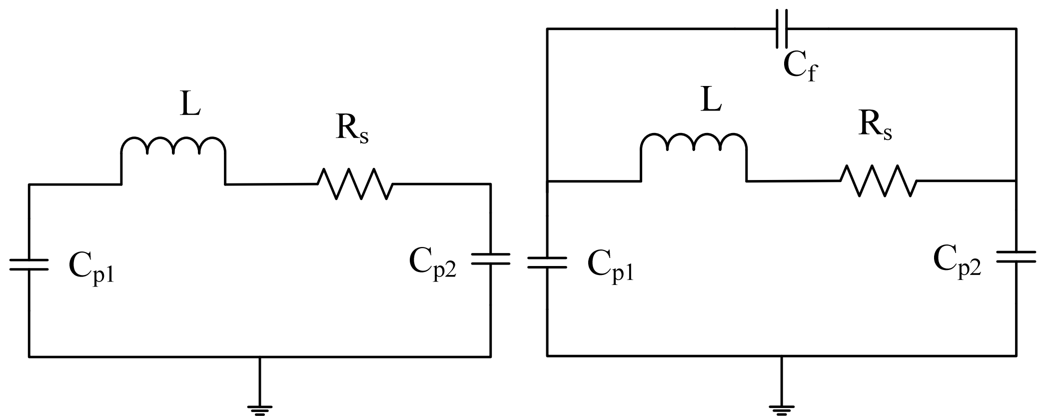

Figure 5-17: π-model for (a) a single layer (b) a two-layer on-chip inductor

Next, simulation is performed for a two layer (*Metal 8* and *Metal 7*) solenoidal spiral (see Figure 5-17 (b)). It is found that, L_{M78} = 18.55 nH, $R_{s\text{-}M78}$ = 9.96 Ω, C_{p1} = 0.06 pF, C_{p2} = 0.11 pF, and C_f = 0.03 pF.

Using equation (5-18), $L_{M78} = L_{M8} + L_{M7} + 2k_{78}\sqrt{L_{M8}L_{M7}}$

Solving the equation one can get, k_{78} = 0.6.

For a three-layer (*Metal 8-Metal 7-Metal 6*) inductor the parameters of the π-model are found to be,

L_{M678}=38 nH, $R_{s\text{-}M78}$=30.77 Ω, C_{p1}=0.163 pF, C_{p2}=0.1 pF, C_f=0.02 pF.

Using (5-18),

$$L_{M678} = L_{M8} + L_{M7} + L_{M6} + 2k_{78}\sqrt{L_{M8}L_{M7}} + 2k_{67}\sqrt{L_{M6}L_{M7}} + 2k_{68}\sqrt{L_{M6}L_{M8}}$$

Now, $L_{M8} \approx L_{M7} \approx L_{M6}$ and $k_{78} \approx k_{67}$

$$L_{M678} = 3\,L_{M8} + 4k_{78}L_{M8} + 2k_{68}L_{M8}$$

Solving the equation one can get, k_{68} = 0.58.

5.9.2 Mathematical Model of On-Chip Inductor

Mathematical model for on-chip inductor has been derived using the similar approach described in the previous chapter for PCB inductor. Using Greenhouse formula equation (4-07), the inductance and the resistance of a single layer (*Metal 8*) inductor can be calculated as, L_{M8} = 8 nH, $R_{s\text{-}M8}$ = 4.49 Ω. Similarly, the inductance value is over-estimated than the simulated value. But the series resistance value is almost the same as the simulated value.

Table 5-8: Comparison of Simulated and Calculated Inductance and Resistance values of On-Chip Inductor

Parameter	*Simulated*	*Calculated*
L_{M8}	5.78 nH	5.98 nH
$R_{s\text{-}M8}$	4.377 Ω	4.49 Ω
L_{M7}	5.8 nH	5.98 nH
$R_{s\text{-}M7}$	5.4 Ω	5.17 Ω
L_{M6}	6 nH	5.98 nH
$R_{s\text{-}M6}$	16.85 Ω	20.5 Ω
L_{M78}	18.55 nH	15.52 nH
$R_{s\text{-}M78}$	9.96 Ω	9.66 Ω
L_{M786}	38 nH	35.77 nH
$R_{s\text{-}M786}$	30.77 Ω	30.16 Ω

It has been found empirically that Greenhouse formula predicts approximately 26% higher than the simulated values. Greenhouse formula is modified as follows and a good match is achieved between the simulated and the calculated values:

$$L = 0.4699(\mu_0 n^2\, d_{avg})\left[ln\left(\frac{2.07}{\varphi}\right) + 0.18\varphi + 0.13\varphi^2\right] \tag{5-21}$$

Inductance and resistance values of all the metal layers have been calculated using the modified Greenhouse formula and these values are compared with simulated values in Table 5-8. Comparison results are also shown in Figure 5-18 and Figure 5-19. A good match is obtained between the simulated and the calculated values.

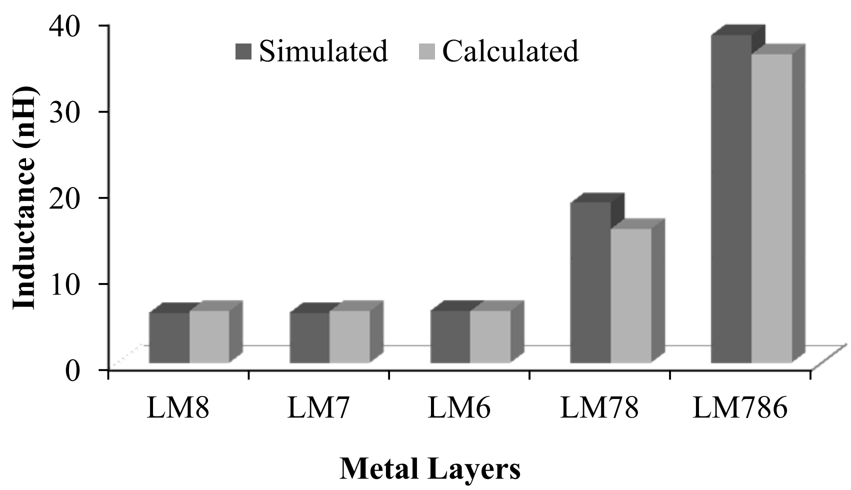

Figure 5-18: Comparison of the simulated and the calculated values of inductance for on-chip inductors. Simulation is performed by Sonnet software and calculation is done by modified Greenhouse formula.

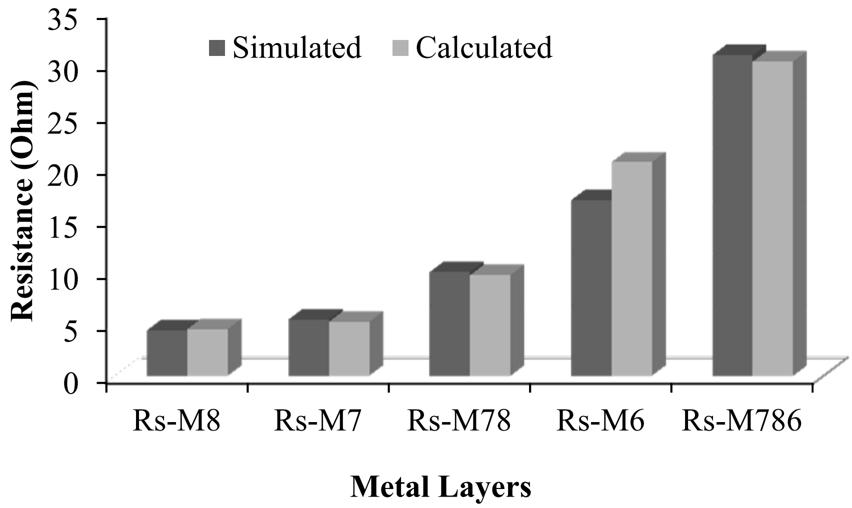

Figure 5-19: Comparison of the simulated and the calculated values of resistance for on-chip inductors. Simulation is performed by Sonnet software and calculation is done by modified Greenhouse formula.

5.10 **Measurement Results of On-Chip Inductors**

The inductors are fabricated using a 90 nm RF CMOS process. For the measurement the Agilent® E5071C ENA network analyzer has been used. A Signatone® probe station equipped with RF micro-positioners and Picoprobe® RF probes with 150 pitch have been employed for the measurements. The setup of the measurement is shown in Figure 5-20. S-parameters of the on-chip inductors are measured using network analyzer. By following the OSTD method the network analyzer is calibrated up to probe pad using on-chip calibration structures. Then the S-parameters of fabricated inductors are measured using the network analyzer from 0.9 GHz to 1.2 GHz. The experiments are carried out at room temperature and in normal environment without any RF shielding to emulate the real system where any inductive link is affected by ambient electromagnetic interferences. Microphotograph of the fabricated inductors is shown in Figure 5-21 and photograph of the on-chip inductor with RF probe is shown in Figure 5-22.

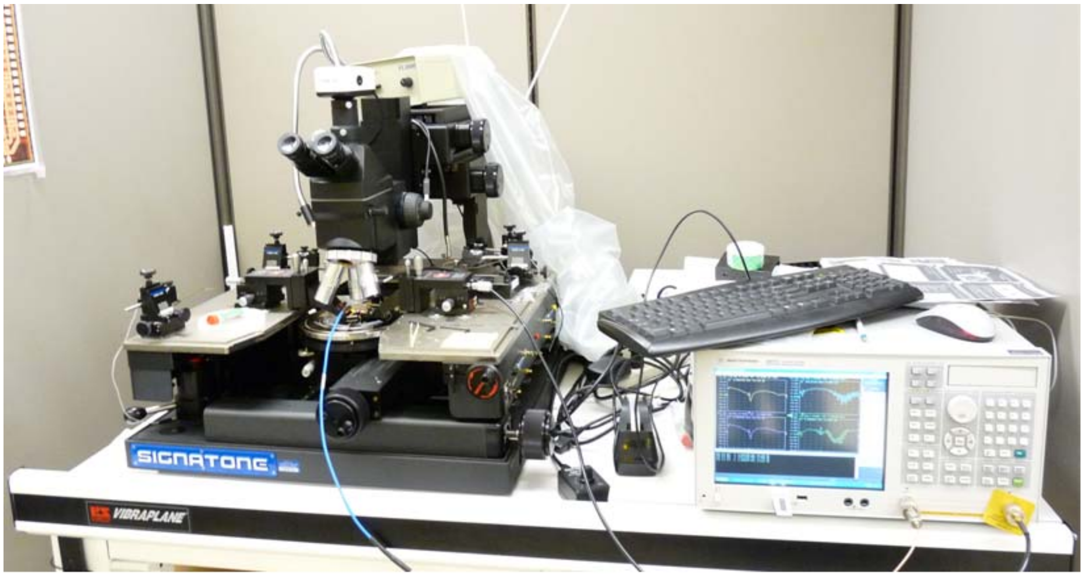

Probe Station   Network Analyzer

Figure 5-20: The test setup for measuring S-parameters of on-chip inductors. The setup comprises of probe station, network analyzer and vibration reduction table.

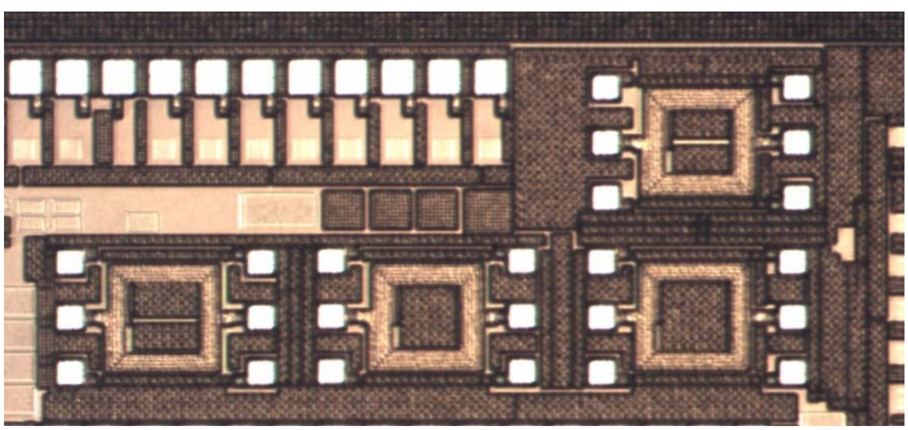

Figure 5-21: Microphotograph of the fabricated inductors.

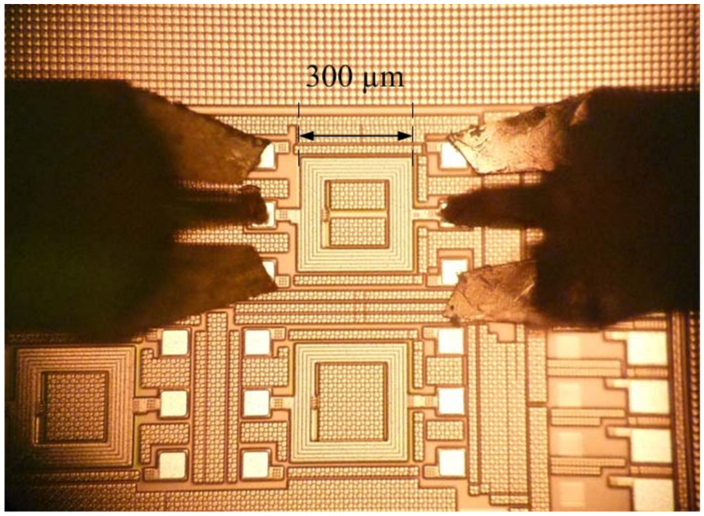

Figure 5-22: Probing of on-chip inductors using RF probes.

The measured S-parameters are converted to inductance values using a MATLAB® program. Two inductors of the same number of turns (# turns 4) and having two different number of layers (2 and 3) have been fabricated and measured. Inductance values from 900 MHz to 1.2 GHz are shown in Figure 5-23. It can be seen from the figure that higher number of layers can produce higher inductance. At higher frequencies parasitic effects have more impact on the overall reactance of the system.

For any inductor, three sets of measurements are taken from three different chips to identify the chip to chip variation. Figure 5-24 shows the inductance of the on-chip inductor (layer 3, number of turns 5) at frequencies from 900 MHz to 1.2 GHz for three different chips. Average standard deviation of the inductance is 3.3 nH which is low. This variation of inductance will change the resonance frequency as well as the power extracted from the inductive link system. This variation could be taken care of by a properly designed voltage regulator after the rectifier in the power receiver chain.

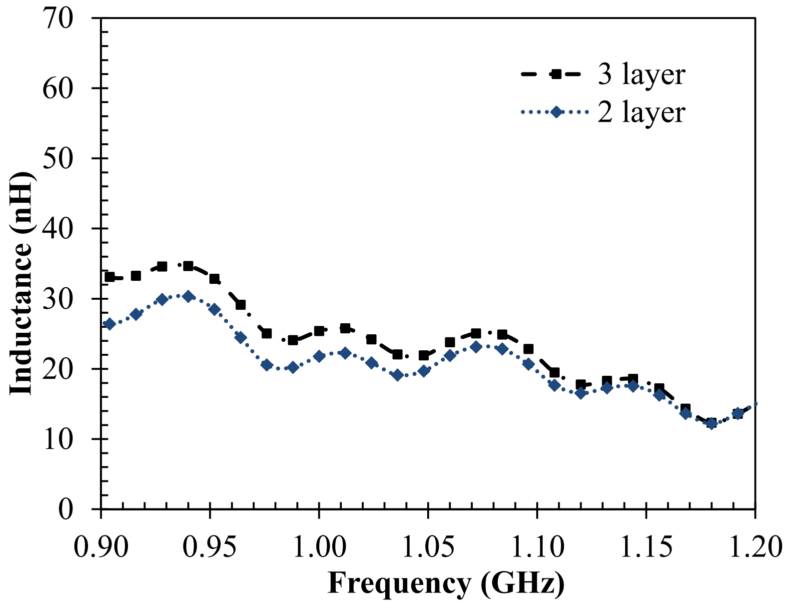

Figure 5-23: Measured inductance values of on-chip inductors with two different layers. Here, number of turns is 4.

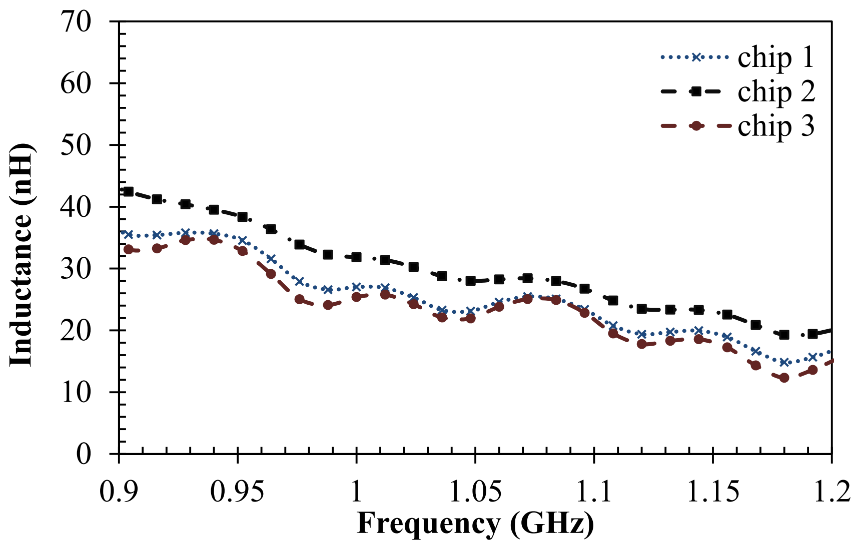

Figure 5-24: Measured inductance of on-chip inductors for three different chips. Here, number of layers is 3 and number of turns is 4.

5.11 **Comparison**

5.11.1 Comparison between simulated and measured data

For the three-layer inductor the simulated value of the inductance is 38 nH while the measured value is 31 nH. The measured and the simulated values of the inductance are very close to each other. The differences between the simulated and the measured values can be attributed to various non-ideal effects in high frequency systems which are discussed below.

First of all, for the purpose of simulation all the electric and magnetic properties of the inductor are assumed to be ideal. As the real electric and magnetic parameters (conductivity, relative permittivity, dielectric conductivity, etc) of oxide and metal layers are unavailable from the vendor, standard values of these parameters are considered. SiO_2 is considered as a standard dielectric layer between the metal layers. Copper (Cu) is considered as the metal layer from layer 1 to 7 and Aluminum (Al) is considered as the top layer (layer 8). In each simulation, only one inductor structure is simulated without having any other structures present in the system. In a real die, the measured inductor is in close proximity to other inductors, circuits and metal fills. Although, sufficient amount of substrate contacts have been employed to isolate the inductor from substrate noise but the noise from substrate will greatly affect the parameters of the designed inductor. Presence of metals in the core due to metal fills will increase the loss at high frequencies. This will eventually decrease the inductance. Due to presence of other metal layers (metal fills, circuits, inductors) in the vicinity of the designed inductor, it will have proximity effect. At high frequencies, proximity effect in conjunction with skin effect will change the current distribution of the inductor.

Non-idealities can come from the measurement as well. Errors can come from the calibration, reference plane, electromagnetic interferences, etc. These variations can be avoided by using good calibration kit, proper grounding and using anechoic chamber respectively.

5.11.2 Comparison with State of the Art Works

Table 5-9: Comparison of on-chip inductors reported in literature

Design	*Process*	*Inductance, L (nH)*	*Quality Factor*	*Area,A (mm^2)*	*FOM_{1GHz}*
Proposed design - on chip [simulated]	90 nm	38.27	5.3	0.0900	2254.01
Golmakani et al. [simulated] [112]	180 nm	15.09	3.44	0.0266	1951.45
Chih-Ming et al. [78]	Thin film	8.35	27.7	0.2750	841.07
Haobijam et al. [113]	180 nm	21.4	4	0.0625	1369.60
Wen-Yan et al. [114]	180 nm	8	0.7	0.0028	2031.74
Burghartz et al. [103]	0.8 µm	9	9.5	0.0511	1673.98

To the best of the author's knowledge, there is no reported work on wireless power transfer with integrated inductors in 1 GHz frequency using a commercial process yet. Therefore, the designed on-chip inductor is compared with multilevel inductors reported in literature in Table 5-9. It can be seen from this table that the proposed design shows the highest inductance as well as the highest FOM_{1GHz} compared to the reported works in the literature.

5.12 **Conclusion**

In this chapter, design of multi-spiral on-chip inductor for biomedical applications has been presented. The challenges of designing high *L*, and high *Q* on-chip inductors have been addressed and various methods to solve the problems have been discussed. The method discussed in chapter 4 is applied to design multi-spiral on-chip inductors. Method of moment based electromagnetic simulation has been done by Sonnet software. On-chip inductors along with on-wafer calibration structures have been designed and fabricated in a 90 nm commercial RF CMOS process. A π-model for the multi-spiral on-chip inductor is also proposed based on the empirical formulae. Measurements of S-parameters of different inductors are carried out using a network analyzer. The simulated and the measured values of inductor show a very good match. Finally, the designed inductor is compare with multi-spiral inductors reported in literature. It can concluded that the multi-spiral solenoidal structure can be employed to increase inductance of on-chip inductors

Chapter 6

DESIGN OF INTEGRATED WIRELESS POWER AND DATA TRANSFER SYSTEM

6.1 Design of Power Oscillator Based Wireless Telemetry System

In this chapter, the design and simulation of an inductive power link and backward telemetry scheme using power oscillator is presented. The primary side of the inductive link is driven by a class-E power amplifier (PA) which has zero-voltage switching and high drain efficiency. However a class-E PA needs square pulse to drive the circuit which causes extra power loss and results in poor power-added-efficiency (PAE) which is defined as,

$$PAE = \left[\frac{[P_{OUT}]_{RF} - [P_{IN}]_{RF}}{[P_{IN}]_{DC}}\right] X\ 100\% \tag{6-1}$$

Where, $[P_{OUT}]_{RF}$ is the output RF power, $[P_{IN}]_{RF}$ is the input RF power, and $[P_{IN}]_{DC}$ is the power of the input DC signal.

In this work, a power oscillator (POSC) replaced the PA to avoid the loss in the driver circuit and to achieve higher PAE. On the secondary side of the inductive link system, a charge pump based rectifier rectifies and boosts up the recovered power signal and supplies the power to the implanted sensor electronics. The recovered power is then used to run a ring oscillator-based sensor readout circuit to generate data signal based on sensor current variation. The frequency of the data signal is proportional to the magnitude of the input sensor current. A load-shift-keying (LSK) modulation scheme is used to back-transmit the data to the external unit. Use of power oscillator and modified rectifier unit help achieve higher efficiency. The system has been designed using a commercial 90 nm RF CMOS process with off-chip inductors and capacitors. The link frequency has been selected to be between 5 to 10 MHz to reduce the coil dimension and at the same time satisfy FCC standards. A coupling coefficient of 0.45 has been used to simulate the loosely coupled link coils. The differential cross-coupled power-oscillator can double the output power and filter the harmonic signal. The functional block diagram of the proposed inductive power link and backward telemetry scheme is shown in Figure 6-1.

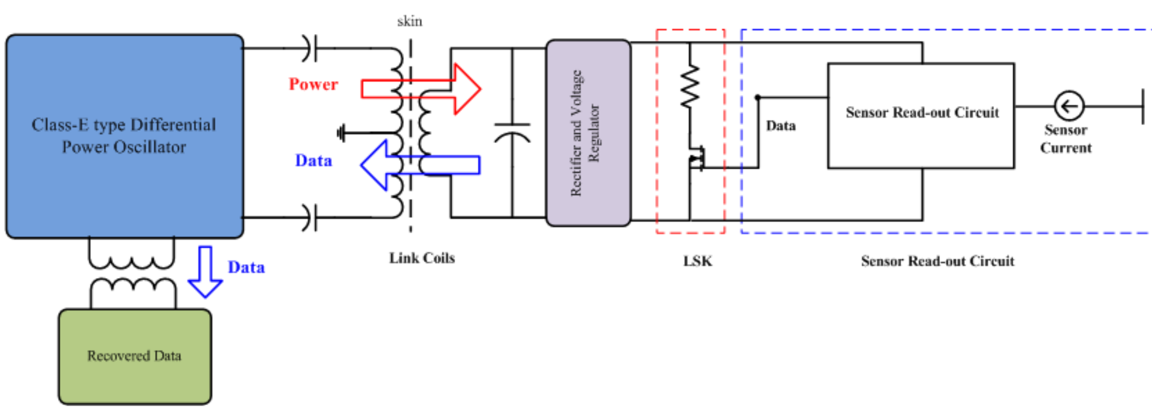

Figure 6-1: Block diagram of inductive power link and backward telemetry system.

The heart of the inductive power link system is a differential POSC that excites a resonant link coil at the primary side to inductively couple power to the secondary side. The recovered power is then rectified and regulated to make it usable for the sensor

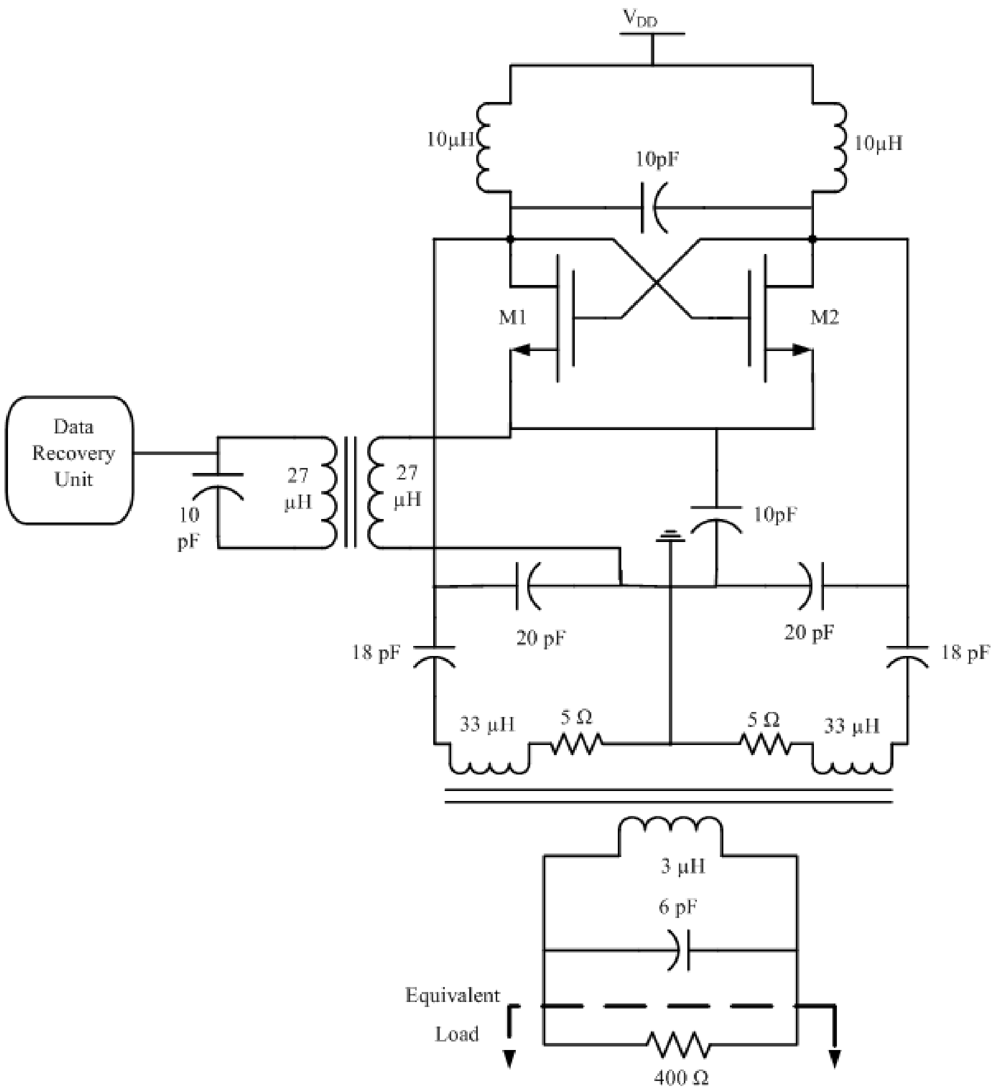

Figure 6-2: Differential class-E power oscillator and data recovery scheme.

readout block. Based on the amplitude of input current the sensor readout block generates the data signal. This data generated by the sensor readout circuit is then passed to a LSK modulator to back-transmit the sensor data using the same inductive power coils. The LSK data is reflected back to the primary side as a load variation which modulates the amplitude of the power signal of the differential POSC. The envelop of the power signal is then recovered via the data recovery block that represents the data signal of the sensor readout circuit back transmitted to the primary side. The detail descriptions of all the blocks are as follows.

6.1.1 Differential Power Oscillator

The basic block of an inductive power link system is the external power driving unit. In this design a cross-coupled MOSFET based differential POSC has been used (see Figure 6-2) to achieve higher PAE of the power link system. In this design a differential POSC is formed by combining the load network of a conventional class-E PA with the cross-coupled MOSFET structure. The series inductor of the load network also functions as a primary side link coil of the power link system. At the bottom of the cross-coupled structure, a LC tank resonating at twice the oscillation frequency is used to filter out the unwanted harmonics. Using half symmetry the frequency of oscillation of the differential POSC can be expressed as,

$$f_o = \frac{1}{2\pi\sqrt{L \cdot \left(C_P + C_f\right)}} \tag{6-2}$$

where L is the inductance and C_P and C_f are the individual drain terminal capacitance and the feedback capacitance between the differential outputs, respectively. The required transconductance of the MOSFET is defined by,

$$g_m = -\frac{R_P + R_L}{R_P \cdot R_L} \tag{6-3}$$

where, $R_P \approx Q^2 . R_S$, Q is the quality factor and R_S is the series resistance of the inductor, respectively. R_L represents the effective load resistance of the load network and the reflected resistance coming from the secondary side of the link coils.

6.1.2 Inductive Link Coils

An inductive power link consists of an external coil, L_{ext} and an internal coil, L_{int} as shown in Figure 6-3. For resonant operation, a series capacitor, C_S is used with the external coil and a parallel capacitor, C_P is used with the internal coil. Literature

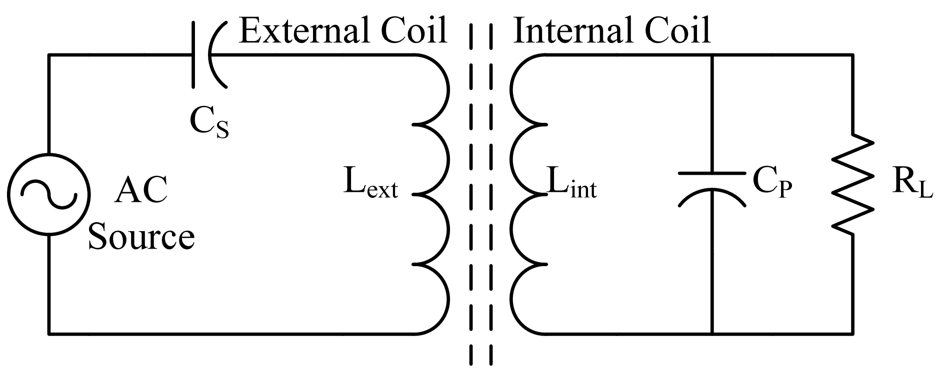

Figure 6-3: Inductive link coils

review shows that with series resonance the power transfer to the external coil from the source unit can be maximized whereas with parallel resonance the output voltage on the internal unit can be maximized [115]. An alternating signal is applied to the external coil which generates a magnetic flux. A portion of the generated magnetic flux is coupled to the internal coil and induces a voltage there. The induced voltage, V_R on the internal coil sources a current to the implanted electronics. Considering the implanted electronics as an equivalent load resistance of value R_L, the power delivered to the load can be expressed as,

$$P_L = \frac{V_{R,peak}^2}{2R_L} \tag{6-4}$$

Finally, if the power delivered from the source is considered as P_S, the link efficiency of the system is defined by,

$$\eta = \frac{P_L}{P_S} \tag{6-5}$$

6.1.3 Design of Rectifier

Generally a CMOS rectifier using diode connected MOSFETs have a loss across the diodes due to threshold voltage (V_{th}) of the MOSFETs. It becomes an issue if the supply voltage is low compared to the threshold voltage of the MOSFET. For example, a diode connected rectifier with V_{th} = 0.3 V would give an ideal output of 0.4 V for an input of 0.7 V. Consequently significant amount of energy is lost across the diodes. Therefore, in this design, a self synchronous rectifier is used. This rectifier is designed after the self synchronous rectifier described by Zhang *et al.* for power electronics application and later used by Mandal *et al.* for CMOS circuits [116, 117]. The basic cell or base cell of the rectifier is shown in Figure 6-4 (a). The operation of the circuit is as follows. The base cell comprises of for MOSFETs – two NMOS and two PMOS.

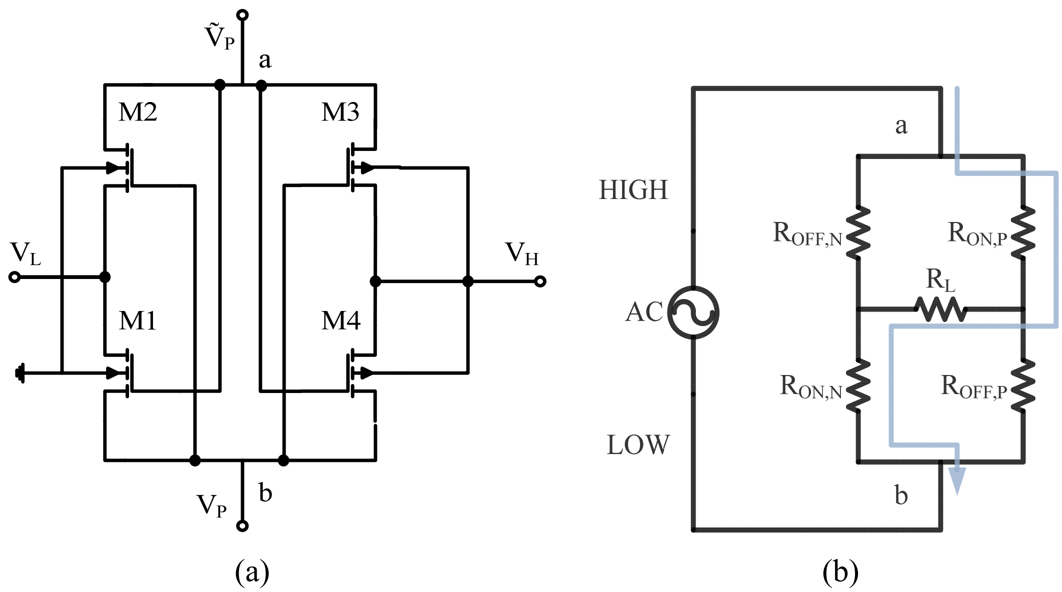

Figure 6-4: (a) Circuit schematic of the rectifier base cell (b) operation of the base cell.

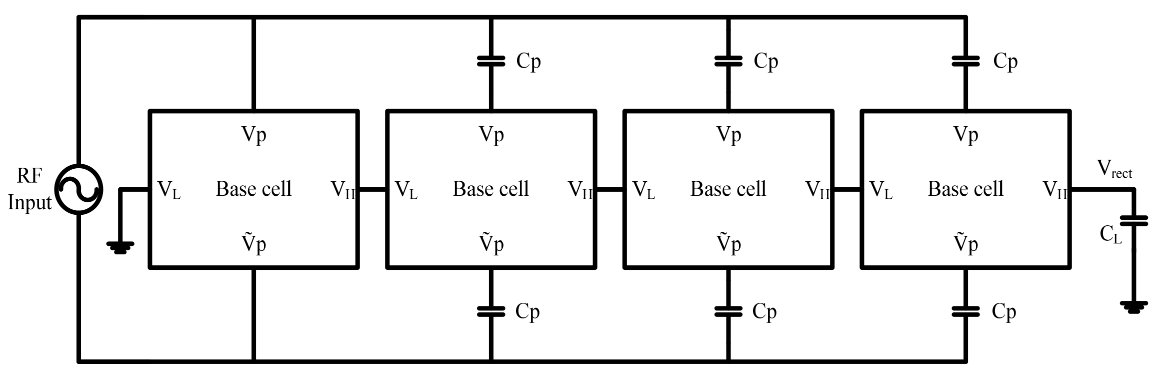

Figure 6-5: Schematic of the complete rectifier by cascading the base cell.

When the input is “high”, i.e. node ‘a’ is at higher potential than node ‘b’, M1 and M3 are ON and M2 and M4 are OFF. The applied potential may not be sufficient to drive the devices in saturation mode and the devices will operate in linear region and can be represented by voltage dependent resistors as illustrated in Figure 6-4 (b). The load resistor, R_L represents the load across output terminals. When $R_{OFF,N}$, $R_{OFF,P}$ >> R_L, current will flow through the path shown in Figure 6-4 (b) in each half cycle. The output of rectifier is, $V_{REC} = \frac{R_L}{R_L + R_{ON}} V_{IN}$ where, $R_{ON} = R_{ON,N} + R_{ON,P}$. This design would have lower loss than the typical diode connected rectifier if, $\frac{R_L}{R_L + R_{ON}} V_{IN} < V_{TH}$. Now, a DC voltage is generated across the output terminal of the rectifier. In general,

$$V_{REC} = V_H - V_L = 2V_{RF} - V_{drop} \tag{6-6}$$

When input amplitude is low, a single rectifier stage does not typically generate adequate DC output voltage. A number of rectifier stages can be cascaded in a charge pump-like topology to increase output DC voltage. The RF inputs are fed in parallel into each stage through pump capacitors (C_p = 100 fF) and the DC outputs are added in series to produce the final output V_{rect}. Schematic of the complete rectifier is shown in Figure 6-5. Parasitic bipolar transistors can lead to latch-up in MOSFET based rectifiers implemented in CMOS processes [118]. But the designed rectifier does not experience the latch-up problem. Since the operating frequencies are greater than the cut-off frequency of the parasitic devices, these rectifiers are free from latch-up. In addition, RF voltage and current amplitudes are comparatively small. Standard layout techniques have been used to further reduce the probability of latch-up. The NMOS and PMOS are physically separated and guard rings have been implemented.

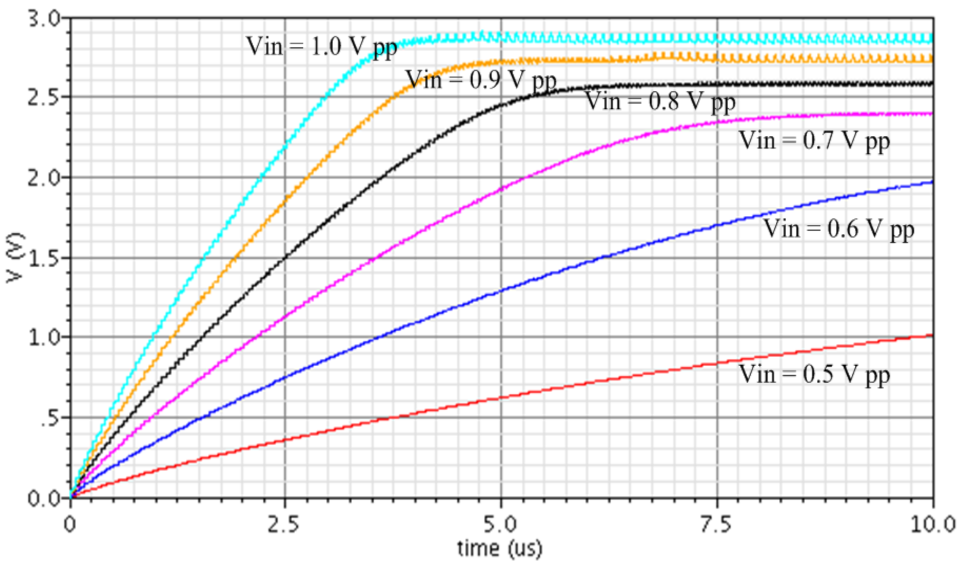

Figure 6-6: Transient simulation results of rectifier for various input voltages

Transient simulation result of the rectifier is shown in Figure 6-6 for different amplitude of input signal at 1 pF load. As the amplitude of the input signal increases, the rise time decreases and the amplitude of DC signal increases (see Figure 6-7). This rise time determines the response or delay time of the circuit. Since biomedical applications are targeted, delays in μs range are good enough to meet the specifications.

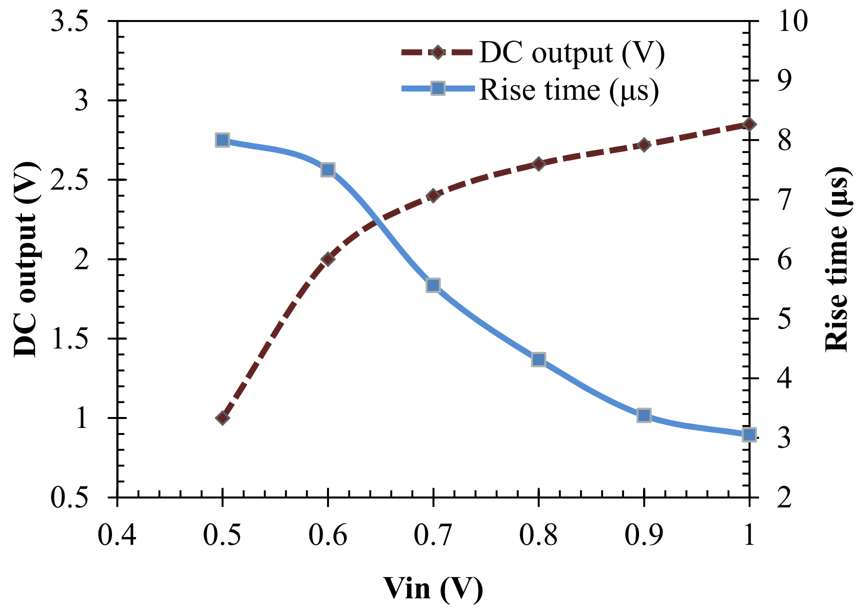

Figure 6-7: DC output voltage and rise time of the rectifier with respect to increase in input amplitude. Data of this figure are obtained from Figure 6-6.

6.1.4 Sensor Read-Out Circuit

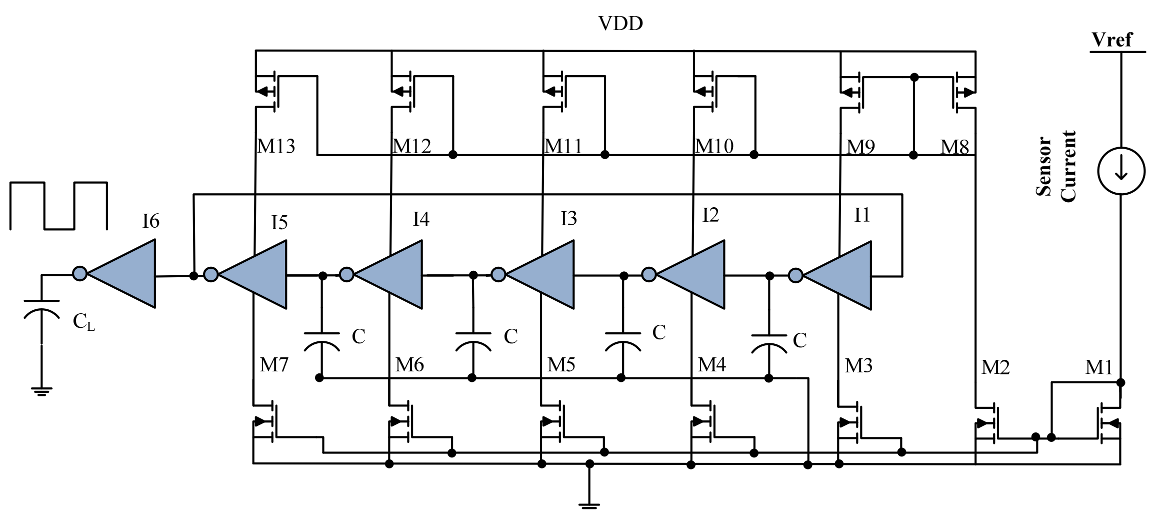

Figure 6-8: Sensor read-out circuit for data generation based on current starved ring oscillator. Frequency of output signal is proportional to the input sensor current.

The sensor read-out circuit or data generator is fundamentally a current starved 5-stage inverter based ring oscillator as shown in Figure 6-8. Inverter I1 to I5 work as the ring oscillator and I6 works as the output buffer. It is assumed that the targeted biomedical sensors will produce current output related to the physiological phenomena being measured. For example, a glucose sensor will produce the output current proportional to the amount of glucose it is measuring in blood and in any other environment. This current is designated as the 'sensor current'. This sensor current is fed to the input NMOS M1. From M1 this current is copied to the bottom bias network (M2 to M7) through the current mirror. The current is also used to bias the top PMOS bias network (M8 to M13) through the current sources. Both bias networks control the bias currents of the ring oscillator (I1-I5). In other words the inverters are starved of current. Thus this structure is known as the current starved oscillator. The frequency of oscillation of the ring oscillator is defined by [119]

$$f_{osc} = \frac{I_{sensor}}{2N \cdot V_{osc} C} \tag{6-7}$$

where, C is the capacitance of the individual stage, V_{osc} is the oscillation amplitude, I_{sensor} is the sensor current and N is the number of stages. As a result, the ring oscillator generates frequency modulated digital pulses where the frequency of pulses is directly proportional to the level of sensor current. For biomedical applications, it can be said that the frequency of the digital pulse is proportional to the measured physiological phenomenon. The ring oscillator is designed to operate in the input current range of 1 μA to 5 μA which is an acceptable range in some biomedical applications [120]. Data generator is designed to work with low power supply voltage. It can work very well at supply voltage of 500 mV although the nominal supply voltage is 1.2 V. Transient response of the data generator is illustrated in Figure 6-9 for 5 μA of input current. Pulse signal of 50% duty cycle is generated by the data generator. It can be observed from equation (6-7) that the frequency of the generated pulse is proportional to the input current. Data has been taken for the entire operating range of 1 μA to 5 μA for output frequency and the average power consumption are shown in Table 6-1 and Figure 6-10. As the input current is increased the data frequency is increased linearly.

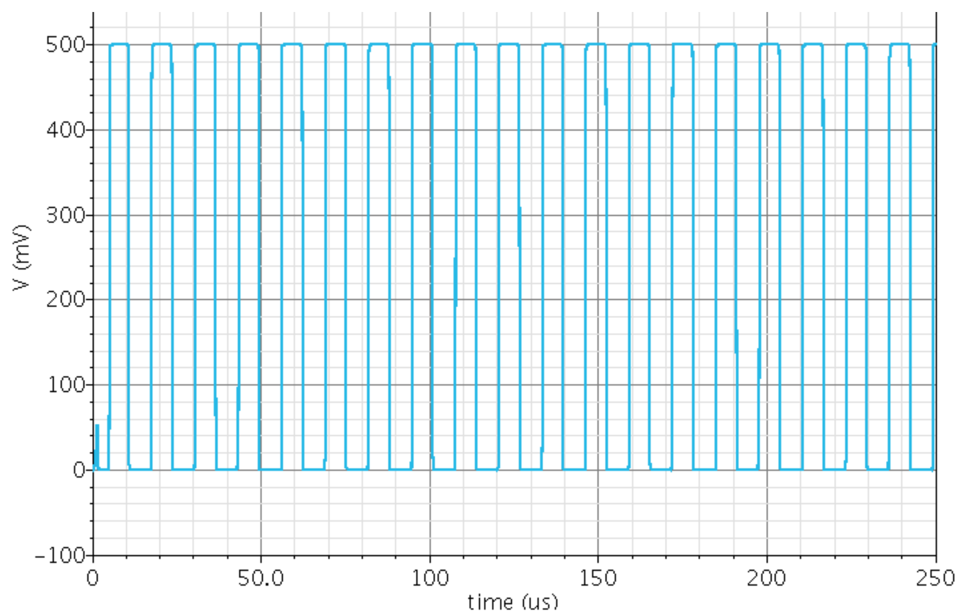

Figure 6-9: Transient response of the sensor read-out circuit with input current of 5 μA. Power supply voltage is set at 500 mV and sensor read-out circuit can work with this low supply voltage.

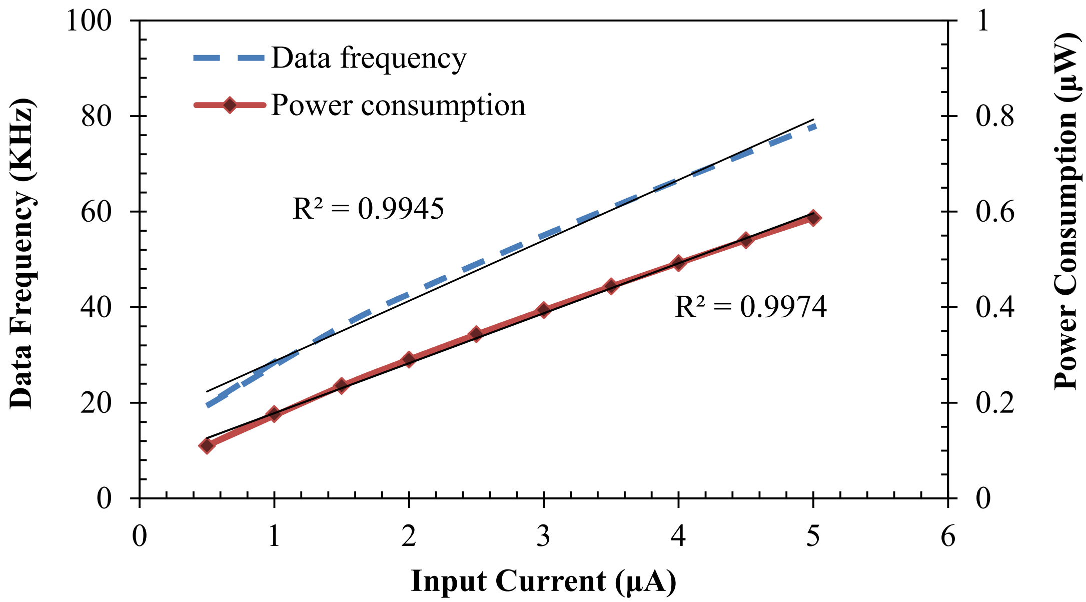

Figure 6-10: Data frequency and power consumption of the sensor signal processing unit. Both outputs show linear response with respect to input current.

From Figure 6-10 the R^2 (coefficient of determination) value for data frequency is 0.9945 which is very close to 1. It implies that when the input current is increased it increases the bias current of all five stages of the ring oscillator. As a result, average power consumption of the circuit is increased. As the input current increases linearly power consumption also increases linearly. From Figure 6-10 the R^2 (coefficient of determination) value for average power consumption is 0.9974 which is also very close to 1.

Table 6-1: Output frequency and power consumption of the data generator for the operating range of input current.

Input Current (μA)	*Data Frequency (KHz)*	*Avg. Current Consumption (μA)*	*Avg. Power Consumption (μW)*
1	28.51	0.353	0.1765
0.5	19.4	0.22	0.11
1.5	36.007	0.471	0.2355
2	42.758	0.581	0.2905
2.5	49.025	0.687	0.3435
3	55.063	0.788	0.394
3.5	60.827	0.887	0.4435
4	66.6	0.984	0.492
4.5	72.175	1.08	0.54
5	77.734	1.173	0.5865

6.2 Backward Data Telemetry Unit

To back-transmit the sensor data, LSK scheme has been used in this design. The generated digital pulses from the sensor readout block are coupled to a series combination of a MOSFET and a resistor connected in between the supply and the ground line of the secondary unit. Depending upon the level of digital pulses, the LSK modulator unit draws extra current which is reflected as a load variation on the primary side of the power link system. As a result the envelope of the power signal is modulated at a rate proportional to the frequency of the digital pulses.

6.2.1 Data Recovery Unit

The bottom tank of the differential POSC as shown in Figure 6-2 also helps extracting the data signal. The complete circuit schematic of the data recovery unit is shown in Figure 6-11. The LSK modulated envelop of the power signal appears at the bottom tank where the carrier frequency is twice the fundamental frequency of oscillation. The envelope signal is first passed through a non-inverting low-gain amplifier. An operational transconductance amplifier (OTA) is used for this purpose. Due to the low frequency response of OTA the high frequency components of the LSK signal are filtered out leaving behind only the envelope signal. The recovered signal can be further amplified and used for digital processing.

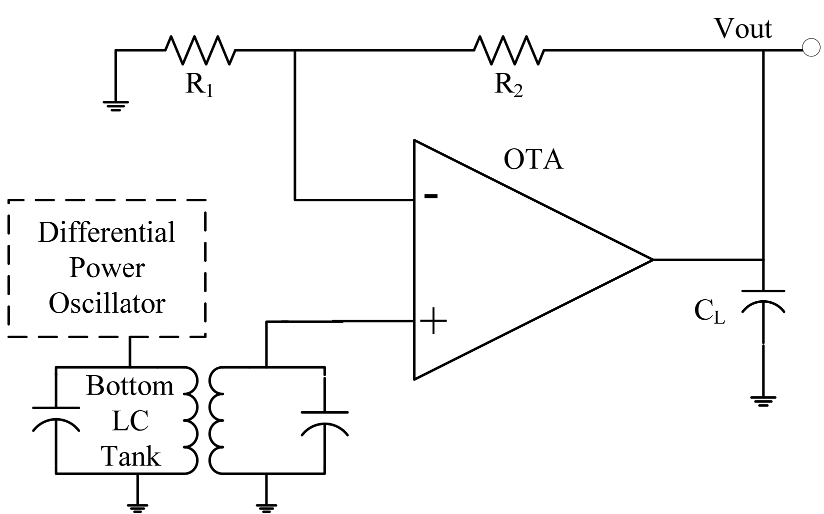

Figure 6-11: Circuit schematic of the data recovery unit.

6.3 Conclusion

In this chapter, design of power oscillator based inductive power transfer and data telemetry system have been presented. The power receiver unit has been implemented in a commercial 90 nm RF CMOS process. All the design blocks of the power receiver unit and the power oscillator block have been discussed in detail in this chapter. The current read out circuit shows a low-power implementation of current-to-data converter which would reduce the total power budget of the designed system. The charge pump based rectifier scheme can be successfully implemented to compensate the low peak to peak voltage caused by coil misalignments and lower coupling in a real system.

Chapter 7

RECOMMENDATIONS AND CONCLUSION

7.1 Original Contribution

The original contributions of this research work are summarized as follows.

-Design of a multi-spiral solenoidal inductor for biomedical applications has been proposed. By using additive mutual coupling, multi-spiral metal layers and larger number of turns the net value of inductance can be effectively increased by using the proposed scheme. The net result is the increase of inductance per unit area compared to published works in literature.

-The proposed multi-spiral solenoidal inductor scheme has been implemented on printed circuit board (PCB). This scheme contributes to higher inductance in smaller cross section area of the PCB which is desirable for implantable biomedical sensor electronics.

-The proposed multi-spiral solenoidal inductor scheme has been implemented on-chip in a 90 nm commercial RF CMOS process. This scheme leads to higher on-chip inductances in a standard CMOS process without the use of any expensive process dependent improvement schemes.

7.2 Recommendations for Future Works

The proposed work shows promising performance in enhancing the inductance density of printed circuit board and on-chip inductors. However, there are areas where further investigation will be required to increase the overall performance of the inductor with respect to inductive link based wireless power transfer system. The following works are recommended for future improvements.

-A combined realization of wireless power transfer system with PCB inductor and on-chip electronics can be performed to implement the proof of concept of WPT in biomedical applications. The inductance value of a PCB inductor can be increased by inserting ferrite core inside the PCB coil. Proposed multi-spiral solenoidal inductor can be combined with ferrite core to increase the inductance density and to decrease the overall size of the PCB system.

-Realization of the wireless power transfer system with on-chip inductors and associated electronics. This can be used to miniaturize the wireless power transfer system which could be a good step towards implementation of complete on-chip WPT system. This will open up new possibilities for various types of implantable sensors which are yet to be placed inside human body. Proposed multi-spiral solenoid structure can be combined with post-fabrication techniques to increase the quality factor of the on-chip inductors. This will lead to high inductance, high quality factor inductors which could be used to develop WPT system for biomedical applications.

7.3 Conclusion

With the recent technological improvements sensor based remote healthcare monitoring system is gaining more attraction day by day. Now-a-days much emphasis is placed on taking pro-active measures by health care professionals before the condition of the patient becomes acute. It is only possible if patients are equipped with wearable sensors. Certain sensors are placed inside the human body to obtain the information on vital physiological phenomena such as glucose, lactate, pH, oxygen, etc. These implantable sensors have associated circuits for signal processing and data transmission. Powering the circuit is always a crucial design factor. Battery cannot be placed inside the human body due to serious health risks such as poisoning and chemical burn. An alternate approach is to supply power using inductive link where power is transferred via two loosely coupled inductors.

For good inductive coupling, the inductors should have high inductance and high quality factor. But the physical dimension of the implanted inductor cannot be large due to biomedical constraints. In addition, the frequency cannot be increased due to FCC regulations. Therefore, there is a need for small sized and high inductance, high quality factor inductors for implantable sensor applications. In this work, design of a multi-spiral solenoidal printed circuit inductor for biomedical application is presented. The inductors are simulated and optimized for targeted application using Sonnet software, a commercial electromagnetic simulation tool. The targeted frequency for power transfer is 13.56 MHz which is within the license-free industrial, scientific and medical (ISM) band. Parametric study of the multi-spiral inductor is investigated in terms of number of layers, metal spacing, and metal width. Finally, it is demonstrated that the proposed multi-spiral solenoidal inductor exhibits a better overall performance in comparison with the conventional spiral inductors for biomedical applications.

Litz wire based inductors have been proposed in literature for biomedical sensor applications. But these inductors are typically large in size and are thus unsuitable for implantable sensors. In addition, reducing the size of the inductor is always a big challenge. On-chip inductor is a potential solution to this problem. However, the implementation of the integrated inductors has been a great challenge due to parasitic effects, low inductance, and low quality factor. Due to very small physical dimensions on-chip inductors exhibit inductances in the nano Henry region. To accommodate this phenomenon frequency of operation of inductive links needs to be increased to GHz region. For human tissue and small coil size the optimum frequency of operation of inductive link is 1GHz. Therefore, design and optimization of multi-spiral solenoidal integrated inductors for biotelemetry applications in 1 GHz frequency has been proposed in this work. The inductors are simulated and optimized for targeted application using Sonnet software. By using additive mutual coupling, multi-spiral metal layers and larger number of turns the net value of inductance can be effectively increased. This results in higher inductance density of on-chip inductors.

LIST OF REFERENCES

[1] G. Reach and G. S. Wilson, "Can continuous glucose monitoring be used for the treatment of diabetes?," *Analytical Chemistry,* vol. 64, pp. 381A-386A, 1992.
[2] J. Wang, "Glucose Biosensors: 40 Years of Advances and Challenges," *Electroanalysis,* vol. 13, pp. 983-988, 2001.
[3] J. Wang, "Electrochemical Glucose Biosensors," *Chemical Reviews,* vol. 108, pp. 814-825, 2007.
[4] Y. Hu and G. S. Wilson, "Rapid changes in local extracellular rat brain glucose observed with an in vivo glucose sensor," *Journal of Neurochemistry* vol. 68, pp. 1745-1752 1997.
[5] A. Schneider and T. Stieglitz, "Implantable flexible electrodes for functional electrical stimulation," *Medical device technology* vol. 15, pp. 16-18, 2004.
[6] R. D. O'Neill, "Microvoltammetric techniques and sensors for monitoring neurochemical dynamics in vivo. A review," *Analyst,* vol. 119, pp. 767-779, 1994.
[7] D. V. McAllister*, et al.*, "Microfabricated microneedles for gene and drug delivery," *Annual Review of Biomedical Engineering,* vol. 2, pp. 289-313, 2000.
[8] W. Ryu*, et al.*, "Biodegradable micro-osmotic pump for long-term and controlled release of basic fibroblast growth factor," *Journal of Controlled Release,* vol. 124, pp. 98-105, 2007.
[9] F. Yildiz, "Potential Ambient Energy-Harvesting Sources and Techniques," *Journal of Technology Studies,* vol. 35, pp. 40-48, 2009.
[10] N. Tesla, " Apparatus for Transmitting Electrical Energy," U.S. Patent, 1902.
[11] G. Lazzi, "Thermal effects of bioimplants," *Engineering in Medicine and Biology Magazine, IEEE,* vol. 24, pp. 75-81, 2005.
[12] *Guidelines for evaluating the environmental effects of radio frequency radiation,* F. C. Commission, 1996.
[13] ANSI, "American National Standard Safety Levels With Respect to Human Exposure to Radio Frequency Electromagnetic Fields, 300 kHz to 100 GHz," *ANSI Std C95.1-1982,* p. 0_1, 1982.
[14] D. Sawicki, *Police Traffic SPEED RADAR Handbook*.
[15] IEEE, "IEEE Standard for Safety Levels With Respect to Human Exposure to Radio Frequency Electromagnetic Fields, 3 kHz to 300 GHz," *IEEE Std C95.1-1991,* p. 1, 1992.
[16] S. Gabriel*, et al.*, "The dielectric properties of biological tissues .2. Measurements in the frequency range 10 Hz to 20 GHz," *Physics in Medicine and Biology,* vol. 41, pp. 2251-2269, Nov 1996.
[17] Q. H. Tang*, et al.*, "Communication scheduling to minimize thermal effects of implanted biosensor networks in homogeneous tissue," *IEEE Transactions on Biomedical Engineering,* vol. 52, pp. 1285-1294, Jul 2005.
[18] I. C. o. N.-I. R. P.-. ICNIRP, "Guidelines for limiting exposure to time-varying electric, magnetic and electromagetic fields (up to 300 GHz)," ed, 2009.
[19] FCC, "Available online: http://www.fcc.gov/cgb/sar/."

[20] A. Milenkovic*, et al.*, "Wireless sensor networks for personal health monitoring: Issues and an implementation," *Computer Communications,* vol. 29, pp. 2521-2533, 2006.
[21] S. A. Jaffari and A. P. F. Turner, "Recent advances in amperometric glucose biosensors for in vivo monitoring," *Physiological Measurement,* vol. 16, pp. 1-15, Feb 1995.
[22] E. Renard, "Implantable glucose sensors for diabetes monitoring," *Minimally Invasive Therapy & Allied Technologies,* vol. 13, pp. 78-86, Apr 2004.
[23] M. Zhang*, et al.*, "A low power sensor signal processing circuit for implantable biosensor applications," *Smart Materials & Structures,* vol. 16, pp. 525-530, Apr 2007.
[24] D. A. Baker and D. A. Gough, "A Continuous, Implantable Lactate Sensor," *Analytical Chemistry,* vol. 67, pp. 1536-1540, May 1995.
[25] C. Hierold*, et al.*, "Low power integrated pressure sensor system for medical applications," *Sensors and Actuators A-Physical,* vol. 73, pp. 58-67, Mar 1999.
[26] G. L. Cote*, et al.*, "Emerging biomedical sensing technologies and their applications," *IEEE Sensors Journal,* vol. 3, pp. 251-266, Jun 2003.
[27] M. Soma*, et al.*, "Radio-Frequency Coils in Implantable Devices: Misalignment Analysis and Design Procedure," *Biomedical Engineering, IEEE Transactions on,* vol. BME-34, pp. 276-282, 1987.
[28] W. H. Ko*, et al.*, "Design of radio-frequency powered coils for implant instruments," *Medical & Biological Engineering & Computing,* vol. 15, pp. 634-640, 1977.
[29] W. J. Heetderks, "RF powering of millimeter- and submillimeter-sized neural prosthetic implants," *IEEE Transactions on Biomedical Engineering,* vol. 35, pp. 323-327, May 1988.
[30] C. M. Zierhofer*, et al.*, "Electronic design of a cochlear implant for multichannel high-rate pulsatile stimulation strategies," *Rehabilitation Engineering, IEEE Transactions on,* vol. 3, pp. 112-116, 1995.
[31] J. H. Schulman, "The feasible FES system: Battery powered BION stimulator," *Proceedings of the IEEE,* vol. 96, pp. 1226-1239, Jul 2008.
[32] W. T. Liu*, et al.*, "A neuro-stimulus chip with telemetry unit for retinal prosthetic device," *IEEE Journal of Solid-State Circuits,* vol. 35, pp. 1487-1497, Oct 2000.
[33] B. Lenaerts and R. Puers, "An inductive power link for a wireless endoscope," *Biosensors & Bioelectronics,* vol. 22, pp. 1390-1395, Feb 2007.
[34] G. Y. Ma*, et al.*, "Power transmission for gastrointestinal microsystems using inductive coupling," *Physiological Measurement,* vol. 28, pp. N9-N18, Mar 2007.
[35] S. Mandal*, et al.*, "Circuits for an RF cochlea," in *Circuits and Systems, 2006. ISCAS 2006. Proceedings. 2006 IEEE International Symposium on*, 2006, p. 4 pp.
[36] C. Sauer*, et al.*, "Power harvesting and telemetry in CMOS for implanted devices," *Circuits and Systems I: Regular Papers, IEEE Transactions on,* vol. 52, pp. 2605-2613, 2005.

[37] M. Ghovanloo and K. Najafi, "A wideband frequency-shift keying wireless link for inductively powered biomedical implants," *Circuits and Systems I: Regular Papers, IEEE Transactions on,* vol. 51, pp. 2374-2383, 2004.

[38] G. A. Kendir*, et al.*, "An optimal design methodology for inductive power link with class-E amplifier," *Circuits and Systems I: Regular Papers, IEEE Transactions on,* vol. 52, pp. 857-866, 2005.

[39] R. Bashirullah, "Wireless Implants," *IEEE Microwave Magazine,* vol. 11, pp. S14-S23, Dec 2010.

[40] J. Sacristán-Riquelme*, et al.*, "Simple and efficient inductive telemetry system with data and power transmission," *Microelectronics Journal,* vol. 39, pp. 103-111, 2008.

[41] Z. Tang*, et al.*, "Data transmission from an implantable biotelemeter by load-shift keying using circuit configuration modulator," *Biomedical Engineering, IEEE Transactions on,* vol. 42, pp. 524-528, 1995.

[42] W. Lihsien*, et al.*, "An efficient wireless power link for high voltage retinal implant," in *Biomedical Circuits and Systems Conference, 2008. BioCAS 2008. IEEE*, 2008, pp. 101-104.

[43] L. Pengfei*, et al.*, "A Wireless Power Interface for Rechargeable Battery Operated Neural Recording Implants," in *Engineering in Medicine and Biology Society, 2006. EMBS '06. 28th Annual International Conference of the IEEE*, 2006, pp. 6253-6256.

[44] M. Sawan*, et al.*, "Multicoils-based inductive links dedicated to power up implantable medical devices: modeling, design and experimental results," *Biomedical Microdevices,* vol. 11, pp. 1059-1070, Oct 2009.

[45] S. Mandal and R. Sarpeshkar, "A Bidirectional Wireless Link for Neural Prostheses that Minimizes Implanted Power Consumption," in *Biomedical Circuits and Systems Conference, 2007. BIOCAS 2007. IEEE*, 2007, pp. 45-48.

[46] S. O'Driscoll and T. H. Meng, "Adaptive signal acquisition and wireless power transfer for an implantable prosthesis processor," in *Circuits and Systems (ISCAS), Proceedings of 2010 IEEE International Symposium on*, 2010, pp. 3589-3592.

[47] U. M. Jow and M. Ghovanloo, "Optimization of Data Coils in a Multiband Wireless Link for Neuroprosthetic Implantable Devices," *Biomedical Circuits and Systems, IEEE Transactions on,* vol. 4, pp. 301-310, 2010.

[48] R. R. Harrison*, et al.*, "A low-power integrated circuit for a wireless 100-electrode neural recording system," *IEEE Journal of Solid-State Circuits,* vol. 42, pp. 123-133, Jan 2007.

[49] A. M. Sodagar*, et al.*, "A Wireless Implantable Microsystem for Multichannel Neural Recording," *Microwave Theory and Techniques, IEEE Transactions on,* vol. 57, pp. 2565-2573, 2009.

[50] D. C. Galbraith, *et al.*, "A wide-band efficient inductive transdermal power and data link with coupling insensitive gain," *IEEE Transactions on Biomedical Engineering,* vol. 34, pp. 265-275, Apr 1987.
[51] M. Piedade, *et al.*, "Visual neuroprosthesis: a non invasive system for stimulating the cortex," *Circuits and Systems I: Regular Papers, IEEE Transactions on,* vol. 52, pp. 2648-2662, 2005.
[52] M. Sawan, *et al.*, "Wireless smart implants dedicated to multichannel monitoring and microstimulation," *Circuits and Systems Magazine, IEEE,* vol. 5, pp. 21-39, 2005.
[53] G. J. Suaning and N. H. Lovell, "CMOS neurostimulation ASIC with 100 channels, scaleable output, and bidirectional radio-frequency telemetry," *Biomedical Engineering, IEEE Transactions on,* vol. 48, pp. 248-260, 2001.
[54] T. Akin, *et al.*, "A wireless implantable multichannel digital neural recording system for a micromachined sieve electrode," *Solid-State Circuits, IEEE Journal of,* vol. 33, pp. 109-118, 1998.
[55] G. Gudnason, *et al.*, "A chip for an implantable neural stimulator," *Analog Integrated Circuits and Signal Processing,* vol. 22, pp. 81-89, Jan 2000.
[56] B. Smith, *et al.*, "An externally powered, multichannel, implantable stimulator-telemeter for control of paralyzed muscle," *IEEE Transactions on Biomedical Engineering,* vol. 45, pp. 463-475, Apr 1998.
[57] W. Guoxing, *et al.*, "Design and analysis of an adaptive transcutaneous power telemetry for biomedical implants," *Circuits and Systems I: Regular Papers, IEEE Transactions on,* vol. 52, pp. 2109-2117, 2005.
[58] L. S. Y. Wong, *et al.*, "A very low power CMOS mixed-signal IC for implantable pacemaker applications," in *Solid-State Circuits Conference, 2004. Digest of Technical Papers. ISSCC. 2004 IEEE International*, 2004, pp. 318-530 Vol.1.
[59] R. Sarpeshkar, *et al.*, "An ultra-low-power programmable analog bionic ear processor," *Biomedical Engineering, IEEE Transactions on,* vol. 52, pp. 711-727, 2005.
[60] K. D. Wise, *et al.*, "Wireless implantable microsystems: high-density electronic interfaces to the nervous system," *Proceedings of the IEEE,* vol. 92, pp. 76-97, 2004.
[61] J. D. Weiland, *et al.*, "Retinal prosthesis," *Annual Review of Biomedical Engineering,* vol. 7, pp. 361-401, 2005.
[62] K. V. Schuylenbergh, "Optimisation of inductive powering of small biotelemetry implants," PhD, K.U. Leuven ESAT-MICAS, Belgium, 1998.
[63] G. Vandevoorde and R. Puers, "Wireless energy transfer for stand-alone systems: a comparison between low and high power applicability," *Sensors and Actuators A-Physical,* vol. 92, pp. 305-311, Aug 2001.
[64] K. VanSchuylenbergh and R. Puers, "Self-tuning inductive powering for implantable telemetric monitoring systems," *Sensors and Actuators A-Physical,* vol. 52, pp. 1-7, Mar-Apr 1996.

[65] R. Puers, *et al.*, "A telemetry system for the detection of hip prosthesis loosening by vibration analysis," *Sensors and Actuators A-Physical,* vol. 85, pp. 42-47, Aug 2000.
[66] B. Ziaie, *et al.*, "A self-oscillating detuning-insensitive class-E transmitter for implantable microsystems," *Biomedical Engineering, IEEE Transactions on,* vol. 48, pp. 397-400, 2001.
[67] N. Donaldson and T. Perkins, "Analysis of resonant coupled coils in the design of radio frequency transcutaneous links," *Medical and Biological Engineering and Computing,* vol. 21, pp. 612-627, 1983.
[68] N. O. Sokal and A. D. Sokal, "Class E-A new class of high-efficiency tuned single-ended switching power amplifiers," *IEEE Journal of Solid-State Circuits,* vol. SC10, pp. 168-176, 1975.
[69] J. Uei-Ming and M. Ghovanloo, "Design and Optimization of Printed Spiral Coils for Efficient Inductive Power Transmission," in *Electronics, Circuits and Systems, 2007. ICECS 2007. 14th IEEE International Conference on*, 2007, pp. 70-73.
[70] M. R. Shah, *et al.*, "A study of printed spiral coils for neuroprosthetic transcranial telemetry applications," *Biomedical Engineering, IEEE Transactions on,* vol. 45, pp. 867-876, 1998.
[71] J. A. Von Arx and K. Najafi, "A wireless single-chip telemetry-powered neural stimulation system," in *Solid-State Circuits Conference, 1999. Digest of Technical Papers. ISSCC. 1999 IEEE International*, 1999, pp. 214-215.
[72] K. Sohee, *et al.*, "Electromagnetic compatibility of two novel packaging concepts of an inductively powered neural interface," in *Neural Engineering, 2007. CNE '07. 3rd International IEEE/EMBS Conference on*, 2007, pp. 434-437.
[73] F. W. Grover, *Inductance Calculations*. Princeton, New Jersey: Van Nostrand, 1946.
[74] E. B. Rosa, "The Self and Mutual Inductances of Linear Conductors," *Bulletin of the Bureau of Standards,* vol. 4, pp. 301-344, 1908.
[75] H. Greenhouse, "Design of Planar Rectangular Microelectronic Inductors," *Parts, Hybrids, and Packaging, IEEE Transactions on,* vol. 10, pp. 101-109, 1974.
[76] Sonnet, "Sonnet Software," 12.56 ed, 2010.
[77] S. S. Mohan, *et al.*, "Simple accurate expressions for planar spiral inductances," *IEEE Journal of Solid-State Circuits,* vol. 34, pp. 1419-1424, Oct 1999.
[78] T. Chih-Ming and L. Chien-Neng, "Multilevel Suspended Thin-Film Inductors on Silicon Wafers," *Electron Devices, IEEE Transactions on,* vol. 54, pp. 1510-1514, 2007.
[79] J. Uei-Ming and M. Ghovanloo, "Modeling and optimization of printed spiral coils in air and muscle tissue environments," in *Engineering in Medicine and Biology Society, 2009. EMBC 2009. Annual International Conference of the IEEE*, 2009, pp. 6387-6390.

[80] J. Uei-Ming and M. Ghovanloo, "Optimization of a multiband wireless link for neuroprosthetic implantable devices," in *Biomedical Circuits and Systems Conference, 2008. BioCAS 2008. IEEE*, 2008, pp. 97-100.

[81] J. Masuch and M. Delgado-Restituto, "Design constraints for the inductive power and data link of an implanted body sensor," in *Circuit Theory and Design, 2009. ECCTD 2009. European Conference on*, 2009, pp. 425-428.

[82] C. Peters and Y. Manoli, "Inductance calculation of planar multi-layer and multi-wire coils: An analytical approach," *Sensors and Actuators a-Physical,* vol. 145, pp. 394-404, Jul-Aug 2008.

[83] A. M. Niknejad, "Analysis, Simulation, and Applications of Passive Devices on Conductive Substrates," Ph. D., U. C. Berkeley, 2000.

[84] R. B. Jaime Aguilera, *Design and Test of Integrated Inductors for RF Applications*. Boston: Kluwer Academic Publishers, 2004.

[85] T. H. Lee, *The Design of CMOS Radio-Frequency Integrated Circuits*, 2nd ed.: Cambridge University Press 2003.

[86] N. M. Nguyen and R. G. Meyer, "A 1.8 GHz monolithic LC voltage-controlled oscillator," in *Solid-State Circuits Conference, 1992. Digest of Technical Papers. 39th ISSCC, 1992 IEEE International*, 1992, pp. 158-159, 272.

[87] C. P. Yue and S. S. Wong, "Physical modeling of spiral inductors on silicon," *Electron Devices, IEEE Transactions on,* vol. 47, pp. 560-568, 2000.

[88] A. Scuderi*, et al.*, "A lumped scalable model for silicon integrated spiral inductors," *Circuits and Systems I: Regular Papers, IEEE Transactions on,* vol. 51, pp. 1203-1209, 2004.

[89] M. Peter*, et al.*, "Scalable Inductor Model on Lossy Substrates with Accurate Eddy Current Simulation," in *Solid-State Device Research Conference, 2000. Proceeding of the 30th European*, 2000, pp. 160-163.

[90] J. del Pino*, et al.*, "Models and Tools for CMOS Integrated Inductors," *Analog Integrated Circuits and Signal Processing,* vol. 33, pp. 171-178, 2002.

[91] C. P. Yue*, et al.*, "A physical model for planar spiral inductors on silicon," in *Electron Devices Meeting, 1996. IEDM '96., International*, 1996, pp. 155-158.

[92] C. P. Yue and S. S. Wong, "On-chip spiral inductors with patterned ground shields for Si-based," *Solid-State Circuits, IEEE Journal of,* vol. 33, pp. 743-752, 1998.

[93] K. B. Ashby*, et al.*, "High Q inductors for wireless applications in a complementary silicon bipolar process," *Ieee Journal of Solid-State Circuits,* vol. 31, pp. 4-9, Jan 1996.

[94] J. Y. C. Chang*, et al.*, "Large suspended inductors on silicon and their use in a 2-μm CMOS RF amplifier," *IEEE Electron Device Letters,* vol. 14, pp. 246-248, May 1993.

[95] C. Chen-Yu and G. M. Rebiez, "Planar microwave and millimeter-wave lumped elements and coupled-line filters using micro-machining techniques," *Microwave Theory and Techniques, IEEE Transactions on,* vol. 43, pp. 730-738, 1995.

[96] Y. Sun, *et al.*, "Suspended membrane inductors and capacitors for application in silicon MMIC's," in *Microwave and Millimeter-Wave Monolithic Circuits Symposium, 1996. Digest of Papers., IEEE 1996*, 1996, pp. 99-102.

[97] B. Piernas, *et al.*, "High-Q factor three-dimensional inductors," *Microwave Theory and Techniques, IEEE Transactions on,* vol. 50, pp. 1942-1949, 2002.

[98] I. J. Bahl, "High-performance inductors," *Microwave Theory and Techniques, IEEE Transactions on,* vol. 49, pp. 654-664, 2001.

[99] N. Choong-Mo and K. Young-Se, "High-performance planar inductor on thick oxidized porous silicon (OPS) substrate," *Microwave and Guided Wave Letters, IEEE,* vol. 7, pp. 236-238, 1997.

[100] K. Bon-Kee, *et al.*, "Monolithic planar RF inductor and waveguide structures on silicon with performance comparable to those in GaAs MMIC," in *Electron Devices Meeting, 1995., International*, 1995, pp. 717-720.

[101] J. R. Long and M. A. Copeland, "Modeling, characterization and design of monolithic inductors for silicon RFICs," in *Custom Integrated Circuits Conference, 1996., Proceedings of the IEEE 1996*, 1996, pp. 185-188.

[102] M. Danesh and J. R. Long, "Differentially driven symmetric microstrip inductors," *Microwave Theory and Techniques, IEEE Transactions on,* vol. 50, pp. 332-341, 2002.

[103] J. N. Burghartz, *et al.*, "Multilevel-spiral inductors using VLSI interconnect technology," *IEEE Electron Device Letters,* vol. 17, pp. 428-430, Sep 1996.

[104] L. Sang-Gug, *et al.*, "Design and analysis of symmetric dual-layer spiral inductors for RF integrated circuits," in *ASICs, 1999. AP-ASIC '99. The First IEEE Asia Pacific Conference on*, 1999, pp. 5-8.

[105] L. Liang-Hung, *et al.*, "High-Q X-band and K-band micromachined spiral inductors for use in Si-based integrated circuits," in *Silicon Monolithic Integrated Circuits in RF Systems, 2000. Digest of Papers. 2000 Topical Meeting on*, 2000, pp. 108-112.

[106] J. M. Lopez-Villegas, *et al.*, "Improvement of the quality factor of RF integrated inductors by layout optimization," in *Radio Frequency Integrated Circuits (RFIC) Symposium, 1998 IEEE*, 1998, pp. 169-172.

[107] S. O'Driscoll, "A mm-Sized Implantable Power Receiver with Adaptive Matching," presented at the 9th Annual IEEE Conference on Sensors, Waikoloa, Big Island, Hawaii, USA, 2010.

[108] S. Gabriel, *et al.*, "The dielectric properties of biological tissues .3. Parametric models for the dielectric spectrum of tissues," *Physics in Medicine and Biology,* vol. 41, pp. 2271-2293, Nov 1996.

[109] S. O'Driscoll, "Adaptive signal acquisition and power delivery for implanted medical devices," Ph. D. Dissertation, Stanford University, 2009.

[110] T. E. Kolding, "On-wafer calibration techniques for giga-hertz CMOS measurements," in *Microelectronic Test Structures, 1999. ICMTS 1999. Proceedings of the 1999 International Conference on*, 1999, pp. 105-110.

[111] T. E. Kolding, "A four-step method for de-embedding gigahertz on-wafer CMOS measurements," *Electron Devices, IEEE Transactions on,* vol. 47, pp. 734-740, 2000.
[112] A. Golmakani*, et al.*, "Modeling and optimization of a solenoidal integrated inductor for RF ICs," *International Journal of Rf and Microwave Computer-Aided Engineering,* vol. 20, pp. 182-189, 2010.
[113] G. Haobijam and R. Paily, "Design of multilevel pyramidically wound symmetric inductor for CMOS RFIC's," *Analog Integrated Circuits and Signal Processing,* vol. 63, pp. 9-21, Apr 2010.
[114] W.-Y. Yin*, et al.*, "Vertical Topologies of Miniature Multispiral Stacked Inductors," *Microwave Theory and Techniques, IEEE Transactions on,* vol. 56, pp. 475-486, 2008.
[115] M. A. Adeeb, "A class-E inductive powering link with backward data communications for implantable sensor systems," M. Sc., Department of Electrical Engineering and Computer Science, The University of Tenessee, Knoxville,, 2006.
[116] M. T. Zhang and F. C. Lee, "Commutation analysis of self-driven synchronous rectifiers in an active-clamp forward converter," in *Power Electronics Specialists Conference, 1996. PESC '96 Record., 27th Annual IEEE*, 1996, pp. 868-873 vol.1.
[117] S. Mandal and R. Sarpeshkar, "Low-Power CMOS Rectifier Design for RFID Applications," *Circuits and Systems I: Regular Papers, IEEE Transactions on,* vol. 54, pp. 1177-1188, 2007.
[118] M. Ghovanloo and K. Najafi, "Fully integrated wideband high-current rectifiers for inductively powered devices," *Solid-State Circuits, IEEE Journal of,* vol. 39, pp. 1976-1984, 2004.
[119] M. R. Haider*, et al.*, "Low-Power Low-Voltage Current Readout Circuit for Inductively Powered Implant System," *IEEE Transactions on Biomedical Circuits and Systems,* vol. 4, pp. 205-213, Aug 2010.
[120] A. B. Islam*, et al.*, "A digitally controllable current readout circuit and modulator unit for remote monitoring and biotelemetry applications," in *Electrical and Computer Engineering (ICECE), 2010 International Conference on*, 2010, pp. 462-465.
[121] J. C. Rautio and R. F. Harrington, "An Electromagnetic Time-Harmonic Analysis of Shielded Microstrip Circuits," *IEEE Transactions on Microwave Theory and Techniques,* vol. 35, pp. 726-730, Aug 1987.
[122] J. C. Rautio and R. F. Harrington, "An Efficient Electromagnetic Analysis of Arbitrary Microstrip Circuits," in *Microwave Symposium Digest, 1987 IEEE MTT-S International*, 1987, pp. 295-298.

APPENDIX

A1. Sonnet Software

All the electromagnetic simulations performed in this work are done using commercial high frequency electromagnetic simulator named Sonnet. The core theory behind Sonnet was developed in 1986 by Rautio and Harrington [121, 122]. The theory expresses the fields inside the box as a sum of waveguide modes and is thus closely related to the spectral domain approach. Sonnet's electromagnetic analysis engine is known as 'Em'. It uses a modified method of moments analysis based on Maxwell's equations to perform a three dimensional current analysis of predominantly planar structures. Em computes S, Y, or Z-parameters, transmission line parameters (Z_0, E_{eff}, VSWR, G_{Max}, Z_{in}, and the loss factor), and SPICE equivalent lumped element networks. Em's circuit netlist capability cascades the results of electromagnetic analyses with lumped elements, ideal transmission line elements and external S-parameter data. Em performs electromagnetic analysis for arbitrary 3-D planar (e.g., microstrip, coplanar, stripline, etc.) geometries, maintaining full accuracy at all frequencies. Em is a "full-wave" analysis in that it takes into account all possible coupling mechanisms. The analysis inherently includes dispersion, stray coupling, discontinuities, surface waves, moding, metallization loss, dielectric loss and radiation loss. Since Em uses a surface meshing technique, i.e. it meshes only the surface of the circuit metallization; Em can analyze predominately planar circuits much faster than volume meshing techniques.

Em analyzes 3-D structures embedded in planar multilayered dielectric on an underlying fixed grid. For this class of circuits, em can use the FFT (Fast Fourier Transform) analysis technique to efficiently calculate the electromagnetic coupling on and between each dielectric surface. This provides em with its several orders of magnitude of speed increase over volume meshing and other non-FFT based surface meshing techniques. Em is a complete electromagnetic analysis; all electromagnetic effects, such as dispersion, loss, stray coupling, etc., are included. There are only two approximations used by em. First, the finite numerical precision inherent in digital computers. Second, em subdivides the metalization into small subsections made up of cells. Em evaluates the electric field everywhere due to the current in a single subsection. Em then repeats the calculation for every subsection in the circuit, one at a time. In so doing, em effectively calculates the "coupling" between each possible pair of subsections in the circuit. Each subsection generates an electric field everywhere on the surface of the substrate, but we know that the total tangential electric field must be zero on the surface of any lossless conductor. This is the boundary condition: no voltage is allowed across a perfect conductor. The problem is solved by assuming current on all subsections simultaneously. Em adjusts these currents so that the total tangential electric field, which is the sum of all the individual electric fields just calculated, goes to zero everywhere that there is a conductor. The currents that do this form the current distribution on the metalization. Once we have the currents, the S-parameters (or Y- or Z-) follow immediately. If there is metalization loss, we modify the boundary condition. Rather than zero tangential electric field (zero voltage), we make the tangential electric field (the voltage on each subsection) proportional to the current in the subsection. Following Ohm's Law, the constant of proportionality is the metalization surface resistivity (in Ohms/square).

A 2. Matlab Code

Calculation of PCB inductance

```
% Calculation of inductance
%% Basic parameters
do=9.5e-3; %do=outer diameter of the inductor
di=5.5e-3; %di=inner diameter of the inductor
n=4; %number of spiral
w=0.25e-3; %width of the spiral
tc=35.56e-6; %thickness of the spiral
s=0.25e-3; %spacing of the spiral
sigma_c=5.8e7; %conductivity of the copper
mu=pi*4e-7; %permeability
f=10e6; %frequency

%% Single layer

delta=sqrt(1/(pi*mu*f*sigma_c)); %delta=skin depth, for copper mu_r =1,
mu_copper=mu_0=mu

lc=4*n*do-4*n*w-((2*n+1)^2)*(s+w); %length of the spiral
Rdc=lc/(sigma_c*w*tc); %Rdc=DC resistance
Rs=(Rdc*tc)/(delta*(1-exp(-tc/delta)));  %Rs=AC resistance considering
skin effect

lg=4*(do-w*n)*(n-1)-4*s*n*(n+1); % length of the gap

phi=(do-di)/(do+di); % Fill factor
davg=(do+di)/2; %average of diameters

L=0.74*(1.27*mu*(n^2)*davg*(log(2.07/phi)+(0.18*phi)+(0.13*phi*phi)))/2
; %L=self-inductance for one layer
```

```
Q=(2*pi*f)*L/Rs; % quality factor of the inductor

Erc=1; %Erc=relative dielectric constant of Air
Ers=4.4; %Ers=relative dielectric constant of FR4 material
a=0.9;
b=0.1;
eps=8.854e-12; %permittivity of free space

Cp1=(a*Erc+b*Ers)*eps*tc*lg/s;  %capacitance between trace lines
Cp2=(b*Ers*eps*tc*lc)/s;  %capacitance between stacked traces
Ctrace=(4.4*eps*lc)/(2*tc);

%% double layer

k_1=0.475; %coupling coefficient between two layers, from sonnet
simulation
L_2layer=2*L+2*k_1*L;

k_2=0.463;
L_3layer=3*L+4*k_1*L+2*k_2*L;

k_3=0.1;
L_4layer=4*L+6*k_1*L+4*k_2*L+2*k_3*L;
```

Conversion of S parameter to Y parameter and calculation of inductance and quality factor

```
%% S to Y conversion
%% values of s11, s22, s21, s22 and Frequency are measured and not
given here

max=length(s11mag);
s11=zeros(max:1);
s_params=zeros(2,2,max);

for j=1:max
    s11(j)=s11mag(j).*exp((s11angle(j)*pi/180)*1i);
    s12(j)=s12mag(j).*exp((s12angle(j)*pi/180)*1i);
    s21(j)=s21mag(j).*exp((s21angle(j)*pi/180)*1i);
    s22(j)=s22mag(j).*exp((s22angle(j)*pi/180)*1i);
```

```
    s_params(:,:,j)=[s11(j) s12(j); s21(j) s22(j)];
end

y_params = s2y(s_params, 50);
for j=1:max
    L(j)=imag(1/y_params(1,1,j))/(2*pi*Frequency(j));
    Q(j)=imag(1/y_params(1,1,j))/real(1/y_params(1,1,j));
end

plotyy(Frequency,L,Frequency,Q);
figure;
[lineseries,hsm] = smithchart(s11);
```

Vita

Ashraf B. Islam received his B. Sc. degree from Bangladesh University of Engineering and Technology (BUET), Bangladesh, in 2007. From January 2008 he is pursuing his Ph. D. studies in the University of Tennessee, Knoxville, USA. His doctoral research is focused on the development of wireless power transfer and data telemetry system for biomedical applications. He has several publications in different journals and conference proceedings. He has received best oral paper award in the 19^{th} Connecticut Microelectronics and Optoelectronics Consortium in 2010. He has also received University of Tennessee Citation Award for extra ordinary professional promise in 2011. His fields of interests are design of on-chip and PCB inductors, low-power analog and RF circuit design, low-power circuit design for sensor instrumentations, etc.